

High-latitude sedimentation in response to climate variability during the Cenozoic

Natalia Varela

Dissertation submitted to the faculty of the Virginia Polytechnic Institute and State University in partial fulfillment of the requirements for the degree of

Doctor of Philosophy  
In  
Geosciences

Brian W. Romans, Chair  
Tina Dura  
Kenneth A. Eriksson  
Benjamin C. Gill

December 5, 2023  
Blacksburg, VA

Keywords: sedimentology, high-latitude sedimentation, Antarctic Bottom Water, submarine canyon deposition, hydrothermal vent, Pliocene, Pleistocene, Paleocene-Eocene, climate change

Copyright © Natalia Varela 2023

# High-latitude sedimentation in response to climate variability during the Cenozoic

Natalia Varela

## **ABSTRACT**

Here we investigate sedimentological responses to past climate change in shallow to deep marine depositional environments. Our primary study spans from the Late Pliocene to the Pleistocene (3.3 to 0.7 Ma), and features results from two International Ocean Discovery Program (IODP) Sites U1525 and U1524. Each of these sites is discussed in separate chapters here (Chapters 1 and 2). This interval experienced the change from the warming of the Late Pliocene, known as the Mid-Piacenzian Warming Period, to the Pleistocene cooling. This shift significantly impacted the expansion of the West Antarctic Ice Sheet, sea ice/polynya formation, and, notably, the genesis of Antarctic Bottom Water (AABW), a crucial component of the global thermohaline circulation. In Chapter 1, we propose that turbidite currents, arising from the formation of dense shelf water (DSW) in the Ross Sea (a precursor to AABW), leave a distinct record in the levees of Hillary Canyon. This canyon acts as a conduit, channeling DSW into the deep ocean and contributing to AABW production. By analyzing turbidite beds based on their frequency, thickness, and grain size, we gain insights into the historical occurrence and magnitude of these currents. Furthermore, we explore the influence of factors such as shelf availability and sea ice/polynya formation within the broader climate context of AABW formation. Chapter 2 shifts its focus to the sedimentological variability from shelf-to-slope along Hillary Canyon. This chapter examines the turbidite record associated with AABW formation within the shared timeframe (2.1 to 0.7 million years ago) between IODP Sites U1524 and U1525, and the impact of along slope currents and other processes in the sedimentary deposition and transport.

The second study interval (Chapter 3), focuses on the regional sedimentological response proximal to a hydrothermal vent complex associated with the Paleocene-Eocene Thermal Maximum (PETM; ca. 56 Ma), a global warming event during which thousands of Gt C was released into the ocean-atmosphere on Kyr timescales. IODP Site U1568, strategically

located near the hydrothermal vent complex and part of a broader drilling transect in the Modgunn Arch, North Atlantic, is the main study subject. This site's proximity to the vent complex offers a distinctive environment for refining our understanding of stratigraphy and sedimentology within the PETM. We achieve this through a comprehensive analysis of grain size and composition, coupled with a comparison to XRF data. Our findings show that the timing between the onset of the PETM and the response of the sedimentary system to the warming, reflected on the grain size coarsening after the start of the PETM, is not synchronous. Notably, the transition from a marine to a more terrestrial composition predates this shift in grain size, aligning with the PETM onset instead.

# High-latitude sedimentation in response to climate variability during the Cenozoic

Natalia Varela

## **GENERAL AUDIENCE ABSTRACT**

Deep-marine core records are invaluable sources of sedimentological information that provide insights into the ocean's response to past climates. These cores, extracted from the deep-ocean floor, contain layers of sediment that accumulate over time because of the different processes that occur in the ocean. Analyzing these sediments, by looking at their physical characteristics like how frequently are they deposited, the thickness of the layers, their grain size, and their composition helps to reconstruct past environmental conditions and understand how the oceans have responded to climatic changes.

This dissertation focuses on studying the record of two main processes. The first one is the sedimentary record left behind by the formation of Antarctic Bottom Water (AABW), one of the coldest ( $-1^{\circ}\text{C}$ ), deepest ( $> 2000$  meters below sea level), and densest water masses in the ocean. AABW is a key component of the global ocean circulation system, often referred to as the "global conveyor belt" or the thermohaline circulation. This circulation pattern plays a crucial role in redistributing heat, salt, and nutrients around the world's oceans. AABW is formed near Antarctica through a process that begins with the cooling and sinking of surface waters near the continent. As these waters sink, they become denser and eventually form AABW, filling the deep ocean basins around Antarctica. The dense water flows from the surface to the bottom of the ocean forming turbidity currents. These turbidity currents, dense plumes of water and sediments, flow down submarine conduits, such as Hillary Canyon in the Ross Sea, Antarctica, leaving a sedimentary record in the levees or flanks, called turbidites. The turbidite sequences in sediment cores can reveal information about the frequency and magnitude of these currents, providing insights into the sediment transport processes in deep-marine settings, and for this work, the history of the AABW formation over the last 3.3 Ma. This study will help to understand what are the main controls for AABW formation across different climates in the past, and how we project this into the future climate scenarios.

In the second part of the study (Chapter 3), we look at the sedimentary record of a warming event that happened around 56 million years ago. This event, known as the Paleocene-Eocene Thermal

Maximum (PETM), involved a significant amount of carbon being released into the air and oceans over thousands of years (150,000 to 200,000).

Our focus is IODP Site U1568, located near a submarine hydrothermal vent, and part of a larger drilling transect in the North Atlantic's Modgunn Arch. The vent's unique location provides a crucial perspective for understanding how the system responded to the warming during the Paleocene-Eocene Thermal Maximum (PETM). This warming event was triggered by the release of carbon into the atmosphere, with the vent serving as one of the conduits for this release. To understand this, we studied the grain size and content of the sediment, and compared that with XRF data. Changes in grain size serve as indicators of shifts in the energy of the environment – coarser grains signify a more energetic system. Warmer weather, for instance, can increase precipitation, leading to more erosion and sediment influx into the basin. This influx also brings in more materials from the land, as evidenced by the presence of microfossils and plant fragments. Our discoveries indicate that the sedimentary system responded gradually to the PETM, as reflected in the coarsening of grain size after the PETM's onset. Notably, the transition from a marine to a more terrestrial composition occurred before the change in grain size, aligning more closely with the initiation of the PETM itself.

## **Dedication**

To my family, for a lifetime of unwavering support, and especially to Bruno, the little light of our lives.

## **Acknowledgments**

I would like to express my forever gratitude to my advisor, Dr. Brian Romans, for welcoming me into this project back in 2018. His support, guidance, and patience, along with the technical skills I acquired under his mentorship, were instrumental in successfully completing this part of my life as a geoscientist, and I look forward to collaborating in the future.

To my advisory committee, for the helpful insight and supportive feedback over the years: Drs. Tina Dura, Ken Eriksson, and Ben Gill.

To the department head Dr. Steve Holbrook and the Department of Geosciences, for supporting my Ph.D. and my career growth.

To all the faculty from whom I had the luck to learn, but especially, Dr. John Chermak, Drs. Maddy Schreiber, Shuhai Xiao, Ryan Pollyea, Rachel Reid, Trish Dove, and James Spotila.

To April Newcomer and Lacie Kmetz, for helping me to get to the final line, and all the other deadlines in between.

To Mary Jane Smith, for being awesome and always on our side, and to Mariah Green for the same reasons. To Sharon Collins and Bera Cuskovic, for helping me with the most random problems, at all times.

To the NSF funding support through grant # 2000992 and U.S. Science Support Program (IODP) grants for supporting my research and further training through workshops and travel support.

To the co-chiefs and science party of IODP Expeditions 374 (Ross Sea) and 396 (Mid-Norwegian margin), for the opportunity to collaborate, and for the invaluable scientific and professional experience.

To the P.E.O. IPS program that aided me financially, but more importantly, through which I met a supportive community of women, particularly the Blacksburg and Radford chapters. Special shout-out to Sandi Webster, Becky Covey, Bev Lineweaver, Annemieke Philippi, and Jennifer Kiwus.

To my buddies from the Sedimentary Systems Research lab, Drs. Seba Kaempfe and Drew Parent, and Michala Puckett.

To the Geochem ladies of Derring 1091: Yezi Yang, Tara Putri, Kayla McCabe, and Amy Hagen, for great conversations about rocks, cats, and life in general, but also a great support system through the rough seas of grad school.

To the 4<sup>th</sup> and 5<sup>th</sup> floors: the El Bronco crew (Max Garvue, Kaitlyn DeFreece, David Bruce, Elizabeth Curtiss), Lowell Moore, Faisal Adams, Jonny Prouty, Alix Ehlers.

To my Derring friends who are now pursuing their own paths of glory: Drs. Selva Marroquin, Jess DePaolis, Allie Nagurney, Amin Abassi Baghbadorani, Kannikha Kolandaivelu, Eszter Sendula, Morrison Nolan, Devin Hoffman, Khahn To, Sarah Ulrich, Aly Hoeher.

To the Chileans of Blacksburg: Valentina, Cristobal and Emma, Yuki, Alvaro, Josefa, Natalia, Pablo, Isabel, Daniel, and José. Muchas gracias.

To Lisley Gomes and Ana Paula Taroza, for that last track ran together.

To my friends from Chile, for their overseas support, especially Fa, Sole, Cif, Oleito, Paulamer, Tipps & Giapoldo, Nito M, Emilio Mena, Marko Yurac, Lauris Torres, Pililo, Rocío Gallardo, and my Sensei.

To my extended family, the Valenzuelas, for their love and encouragement, all the way from Chile and beyond.

To Francisco, Oriana, and the Vivent-Barahona family, for the many years of loving support.

To Dustin, Jody, and Dasha Harper, for welcoming me into their lives.

To Remi, Heidi, and Mushu for keeping me sane.

To my parents, Cecilia and Reinard, and my siblings, Rafa and Pablo, and their families, for their constant encouragement from all their corners of the world. To my nephew, Bruno, that gives me all the reasons to keep going.

## Introduction

The archives of shallow-to-deep marine sediments offer valuable insights into the historical responses of the ocean to climate change. Shallow marine sediments are particularly responsive to short-term environmental changes, whereas deep marine sediments provide a more stable and continuous record of long-term climate trends and global-scale processes. Integrating information from both sediment types creates a more comprehensive understanding of Earth's past environmental conditions and the sedimentary system's response. Consequently, these sediment records significantly contribute to our comprehension of past climates and aid in predicting future environmental changes. This dissertation focuses on two high-latitude records situated in opposite hemispheres. First, in the Ross Sea, Antarctica, we examine the deep-marine record of bottom water formation over the past 3.3 million years, simultaneously investigating spatial stratigraphic and sedimentological variability along a submarine canyon-channel system. The other deposit is the subject of the sedimentological analysis of a unique shallow-marine vent fill crater associated with a major warming event at 56 Ma in the North Atlantic.

Chapter one, *Antarctic Bottom Water (AABW) formation history during the Pliocene-Pleistocene from turbidites at IODP Site U1524 (Ross Sea)* investigates the Antarctic Bottom Water (AABW) formation history during the Pliocene-Pleistocene at IODP Site U1524 in the Ross Sea. Focused on Hillary Canyon, a key conduit for dense shelf water (DSW) outflow (McKay et al., 2019; Conte et al., 2021; Gales et al., 2021), the study examines oceanographic-sedimentary processes, emphasizing turbidity currents triggered by cascading DSW (Baines & Condie, 1998). We identified over 3,300 turbidites, recorded their bed thickness, and analyzed the grain size of one-hundred of them, that revealed sedimentological characteristics consistent with the same process. Utilizing a Rouse-type model (Rouse & others, 1938), the integration of the sedimentary parameters obtained here elucidates low suspended sediment concentrations and velocities for the turbidite plume, highlighting the impact of salinity and temperature changes on DSW cascading. We associate the late Pliocene turbidite frequency with climate cooling, West Antarctic Ice Sheet expansion, and increased sea ice-polynya formation (McKay et al., 2012), while early Pleistocene reduction correlates with changes in continental shelf area and decreased DSW-AABW

production, contributing valuable insights into Ross Sea dynamics and broader climate variations over geological time scales.

Chapter 2, *Proximal-distal patterns in density-flow deposits on the Ross Sea continental slope and rise: Sedimentological characterization of Pleistocene deposits from IODP Sites U1524 and U1525*, builds upon the concepts introduced in Chapter 1. In the earlier chapter, we proposed that turbidites serve as a record of Antarctic Bottom Water (AABW) formation, with this process being preserved in the levee deposits of Hillary Canyon, a crucial archive for ice sheet-ocean interactions since the Late Oligocene (De Santis et al., 1995; Conte et al., 2021). In this chapter, we augment the data from IODP Site U1524 with sedimentological analyses of the Pleistocene interval at Site U1525. The results show similarities in turbidite bed thickness and frequency until ~1 Ma, after which Site U1524 exhibits a significant decline in turbidite frequency. This decline may be associated with the strengthening of the Antarctic Slope current or the offshore displacement of DSW-AABW formation during glacial periods (Conte et al., 2021; Bollen et al., 2022). These findings highlight the intricate interplay of oceanographic processes and ice sheet dynamics in the Ross Sea, and the influence of the shelf- to -slope processes in the sedimentary record.

The final chapter moves away from the Southern Ocean towards the North Atlantic, and further into time (~56 Ma), focusing into refining the existing data by adding grain size and compositional data. Chapter 3 “*Grain size and compositional characterization of the sedimentary infill of a hydrothermal vent complex in the Vøring Basin, North Atlantic (IODP Hole U1568A): Implications for constraining sedimentary system response to the Paleocene-Eocene Thermal Maximum (PETM)*”, investigates the sedimentology of the Modgunn Hydrothermal Vent Complex (HTVC) in the mid-Norwegian margin, North Atlantic, associated with the Paleocene-Eocene Thermal Maximum (PETM), a major warming event in the Cenozoic (Kennett & Stott, 1991; Thomas & Shackleton, 1996; Zachos et al., 2001). We analyzed the grain size, sorting, and composition of 163 core samples from IODP Expedition 396's Hole U1568A, to characterize the system's response to the PETM. The study indicates a delayed sedimentary system response but a quicker biotic response, providing a valuable physical proxy for assessing system sensitivity to climate-induced changes, particularly in hydrological versus biological systems.

## References

- Baines, P. G., & Condie, S. (1998, March 18). *Observations and Modelling of Antarctic Downslope Flows: A Review*. AGU Journals; American Geophysical Union (AGU). <https://onlinelibrary.wiley.com/doi/abs/10.1029/AR075p0029>
- Bollen, M., Riesselman, C. R., Ohneiser, C., Albot, O., McKay, R., Lee, M. K., Yoo, K.-C., Kim, S., Lee, J. I., & Levy, R. (2022). Pleistocene oceanographic variability in the Ross Sea: A multiproxy approach to age model development and paleoenvironmental analyses. *Global and Planetary Change*, 216, 103901. <https://doi.org/10.1016/j.gloplacha.2022.103901>
- Conte, R., Rebesco, M., De Santis, L., Colleoni, F., Bensi, M., Bergamasco, A., Kovacevic, V., Gales, J., Zgur, F., Accettella, D., De Steur, L., Ursella, L., McKay, R., Kim, S., & Lucchi, R. G. (2021). Bottom current control on sediment deposition between the Iselin Bank and the Hillary Canyon (Antarctica) since the late Miocene: An integrated seismic-oceanographic approach. *Deep Sea Research Part I: Oceanographic Research Papers*, 176, 103606. <https://doi.org/10.1016/j.dsr.2021.103606>
- De Santis, L., Anderson, J. B., Brancolini, G., & Zayatz, I. (1995). Seismic Record of Late Oligocene Through Miocene Glaciation on the Central and Eastern Continental Shelf of the Ross Sea. In *Geology and Seismic Stratigraphy of the Antarctic Margin* (pp. 235–260). American Geophysical Union (AGU). <https://doi.org/10.1029/AR068p0235>
- Gales, J., Rebesco, M., De Santis, L., Bergamasco, A., Colleoni, F., Kim, S., Accettella, D., Kovacevic, V., Liu, Y., Olivo, E., Colizza, E., Florindo-Lopez, C., Zgur, F., & McKay, R. (2021). Role of dense shelf water in the development of Antarctic submarine canyon morphology. *Geomorphology*, 372, 107453. <https://doi.org/10.1016/j.geomorph.2020.107453>
- Kennett, J. P., & Stott, L. D. (1991). Abrupt deep-sea warming, palaeoceanographic changes and benthic extinctions at the end of the Palaeocene. *Nature*, 353(6341), Article 6341. <https://doi.org/10.1038/353225a0>
- McKay, R., De Santis, L., Kulhanek, D. K., & Expedition 374 Scientists (Eds.). (2019). *Ross Sea West Antarctic Ice Sheet History* (Vol. 374). International Ocean Discovery Program. <https://doi.org/10.14379/iodp.proc.374.2019>

- McKay, R., Naish, T., Carter, L., Riesselman, C., Dunbar, R., Sjunneskog, C., Winter, D., Sangiorgi, F., Warren, C., Pagani, M., Schouten, S., Willmott, V., Levy, R., DeConto, R., & Powell, R. D. (2012). Antarctic and Southern Ocean influences on Late Pliocene global cooling. *Proceedings of the National Academy of Sciences*, *109*(17), 6423–6428. <https://doi.org/10.1073/pnas.1112248109>
- Rouse, H. & others. (1938). *Fluid mechanics for hydraulic engineers* (Vol. 1). McGraw-Hill New York.
- Thomas, E., & Shackleton, N. J. (1996). The Paleocene-Eocene benthic foraminiferal extinction and stable isotope anomalies. *Geological Society, London, Special Publications*, *101*(1), 401–441. <https://doi.org/10.1144/GSL.SP.1996.101.01.20>
- Zachos, J., Pagani, M., Sloan, L., Thomas, E., & Billups, K. (2001). Trends, Rhythms, and Aberrations in Global Climate 65 Ma to Present. *Science*, *292*(5517), 686–693. <https://doi.org/10.1126/science.1059412>

# Contents

<b>Abstract .....</b>	<b>vi</b>
<b>General audience abstract.....</b>	<b>viii</b>
<b>Dedication .....</b>	<b>x</b>
<b>Acknowledgments .....</b>	<b>xi</b>
<b>Introduction.....</b>	<b>xiii</b>
<b>References.....</b>	<b>xv</b>
<b>CHAPTER 1: Antarctic Bottom Water (AABW) formation history during the Pliocene-Pleistocene from turbidites at IODP Site U1524 (Ross Sea).....</b>	<b>1</b>
<b>Abstract .....</b>	<b>1</b>
<b>1. Introduction .....</b>	<b>2</b>
<b>2. Geologic setting and modern oceanography of the Ross Sea.....</b>	<b>5</b>
<b>3. Paleooceanographic and paleoclimatic evolution .....</b>	<b>7</b>
<b>4. Study Approach.....</b>	<b>10</b>
4.1. <i>Hillary Canyon channel-levee system.....</i>	<i>10</i>
4.2. <i>IODP Site U1524.....</i>	<i>11</i>
4.3. <i>Methods for core characterization.....</i>	<i>14</i>
4.3.1. <i>Occurrence and thickness of the turbidite beds.....</i>	<i>14</i>
4.3.2. <i>Grain-size analysis of the turbidite beds and overlying mud .....</i>	<i>14</i>
4.4. <i>Calculation of density flow properties .....</i>	<i>15</i>
<b>5. Results .....</b>	<b>19</b>
5.1. <i>Turbidite bed occurrence, frequency, and thickness.....</i>	<i>19</i>
5.2. <i>Grain size.....</i>	<i>20</i>

5.3.	<i>Calculated density flow properties</i> .....	21
<b>6.</b>	<b>Discussion</b> .....	<b>23</b>
6.1.	<i>AABW production from the latest Pliocene (~3.3 Ma) to present</i> .....	24
6.2.	<i>Shutdown of DSW-AABW outflow during anomalous late Pliocene interglacial KM3</i> .....	26
6.3.	<i>Antarctic submarine channel-levee systems and dense-water formation</i> .....	27
6.3.1.	Record of high magnitude events only.....	27
6.3.2.	Sediment availability.....	28
6.3.3.	Potential effect of ASC .....	28
<b>7.</b>	<b>Conclusions</b> .....	<b>30</b>
<b>8.</b>	<b>References Cited</b> .....	<b>31</b>
<b>CHAPTER 2: Proximal-distal patterns in density-flow deposits on the Ross Sea continental slope and rise: Sedimentological characterization of Pleistocene deposits from IODP Sites U1524 and U1525</b> .....		<b>47</b>
<b>Abstract</b> .....		<b>47</b>
<b>9.</b>	<b>Introduction</b> .....	<b>48</b>
<b>10.</b>	<b>Geologic setting and modern oceanography of the Ross Sea</b> .....	<b>52</b>
<b>11.</b>	<b>Paleoclimatic evolution during the Pleistocene in the Ross Sea</b> .....	<b>54</b>
<b>12.</b>	<b>Study Approach</b> .....	<b>55</b>
12.1.	<i>Hillary Canyon channel-levee system</i> .....	55
12.2.	<i>IODP Site U1524</i> .....	56
12.3.	<i>IODP Site U1525</i> .....	58
12.4.	<i>Chronology of the turbidite and age models for Sites U1524 and U1525</i> .....	60
12.5.	<i>Methods for Core Characterization</i> .....	60
12.5.1.	Occurrence and thickness of the turbidite beds .....	60
12.5.2.	Grain-size analysis of the turbidite beds and overlying mud.....	61
<b>13.</b>	<b>Results</b> .....	<b>62</b>

13.1.	<i>Turbidite bed occurrence, frequency, and thickness</i> .....	62
13.2.	<i>Grain size</i> .....	64
<b>14.</b>	<b>Discussion</b> .....	<b>66</b>
14.1.	<i>Proximal to distal depositional patterns of the dense shelf water plume from 2.1 to 1 Ma</i> .....	66
14.2.	<i>Depositional variations between ice sheet proximal Site U1525 and distal Site U1524 after 1 Ma</i> ...	67
<b>15.</b>	<b>Conclusions</b> .....	<b>70</b>
<b>16.</b>	<b>References Cited</b> .....	<b>71</b>

**CHAPTER 3: Grain size and compositional characterization of the sedimentary infill of a hydrothermal vent complex in the Vøring Basin, North Atlantic (IODP Hole U1568A): Implications for constraining sedimentary system response to the Paleocene-Eocene Thermal Maximum (PETM).....80**

	<b>Abstract</b> .....	<b>80</b>
<b>17.</b>	<b>Introduction</b> .....	<b>81</b>
<b>18.</b>	<b>Geologic setting</b> .....	<b>86</b>
<b>19.</b>	<b>Study Approach</b> .....	<b>87</b>
19.1.	<i>HTVC formation, timing, and morphology</i> .....	87
19.2.	<i>IODP Hole U1568A and lithostratigraphic units</i> .....	88
19.3.	<i>Chronology, isotope stratigraphy, and sedimentation rate of Hole U1568</i> .....	89
19.4.	<i>Methods for characterization</i> .....	90
19.4.1.	<i>Grain-size analysis of the PETM interval</i> .....	90
19.4.2.	<i>Visual microscopy and SEM imaging</i> .....	92
<b>20.</b>	<b>Results</b> .....	<b>93</b>
20.1.	<i>Bulk grain size</i> .....	93
20.2.	<i>Grain composition and relative abundance</i> .....	94
20.3.	<i>Comparison with the XRF ratios</i> .....	98
<b>21.</b>	<b>Discussion</b> .....	<b>99</b>

21.1.	<i>Sedimentary infill of a marine hydrothermal vent complex environment</i> .....	99
21.2.	<i>Relationship with the PETM timing and sedimentary system response to significant climate change</i> <i>105</i>	
22.	<b>Conclusions</b> .....	<b>107</b>
23.	<b>References Cited</b> .....	<b>108</b>
<b>Appendix A: Chapter 1 R scripts and datafiles</b>		
<b>Appendix B: Chapter 2 R scripts and datafiles</b>		
<b>Appendix C: Chapter 3 R scripts and datafiles</b>		
<b>Appendix D: Chapter 3_Smear Slides descriptions</b>		

# **CHAPTER 1: Antarctic Bottom Water (AABW) formation history during the Pliocene-Pleistocene from turbidites at IODP Site U1524 (Ross Sea)**

Natalia Varela<sup>1</sup>, Brian W. Romans<sup>1</sup>, Zoltan Sylvester<sup>2</sup>, Molly Patterson<sup>3</sup>, Denise Kulhanek<sup>4</sup>, and Rob McKay<sup>5</sup>

1. Department of Geosciences, Virginia Tech, Blacksburg, VA, USA
2. Bureau of Economic Geology, The University of Texas at Austin, Austin, TX, USA
3. Department of Earth Sciences, Binghamton University, Binghamton, NY, USA
4. Institute of Geosciences, Christian-Albrechts-Universität zu Kiel, Kiel, Germany
5. Antarctic Research Centre, Victoria University of Wellington, Wellington, New Zealand

## **Abstract**

The Ross Sea is one of the main producers of dense shelf water (DSW) in the Southern Ocean. Its extended ice shelf and highly productive polynyas can generate large-scale, dense flows that contribute to Antarctic Bottom Water (AABW) formation, the coldest, densest, and deepest water mass in the global ocean. Hillary Canyon, located ~120 km north of the Ross Sea Ice Shelf, is a 500 m deep and 40 km wide submarine canyon-channel system on the continental rise, and one of the largest DSW conduits in the Ross Sea. We propose that the DSW cascading at the shelf edge and down Hillary Canyon triggers sediment-laden turbidity currents and that this linked oceanographic-sedimentary process is recorded in the deposits that have accumulated on the adjacent levees.

Drilled on the crest of the southeastern levee of Hillary Canyon, International Ocean Discovery Program (IODP) Site U1524 recovered a 280 m thick section that encompasses AABW formation history from ~3.3 Ma (late Pliocene) to the present. We identified >3,300 thin-bedded (1.5 mm mean thickness) turbidites, with a sharp lower contact and a distinct yellowish color. Grain size analysis of one-hundred pairs of turbidite beds and their overlying mud shows that the turbidite beds have a median grain size between very fine to medium silt (5-30  $\mu\text{m}$ ), and the overlying mud ranges from very fine to fine silt (6-18  $\mu\text{m}$ ). The overall frequency of the turbidite beds declines

from the Pliocene to the Pleistocene but their sedimentological characteristics do not, which suggests the fundamental process does not vary significantly through time. We integrated these sedimentary parameters with the conduit dimensions obtained from seismic-reflection data and used them as inputs to a Rouse-type model that allowed us to assess suspended sediment concentration and flow velocity of the density currents. Results indicate that these turbidity currents likely had very low suspended sediment concentrations (<1%), and velocities of 0.2 to 0.7 m/s in the thalweg of the channel, which is consistent with modern oceanographic observations, where DSW cascading is driven by changes in salinity and temperature, not by suspended sediment load. Thus, it is possible to link the turbidite record from Site U1524 to AABW formation in the Ross Sea, allowing us to expand the understanding of the physical processes associated with ocean and ice sheet interactions during the last 3.3 Myr. We attribute the high frequency of turbidite events during the latest Pliocene (3.3 to 2.6 Ma) to an overall cooling climate (relative to the early to mid-Pliocene) whereby an expanded West Antarctic Ice Sheet (WAIS) promoted enhanced sea ice-polynya formation and DSW-AABW outflow. Within this late Pliocene phase of intensified AABW formation we document a complete cessation of turbidite events that coincides with a well-documented anomalously warm interglacial episode (Marine Isotope Stage KM3; ~3.17-3.15 Ma), suggesting potential threshold behavior. Our record shows that turbidite frequency diminished significantly in the early Pleistocene to almost no events after ~1 Ma, which we link to reduced continental shelf area as a consequence of a much larger WAIS and a general decline in DSW-AABW production.

## **1. Introduction**

AABW is the coldest (<1°C), densest (>28.27 km/m<sup>3</sup> neutral density), deepest (>1900 m) water mass in the ocean, is a key component in the global thermohaline circulation (Jacobs et al., 1970; Gordon, 1991; Orsi et al., 1999; Orsi, 2002; Gordon et al., 2009; Amblas & Dowdeswell, 2018). Modern AABW forms due to the interaction between the ice sheet and the ocean during the austral winter, and formation is concentrated in the Weddell and Ross Seas, as well as along the Adelie coast and Prydz Bay region (Gordon, 1991; Baines & Condie, 1998; Orsi et al., 1999; Yabuki et al., 2006; Rintoul, 2018). The history of AABW formation in response to climate changes in the middle to late Miocene have been investigated in the Weddell Sea using integrated modelling, deep-sea isotopes, and Antarctic margin seismic stratigraphy (e.g. Huang et al., 2017). However,

the history of AABW formation during the overall cooling of the late Pliocene and early Pleistocene in the Ross Sea sector is poorly understood, and studies are largely restricted to interpretations of deep-sea isotopes ( $\delta^{18}\text{O}$ ) that have a complex signal influenced by a range of competing physical or biological processes. The functioning of AABW outflow during relative warm periods of the past  $\sim 3.5$  Myr is of particular interest in the context of contemporary warming and potential future scenarios. For example, recent modelling studies suggest that enhanced meltwater from retreating ice sheets could potentially slow down AABW overturning by 40% and might feature enhanced incursions of Circumpolar Deepwater (CDW) onto Antarctica's continental shelf further enhancing ice sheet loss (Li et al., 2023).

In the Ross Sea today, the sea ice that forms near the coast is pushed oceanward by strong katabatic winds that flow down the West Antarctic Ice Sheet (WAIS), creating coastal polynyas, or ice-free areas adjacent to the coast (Jacobs et al., 1970; Baines & Condie, 1998). This process allows a continuous ice formation, which increases the salinity of the surrounding seawater and creates a denser water mass (referred to as dense shelf water; DSW). Rapid sinking of this dense water leads to a relatively well-oxygenated water mass (up to 8 mL/L; Gordon, 2001) that ventilates the deeper depths. These resultant denser shelf waters are exported across the continental shelf, can interact with ice shelves to cool further, and are ultimately transported down the continental slope in the form of a descending plume, with flow pathways influenced by topographic features such as submarine canyons (Baines & Condie, 1998; Gales et al., 2021). In some instances, these cascading currents can entrain and resuspend sediment from the outer shelf and upper continental slope, which increases the density of the descending plume further, resulting in a sediment-laden turbidity current (Baines & Condie, 1998; Jacobs et al., 1970). The sediment gravity flow deposits that result (i.e., turbidites) accumulate on the flanks of these conduits and provide a potential record of these linked oceanographic and sedimentary processes across a wide catchment.

To establish a connection between these sedimentary deposits and dense water processes, it is necessary to examine the specific conditions under which they were deposited. The occurrence of these gravity flow-driven events contributes to the construction of depositional levees adjacent to a channel due to "flow stripping" (Piper & Normark, 1983), whereby the upper part of a turbidity current spills over and out of the confined area, leading to sediment accumulation on the overbank

region (Straub & Mohrig, 2008). International Ocean Discovery Program (IODP) Site U1524, one of the five sites cored in the Ross Sea during Expedition 374 in 2018 (Fig. 1a), is located at the crest of one of the levees of Hillary Canyon, one of the three primary conduits for modern AABW outflow in the Ross Sea and, thus, presents a unique archive of past AABW formation in one of its largest global source areas. The high recovery (94%) of this site contains one of the most continuous and complete Antarctic continental-rise records of the mid-Pliocene (~3.3 Ma) to the present (McKay et al., 2019).

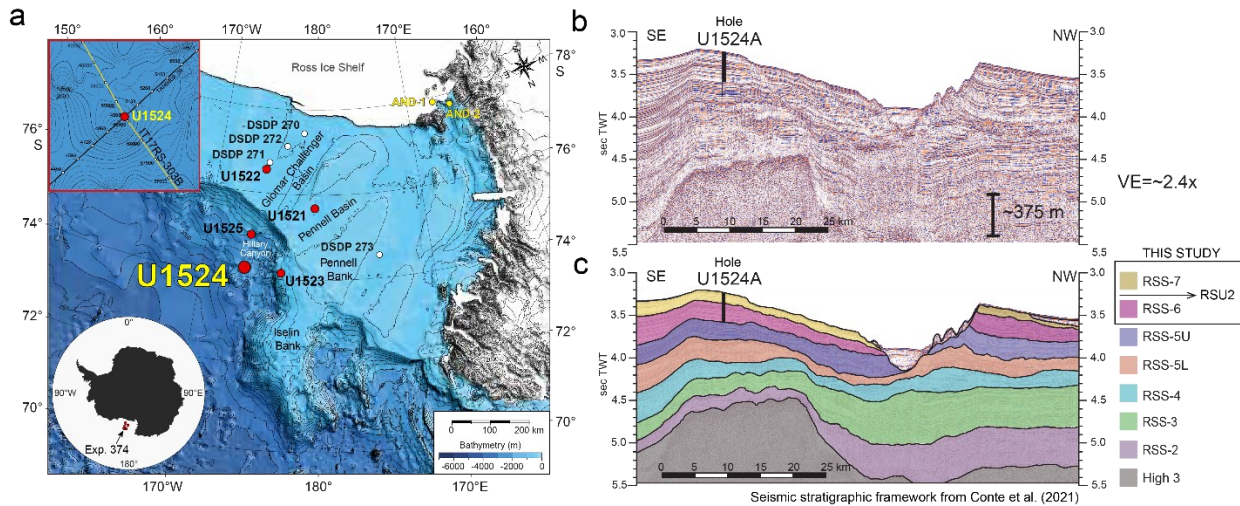


**Figure 1.** (a) Bathymetric map with the location of Site U1524, other IODP Expedition 374 sites (red dots), Deep Sea Drilling Project (DSDP) Leg 28 sites, and Antarctic Geological Drilling Project (AND) drill cores. The red box shows a zoomed-in location of the seismic line IT17RS-303B (yellow line). Modified from McKay et al. (2019). (b) Seismic profile line IT17RS-303B with the location of Hole U1524A. Modified from McKay et al. (2019). (c) Interpretation of Ross Sea seismic Sequences (RSS) by Conte et al. (2021). This study focuses on Hole U1524A, that includes RSSs 6 and 7, separated by the Ross Sea Unconformity (RSU) 2.

Here, we propose that dense shelf water cascading in Hillary Canyon was the main trigger for the initiation of turbidity currents and that thin (<1 cm) turbidite beds (Fig. 2) within the mud-dominated succession at IODP Site U1524 record the history of AABW formation in the Ross Sea. Our analysis focuses on sedimentological characterization including grain size, composition, thickness, and frequency of the interpreted turbidite beds. In addition, we use our sedimentological parameters combined with Hillary Canyon dimensions based on seismic-reflection data as inputs to a Rouse-type model to estimate suspended sediment concentration, flow velocity, and flow height of the formative density currents. We interpret our results in the context of the mid-

Piacenzian/mid-Pliocene warm period (3.264-3.025 Ma) (Dowsett et al., 2013) and climatic evolution during the Plio-Pleistocene transition. Finally, we discuss the potential of this physical proxy of dense water outflow along the Antarctic margin, including limitations and uncertainties.

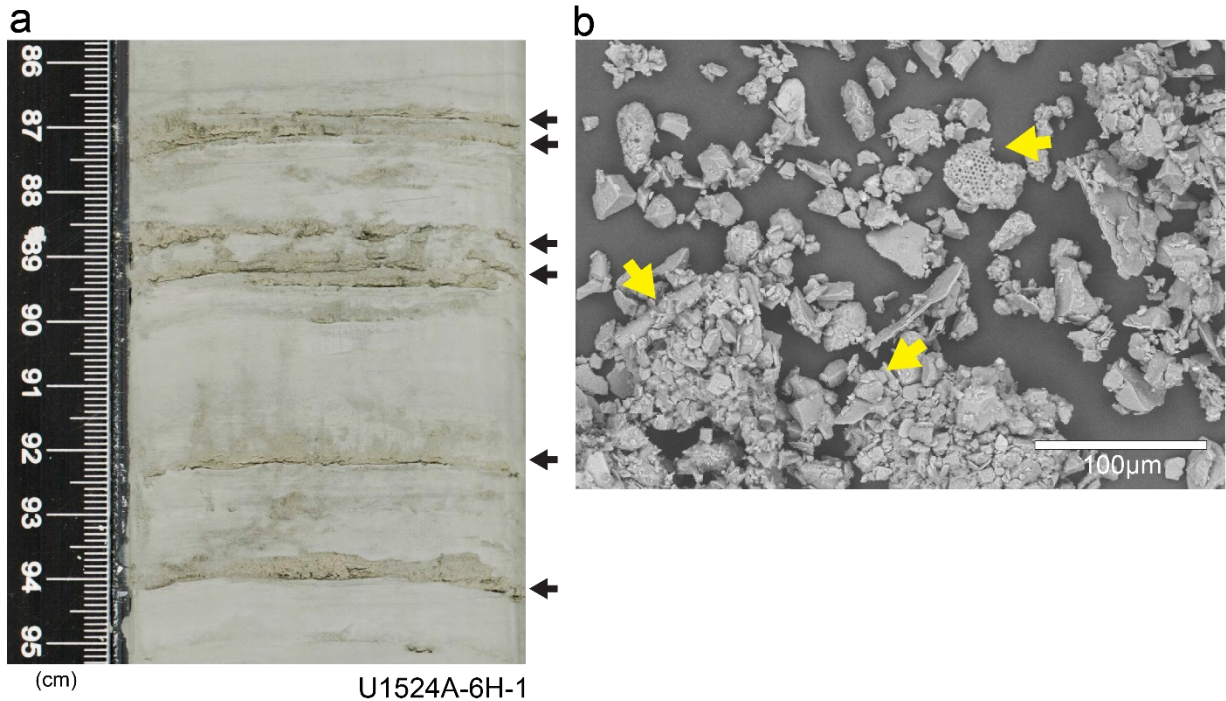


**Figure 2.** (a) Core photo (U1524A-6H-10; 86-95 cm) with black arrows denoting interpreted turbidite beds. Scale in cm. The yellowish color is one of the main characteristics, along with a sharp bottom contact and the flame-like structures on top. The mean thickness of the turbidites is 1.5 mm. (b) SEM image of the bulk sediment from a turbidite layer, showing the highly fragmented biogenic material (yellow arrows), mostly diatoms. The terrigenous fraction is highly angular.

## 2. Geologic setting and modern oceanography of the Ross Sea

The Ross Sea is one of the major drainage zones for the WAIS (Jacobs et al., 1970; De Santis, 1999; Bergamasco et al., 2002; Budillon et al., 2002; Gordon et al., 2004; Budillon et al., 2011; Silvano et al., 2020). The creation of the embayment that is the Ross Sea is linked to crustal thinning and associated rifting that began ~120 Ma with the breakup of Gondwana and the development of the Western Antarctic Rift System, although rifting has largely ceased by middle Miocene times in all but the westernmost Ross Sea (De Santis, 1999; M. McKay et al., 2022). The eastern region of the Ross Sea is now a passive margin, and sediment supply here is largely a function of ice sheet erosion and sedimentation, biological productivity, and reworking by ocean

currents and consequently serves as an archive for the past interactions between the WAIS and the ocean during the last 65 Myr (De Santis, 1999; McKay et al., 2019).

Three main water masses interact in the modern continental margin region of the Ross Sea: Antarctic Surface Water (AASW; density  $<28 \text{ kg/m}^3$ ), Circumpolar Deep Water (CDW; density between  $28\text{-}28.27 \text{ kg/m}^3$ ), and AABW (density  $>28.27 \text{ kg/m}^3$ ) (Gordon et al., 2009; Orsi & Wiederwohl, 2009; Morrison et al., 2020; Conte et al., 2021). CDW, the greatest water mass by volume in the Southern Ocean, originates from the relatively warm and salty mid-depth range and is transported from the subtropical regions of the Southern Ocean (Whitworth III et al., 1998; Orsi & Wiederwohl, 2009). The Antarctic Circumpolar Current (ACC) drives part of CDW to the east, while the remaining volume enters the Ross Gyre, embedded between the colder AASW and AABW below (Whitworth III et al., 1998; Orsi & Wiederwohl, 2009). This overall three-layer structure results in warmer waters flowing into the Ross Sea (Gordon et al., 2009; Conte et al., 2021). When the warm CDW loses heat as it moves poleward, a modified CDW (mCDW; density between  $28.10$  to  $28.27 \text{ kg/m}^3$ ) develops, with similar density but cooler than CDW and separated from it by a  $1.5^\circ\text{C}$  isotherm (Orsi & Wiederwohl, 2009; Shadwick et al., 2014; Silvano et al., 2018; Morrison et al., 2020). This mCDW supplies the shelf area with warmer, less-dense waters (Williams et al., 2010; Morrison et al., 2020), that contribute to the formation of Dense Shelf Water (DSW; density  $<28 \text{ kg/m}^3$ , temperature  $<1.7^\circ\text{C}$ , Whitworth III et al., 1998). The transport of CDW/mCDW onto the continental shelf is modulated by a strong gradient of water properties known as the Antarctic Slope Front (ASF) (Gill, 1973; Jacobs, 1991; Baines, 2009; Thompson et al., 2018), a hydrographically dense boundary between the CDW and the shelf waters, that is coupled with the westward flowing Antarctic Slope Current (ASC) (Jacobs, 1991; Thompson et al., 2018, 2020). The ASC and the ASF control the heat transport and other properties, between the continental shelf waters and the warmer mCDW (Jacobs, 1991; Whitworth III et al., 1998; Baines, 2009; Thompson et al., 2018, 2020).

Dense shelf water is a product of sea ice formation on the Antarctic shelf, which, in turn, causes the loss of heat and the increase of salinity in the remaining water due to brine rejection (Baines & Condie, 1998; Gordon et al., 2004; Morrison et al., 2020). The mixing of the denser, saltier, and colder DSW with the warmer upwelled mCDW downslope allows the production of AABW in the

Southern Ocean (Whitworth III et al., 1998; Baines, 2009; Morrison et al., 2020), but this process is limited to a few places in Antarctica.

The Ross and Weddell seas are the main producers of DSW in the modern Southern Ocean (Orsi et al., 1999; Orsi, 2002; Orsi & Wiederwohl, 2009). Their large ice shelves and highly productive polynyas, in addition to the deep and wide continental shelves crossed by large depressions, can accumulate and export large volumes of DSW (Foldvik et al., 2004; Gordon et al., 2004; Ivanov et al., 2004). The continental shelf of the Ross Sea has an average width of ~240 km, a maximum width of ~400 km, and 63% of its ~380,000 km<sup>2</sup> area deeper than the mean water depth (460 m) of the entire Antarctic continental shelf (Amblas & Dowdeswell, 2018). These physiographic characteristics are ideal for the development of large-scale dense flows that contribute to AABW formation, known in this area as Ross Sea Bottom Water (RSBW) (Orsi et al., 1999; Orsi, 2002; Ivanov et al., 2004; Gordon et al., 2015; Amblas & Dowdeswell, 2018). The RSBW is the coldest (-0.3 to 0°C) and saltiest type (34.7-37.72 PSU) of bottom water formed in the Southern Ocean, with a neutral density > 28.27 kg/m<sup>3</sup> (Jacobs et al., 1970; Orsi & Wiederwohl, 2009; Basak et al., 2015). The neodymium isotopic signature of the RSBW ( $\epsilon_{Nd} \sim -7$ ) shows that this water mass can be traced into the Southeast Pacific (Basak et al., 2015), extending its influence outside of the Ross Sea. Therefore, the reconstruction of AABW formation history in the Ross Sea, one of its key production sites, provides an opportunity to study the response and influence of ocean-ice sheet interactions to past climate change at a global relevant scale.

### **3. Paleoceanographic and paleoclimatic evolution**

During the Cenozoic, Antarctica underwent a transition from a nearly ice-free landscape in the Eocene to the ice-covered continent we see today. The global cooling associated with the Eocene-Oligocene Transition (EOT; ~34 Ma) is thought to represent the most significant change, including large-scale ice-sheet expansion based on geological evidence from land-based outcrops and marine sediment cores from the continental margin at multiple locations in Antarctica (Barrett, 1989; Hambrey et al., 1991; Zachos et al., 1992; M. McKay et al., 2022). The rapid growth of the Antarctic Ice Sheet (AIS) increased the transport of the intermediate waters further north, while enhancing AABW formation (Goldner et al., 2014). Following the EOT and early Oligocene, Antarctica experienced additional ice-sheet expansion from the middle Oligocene through the

Miocene, but with notable punctuations including development of large marine terminating ice sheet across the Oligocene/Miocene boundary and in the Early Miocene (Naish et al., 2009; Marschalek et al., 2021; Duncan et al., 2022). The Miocene Climatic Optimum (MCO; ~ 17–14.7 Ma) (Flower & Kennett, 1994; Flower, 1999) was a global warming episode (~6°C; Flower et al., 2004) that resulted in AIS retreat (Sangiorgi et al., 2018), Southern Ocean warming (Shevenell et al., 2004, 2008; Holbourn et al., 2015), and a reduction of AABW formation (Huang et al., 2017). The ice sheet subsequently expanded, reaching a higher ice volume than the modern during the significant cooling of the Middle Miocene Climatic Transition (MMCT; 14.5–13 Ma) (Flower & Kennett, 1995; Hall et al., 2003; Lear et al., 2015). Proxy studies (Flower & Kennett, 1995; Lear et al., 2000; Sugden & Denton, 2004; Lewis et al., 2007; Lear et al., 2015; Chorley et al., 2022) and models (Huang et al., 2017; Leutert et al., 2021) suggest that ice sheet expansion created the conditions for enhanced AABW formation during the MMCT.

The Pliocene (5.33-2.58 Ma) was a transitional time, from a globally warmer-than-present early Pliocene (~5-3 Myr ago) (Naish et al., 2009), with a mean annual temperature ~3-4°C higher than today (Haywood & Valdes, 2004; Pagani et al., 2010; Dowsett et al., 2013; Prescott et al., 2014), with major cooling steps in the late Pliocene (~3.3 Ma) and Pleistocene (e.g. Naish et al., 2009, McKay et al., 2012). In the Southern Ocean, the cooling trend started between 3.3 and 2.6 Ma, potentially helping to contribute to a drawing down of atmospheric CO<sub>2</sub> from ~400 to 280 ppm (McKay et al., 2012). Within this overall cooling is the interval between 3.264-3.025 Ma, known as the mid-Pliocene or mid-Piacenzian Warm Period (mPWP; Fig. 4), considered one of the best analogs for the future climatic scenarios (Draut et al., 2003; Dowsett et al., 2013; Haywood et al., 2016), and the focus of the PRISM project (Pliocene Research, Interpretation, and Synoptic Mapping). Atmospheric CO<sub>2</sub> concentrations during the mPWP was similar to today's (~415 ppm; Pagani et al., 2010) and the overall tectonic, paleobathymetric, and oceanographic configurations were generally similar to the present (e.g. Draut et al., 2003; Dowsett et al., 2013). However, studies from this time period show that the Greenland Ice Sheet and the WAIS were significantly reduced, contributing to a sea level up to 25 m higher than the present (Miller et al., 2012; Dowsett et al., 2013), and recent simulations on the EAIS stability, proxy studies, and far-field sea level records indicate a larger contribution of Antarctic ice sheets to sea level rise than previously considered (Cook et al., 2013; Austermann et al., 2015; Grant et al., 2019). Coupled Atmosphere-

Ocean General Circulation Models (AOGCMs; e.g., Haywood & Valdes, 2004), indicate a slightly weaker thermohaline circulation, a shallower formation depth for the NADW, higher input of Lower CDW, and reduced outflow of the AABW especially in the Pacific Ocean without a significant heat transport from the atmosphere or the oceans (Billups et al., 1997; Haywood & Valdes, 2004; McKay et al., 2012). However, these results contradict some of the interpretation of carbon isotope ( $\delta^{13}\text{C}$ ) from benthic foraminifera and bottom water temperature records that explain the warming in higher latitudes to be the result of enhanced thermohaline circulation (Raymo et al., 1996; McKay et al., 2012; Woodard et al., 2014; Patterson et al., 2018) .

The relatively warm mPWP that interrupted the overall cooling of the late Pliocene ended by  $\sim 2.7$  Ma with marine and terrestrial records indicating the global cooling trend characteristic of the Pliocene-Pleistocene transition (Lisiecki & Raymo, 2007). In the Ross Sea, after  $\sim 2.6$  Ma, the more negative values ( $-27\text{‰}$ ) of  $\delta^{13}\text{C}$  from an ANDRILL sediment core (AND-1B; Fig. 1a) recovered beneath the Ross Ice Shelf, indicate enhanced development of a polynya-style mixing that would have favored AABW production (McKay et al., 2012). In the southern hemisphere circulation, over the past 1.2 Myr (Marine Isotopic Stages, 35-34), the supply of deep waters from the Southern Ocean into the Pacific has been primarily carried by the deep western boundary current (DWBC), flowing east of New Zealand (Hall et al., 2001). ODP site 1123 showed physical (sortable silt mean size) and isotopic evidence that during glacials there was an increase in DWBC flow and greater Pacific ventilation, associated directly with a higher formation rate of AABW, when compared with interglacials (Hall et al., 2001). However, how the overall AABW outflow changed from the late Pliocene and through the Pleistocene has not been documented.

The climatically driven advances and retreats of the WAIS during the past  $\sim 35$  Myr have left behind an incomplete record of the ocean-ice sheet interactions on the continental shelf, as revealed by several regional unconformities in the Ross Sea (De Santis, 1999; McKay et al., 2012; Naish et al., 2009; Conte et al., 2021). Therefore, a more complete history of AABW formation and outflow during the climate states and variability of the late Pliocene and Pleistocene may lie further offshore, in the sedimentary archives left behind by the dense shelf water plume cascading down Hillary Canyon.

## 4. Study Approach

### 4.1. Hillary Canyon channel-levee system

Hillary Canyon is a 180 km long submarine conduit on the eastern Ross Sea continental margin that shows erosional canyon morphology at the shelf edge and continental slope (Gales et al., 2021) transitioning to depositional channel-levee morphology on the continental rise (Conte et al., 2021). Several deep, glacially sculpted troughs sever the continental shelf landward of the Hillary Canyon, which stretches for around ~300 kilometers to the front of the Ross Ice Shelf today. The head of the canyon sits on the shelf edge, at the juncture of the Pennell Trough and Glomar Challenger Basin, making Hillary Canyon a pathway for the glacial sediments exported from the continental shelf interior through ice streams (De Santis, 1999; Gales et al., 2021). Sediments are delivered downslope through gravity flows (Baines & Condie, 1998; Shapiro, 2003; Ivanov et al., 2004; Gordon et al., 2009; Gales et al., 2021), with a mixture of sediments and highly saline waters (DSW and mCDW), that are interpreted to contribute to the formation of the levees of Hillary Canyon further down-system due to the overspill of the suspended load downstream through “flow stripping” (Piper & Normark, 1983). IODP Site U1524 is located on the crest of the eastern levee, ~120 km from the continental shelf edge and ~100 km from the base-of-slope (Fig. 1a).

Regional seismic-stratigraphic mapping and reconstruction of the Ross Sea sedimentation history provides important context for our core-based study. Conte et al. (2021) identified eight seismic sequences (Ross Sea Sequences; RSSs; Fig. 1c) using new seismic, morpho-bathymetric, and oceanographic data acquired in a 2017 campaign onboard the R/V OGS Explora, in combination with sediment cores, well log data and the age model from IODP sites U1523 and U1524 (Expedition 374). In the eastern Ross Sea, these RSSs are limited by the regional unconformities (Ross Sea Unconformities; RSUs) defined by seismic reflectors interpreted as advances and retreats of the WAIS (De Santis, 1999). The sequences reveal the evolution of Hillary Canyon from the Late Oligocene to the Pleistocene and the overall effect of bottom currents, dense shelf water cascading, and sediment supply in the system, all of which can be linked to climatic variations. The onset of active gravity flow deposits in the early Miocene (17-14.5 Ma; deposition of RSS-4) allowed the building up of the levees of the Hillary Canyon. The thickening of RSS-4 hints at stronger bottom currents acting in the Iselin Bank and the continental rise connected to the

higher input of sediment through the action of turbidity currents. During the Middle to Late Miocene, (14.5-8 Ma; deposition of RSS-5), there is an enhancement of the biogenic sediment supply from the shelf that would have been funneled down the Hillary Canyon, and is reflected by the growth of the sedimentary mounds (De Santis et al., 1999; Conte et al., 2021). A hiatus followed during the Late Miocene (8-5 Ma; RSU-3), due to the action of highly erosive bottom currents and lack of deposition in the shelf and the rise. This bottom current activity and DSW production diminished towards the Pliocene (RSS-6), presumably due to the mPWP (~3.3-3 Ma), weakening the Antarctic Slope Front (Conte et al. 2021). By the Pleistocene (deposition of RSS-7), the cooling period that came after the warming in the Pliocene, is interpreted by Conte et al., 2021 to have invigorated the bottom current activity, and promoted the formation of polynyas and sea ice (McKay et al., 2012) one of the driving mechanisms for the AABW formation derived from the Ross Sea continental shelf.

#### *4.2. IODP Site U1524*

IODP Site U1524 (74°13.05'S, 173°37.98'W), is 120 km north of the continental shelf edge at 2934 m water depth, on the southeastern levee crest of Hillary Canyon (McKay et al., 2019). In this area, the vertical relief from the thalweg to the levee crest is ~500 m, the width of the channel thalweg is 5 km, and the width of the entire channel system, from levee crest to crest, reaches up to nearly ~45 km (Fig. 1b). The Upper Miocene to Pleistocene sediments recovered from the three holes at this site are characterized by three lithostratigraphic units (LSUs I-III; in Figs. 3a and 4a), from dominantly diatom-rich mud at the base of the core (LSU III) to relatively more terrigenous-rich sediment towards the top (LSU I) (McKay et al., 2019). Hole A, studied here, was drilled up to 282.35 m core depth below the seafloor (CSF-A), with the upper 270.3 m using piston coring and the remaining section with an extended core barrel system. The continuous and complete sedimentary record of Hole A (94% recovery), which spans from the late Pliocene (~3.3 Ma) through the Pleistocene, is the primary focus of this study.

The dominant lithologies at Site U1524 (Fig. 3a) are diatom-bearing/rich mud/sandy mud, muddy diatom ooze, and muddy diamict. All the contacts between units and subunits are mostly gradational, with a downhole increase in diatom content. The turbidite beds are present in Units I and II. Unit I consist of ~200 m of upper Pliocene to Pleistocene, and is subdivided into subunits

IA, IB, and IC, based on their relative biogenic content. The overall lithology is unconsolidated interbedded massive to laminated diatom-bearing/rich mud, sandy mud, and muddy diatom ooze. A sharp contact between diatom-rich mud and muddy diatom ooze, divides Unit I from Unit II, respectively. Unit II consists of ~117 m of massive to laminated olive-gray muddy diatom ooze interbedded with bioturbated to laminated greenish-gray diatom ooze and diatom-rich sandy mud. The turbidites observed in Hole A (Fig 2) have a distinctive light yellow-gray color, which sharply contrasts with the overall gray-to-brown background, and have sharp basal contacts. The upper contact of the beds commonly has irregular shapes, in some cases resembling flame-like structures.

This study uses the core depth below seafloor method A (CSF-A) as the depth scale (McKay et al., 2019). To estimate the age of each bed, we employed a combination of paleomagnetic and biostratigraphic data obtained from IODP Expedition 374, using linear interpolation techniques (McKay et al., 2019).

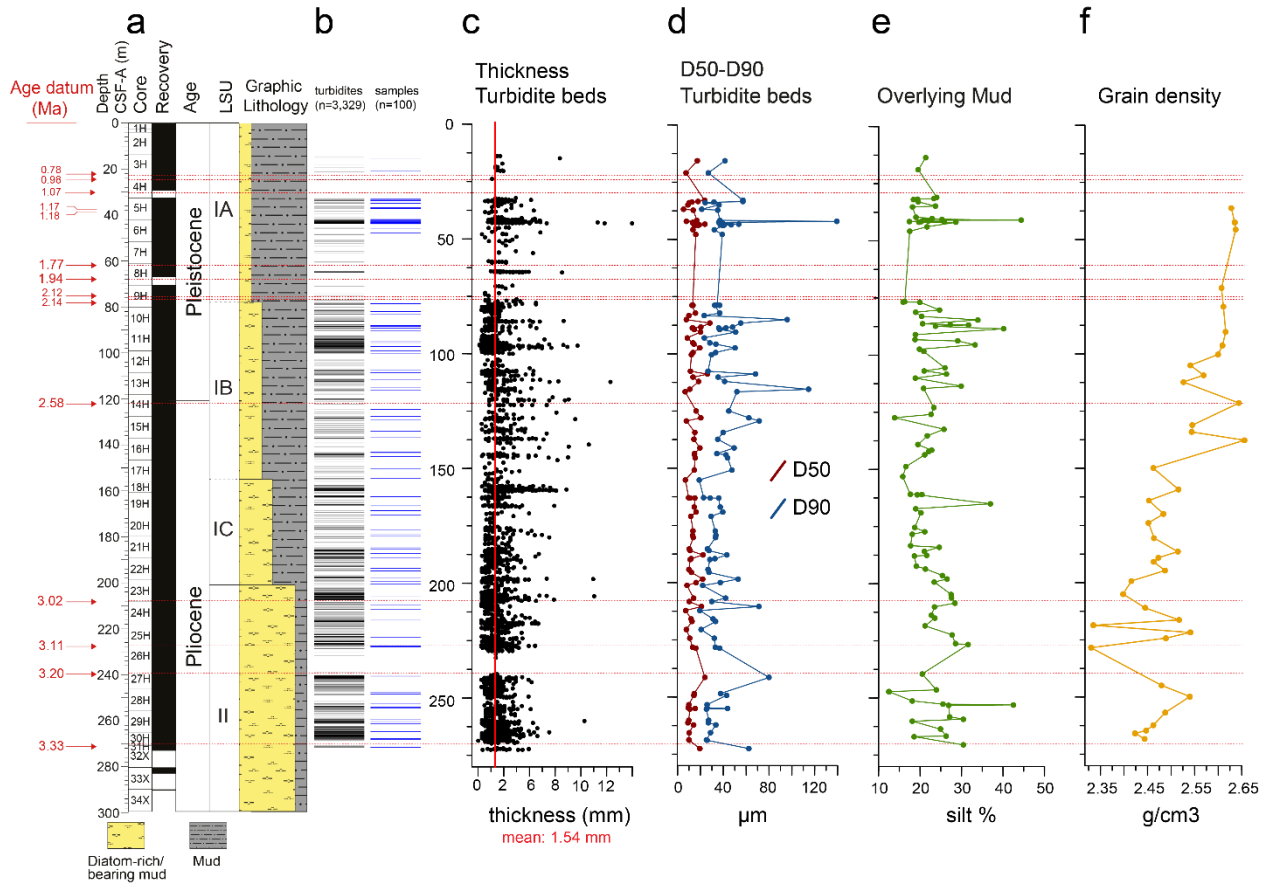


**Figure 3.** (a) Stratigraphic context for IODP Site U1524 (CSF-A in meters). Age datums (in red numbers) are denoted by the red dotted lines. Modified from McKay et al. (2019). (b) Stratigraphic position of all ( $n=3,329$ ) turbidites with sampled beds ( $n=100$ ) shown in blue. (c) Thickness of each turbidite bed. The red line represents the mean thickness (1.54 mm). (d) Grain size analysis of one-hundred paired samples of turbidites and overlying mud is characterized by D50 (red) and D90 (blue) of turbidite beds (in  $\mu\text{m}$ ) (e) Silt percentage (%) of the overlying mud. (f) Shipboard grain density data within 5 cm above and below the sampled turbidite layers.

### *4.3. Methods for core characterization*

The sedimentological characterization of the turbidite beds in Hole U1524A focuses on three parameters: the stratigraphic position and total number of turbidite beds, the thickness of the turbidite beds, and the grain size of a representative sampling of the turbidite beds and the mud directly overlying these beds through the succession (n= 100 pairs of samples).

#### *4.3.1. Occurrence and thickness of the turbidite beds*

We visually identified the beds in high-resolution core photographs and, using a custom MATLAB script, recorded the position of the base and top of each bed, which allowed for determination of bed thickness. During this process, we also evaluated the lateral continuity of the bed across the core and other descriptive characteristics of these turbidite beds (e.g., nature of bed contacts). The depth midpoint of each bed was converted to an age through linear interpolation using the shipboard age model as mentioned above.

#### *4.3.2. Grain-size analysis of the turbidite beds and overlying mud*

We systematically identified and selected one hundred pairs of turbidite beds and their corresponding overlying mud intervals to serve as representatives of the sedimentological variations observed throughout the core. This selection encompasses variations in bed thickness and lateral continuity, providing a comprehensive overview of the sedimentary features in the interval of interest. We sampled those turbidite beds from the core using a 10 cm<sup>3</sup> wedge plastic tool, and a 20 cm<sup>3</sup> half-round plastic scoop for the overlying mud.

To characterize the grain size distributions of the turbidite beds, we used a laser particle analyzer (Malvern MasterSizer 3000). The average amount of sediment obtained from each bed was up to 2 g. Since the sediment was non-cohesive and homogeneous silty material, no chemical treatment was necessary, and we measured it directly on the laser particle analyzer. We manually poured the sediment into the wet dispersion unit until it reached a stable obscuration range of 8-10%. Each sample was measured three times using the instrument's sequence. If the sample showed irregular distribution during the measurements (i.e., large variations between each of the three measurements), additional measurements were taken up to 6 times, if necessary, to ensure data quality. The output data was processed using Gradistat version 9.1 (Blott & Pye, 2001), and

the results are displayed in volume percentage. We summarize the grain-size data by calculating the median (50<sup>th</sup> percentile; D50) and the 90th percentile (D90) from the distributions.

To assess the nature of the finer-grained deposits directly overlying the turbidite beds, we generated grain size data using the Micromeritics SediGraph 5100. The SediGraph is a preferred method for clay-rich sediments (1-63  $\mu\text{m}$  fraction) because it measures particle size based on particle settling velocity following Stokes' law, reducing inaccuracies due to the particle shape effect (McCave & Hall, 2006). Before analysis, we wet-sieved the sample at 63  $\mu\text{m}$ , dried the coarser (>63  $\mu\text{m}$ ) fraction in an oven at 50°C for 48 hours, and then weighed it to calculate the mass percentage of the sand fraction. The finer (<63  $\mu\text{m}$ ) fraction was also dried and weighed, and 1 g was analyzed in the SediGraph. We dispersed the sample in 5 ml of 10% NaOH solution before pouring it into the SediGraph chamber to aid deflocculation. We processed the SediGraph output files with a custom R script to calculate the proportion of silt (4-63  $\mu\text{m}$ ) by mass in these clay-rich sediments.

#### *4.4. Calculation of density flow properties*

Regardless of whether the density flows in Hillary Canyon and on the surrounding slopes are driven by excess density due to water temperature and/or salinity or to suspended sediment - or a combination of the two - sediment deposition on the seafloor is driven primarily by sediment concentration and rate of deposition. To reconstruct the characteristics of the flows, we use a simple model of sedimentation that relies on a Rouse-type concentration profile and an Exner equation that considers both deposition and entrainment.

The Rouse equation (Rouse, 1938) describes the variation of suspended sediment concentration in a flow as a function of height above the bed:

$$C_z = C_a \left( \frac{h-z}{z} \frac{z_a}{h-z_a} \right)^{Ro}, \quad (1)$$

Where  $C_z$  is the sediment concentration at height  $z$  in the current,  $C_a$  is the concentration at a reference height  $z_a$  that is close to the bed,  $h$  is the current thickness, and  $Ro$  is the Rouse number defined as:

$$Ro = \frac{w_s}{ku^*}, \quad (2)$$

In the definition of the Rouse number above,  $w_s$  is the settling velocity,  $k$  is von Karman's constant ( $= 0.4$ ), and  $u^*$  is the shear velocity. The settling velocity can be computed using the following relation (Ferguson & Church, 2004):

$$w_s = \frac{RgD^2}{C_1\nu + \sqrt{0.75C_2RgD^3}}, \quad (3)$$

where  $R$  is the specific submerged gravity,  $g$  is gravitational acceleration,  $D$  is the particle diameter,  $C_1$  and  $C_2$  are constants with theoretical values of 18 and 1, and  $\nu$  is the kinematic viscosity of water. Shear velocity is calculated as:

$$u^* = U\sqrt{C_f}, \quad (4)$$

where  $U$  is the mean velocity of the flow and  $C_f$  is the friction factor.

The Rouse concentration profile was developed for open-channel flow and it is well known that suspended sediment concentration in a turbidity current decline more gradually than a Rouse profile would predict (Altinakar et al., 1996; Kneller & Buckee, 2000; Sequeiros et al., 2010). However, the Rouse equation has been used successfully to model deposition on submarine levees (Straub & Mohrig, 2008); and recent work has shown that the divergence between grain size and concentration profiles of experimental turbidity currents and the corresponding Rouse profiles are relatively small, especially for finer grain sizes (Eggenhuisen et al., 2020).

Deposition of sediment is modeled as the product of settling velocity  $w_s$  and concentration  $C_z$ , with the porosity  $\phi$  taken into account (e.g., Garcia, 1990):

$$\frac{dh}{dt} = \frac{(C_z - E_z)w_s}{1 - \phi}. \quad (5)$$

The term  $E_z$  is the sediment entrainment coefficient and accounts for the fact that, at higher current velocities, a significant part of the sediment that settles toward the bed gets re-entrained into the body of the flow. It is computed using the empirical approach of Garcia and Parker (1991) \*see also Sylvester et al., submitted). Shear stress and grain size are among the key factors that determine entrainment; and shear stress decreases away from the channel or canyon thalweg, because flow velocities decrease as well (e.g., de Leeuw et al., 2018). In our model, we assume a simple linear decrease of shear velocity with height above thalweg. This decrease means that entrainment is important at the bottom of the canyon but close to zero high up on the levees, where the sediment data for Site U1524 comes from.

Based on observations at Site U1524, we use two grain size classes: a coarser fraction, with an initial grain size range of 0.02 – 0.08 mm (20-80  $\mu\text{m}$ ), and a finer fraction (mud), with an initial grain size range of 0.005 – 0.02 mm (5-20  $\mu\text{m}$ ). Both sediment classes are assumed to be deposited by the same flows; however, the mud fraction is easily transported by any bottom-hugging turbidity current and it is less useful when it comes to constraining flow parameters.

An important question is whether advection settling away from the canyon plays a significant role in the formation of the overbank stratigraphy at Hillary Canyon. In the model used here, a generalized version of the advection settling model of Straub and Mohrig (2008) has been implemented and it can be used to limit the lateral extent of levee deposition (Sylvester et al., submitted). However, the southeastern side of Hillary Canyon does not have a typical gullwing levee geometry; instead, it shows significant thickening away from the canyon. This suggests that sediment is not entirely sourced from conventional canyon-related overbank flows at this location. Therefore, in the simulations presented here, we do not apply the advection settling correction and the resulting layers are laterally extensive over tens of kilometers, mimicking the geometries observed in the seismic section.

Despite its simplicity, the model relies on a large number of parameters (Table 1). Some of these parameters are known; many others are unknown. Six unknown parameters (mean flow velocity, duration of deposition, reference concentration for the coarser and finer sediment classes, and grain sizes of the coarser and finer sediments) have a significant effect on the resulting deposit. We used Latin hypercube sampling (LHS; McKay et al., 1979) to run 100,000 simulations that cover the likely ranges of these parameters (Table 2). Then we check which parameter combinations match the observations at Site U1524, in terms of bed thickness and grain size on the levee crest.

**Table 1.** Parameters and their typical values used in the model.

<b>Symbol</b>	<b>Name</b>	<b>Value</b>	<b>Units</b>
g	gravitational acceleration	9.81	m / s <sup>2</sup>
k	von Karman constant	0.4	
C <sub>f</sub>	friction coefficient	0.003	
C <sub>1</sub> , C <sub>2</sub>	constants in grain settling equation	18, 1	
μ	viscosity of water	0.001002	N s / m <sup>2</sup>
ρ <sub>p</sub>	density of particles	2300.0	kg / m <sup>3</sup>
ρ <sub>f</sub>	density of water	1027.0	kg / m <sup>3</sup>
U	mean flow velocity	0.5	m / s
T	duration of deposition	15000	s
C <sub>as</sub>	reference concentration of coarser sediment	0.0002	
C <sub>am</sub>	reference concentration of finer sediment	0.005	
D <sub>s</sub>	coarser grain size	0.04	mm
D <sub>m</sub>	finer grain size	0.010	mm
h	flow depth	700	m
θ	porosity	0.4	
z <sub>a</sub>	reference height	0.01	m
E <sub>f</sub>	entrainment factor	1.0	
u* <sub>f</sub>	shear velocity factor	0.5	
dt	time step	50	s

**Table 2.** Likely ranges of the important unknown parameters; these ranges were used in the LHS experimental design.

Symbol	Name	Range	Units
U	mean flow velocity	0.05 – 1.5	m / s
T	duration of deposition	100 – 20000	s
C <sub>as</sub>	reference concentration of coarser sediment	0.0001 – 0.05	
C <sub>am</sub>	reference concentration of finer sediment	0.0001 – 0.05	
D <sub>s</sub>	coarser grain size	0.02 – 0.08	mm
D <sub>m</sub>	finer grain size	0.005 – 0.02	mm

## 5. Results

### 5.1. Turbidite bed occurrence, frequency, and thickness

We identified a total of 3,329 turbidite beds between 15.6 and 272.4 m CSF-A (Fig. 3b). The occurrence of these beds is highest in the lower lithostratigraphic units (II, IC, and the lower half of IB), with systematically fewer towards the top of the succession. There are a few intervals in the upper part that have a higher number of beds (e.g., 85-100 m CSF-A) and we note that although the uppermost 15 m is finely laminated in places, there are no distinctly light yellow-gray beds with a clearly coarser grain size. Additionally, although the lower part of the core has the highest occurrence of beds, there is a notable lack of turbidite beds between 230 and 240 m CSF-A. When considered in the time domain (Fig. 4), the highest frequency of these turbidite beds is found between 3.32 to ~2.11 Ma (late Pliocene to earliest Pleistocene), systematically decreasing until a high-frequency peak at ~1.3 Ma (mid-Pleistocene), followed by a significant decline during the last ~1 Myr (Fig. 4d).

The thickness of the turbidite beds ranges from 0.4 mm to 6 mm, with rare exceptions greater than 6 mm (Fig. 3c). The average and median thicknesses are 1.54 mm and 1.29 mm, respectively. Although there are concentrations of thicker beds at approximately 160 m, 100 m, and 45 m CSF-A, the thickness of the turbidite beds generally remains consistent throughout the succession.

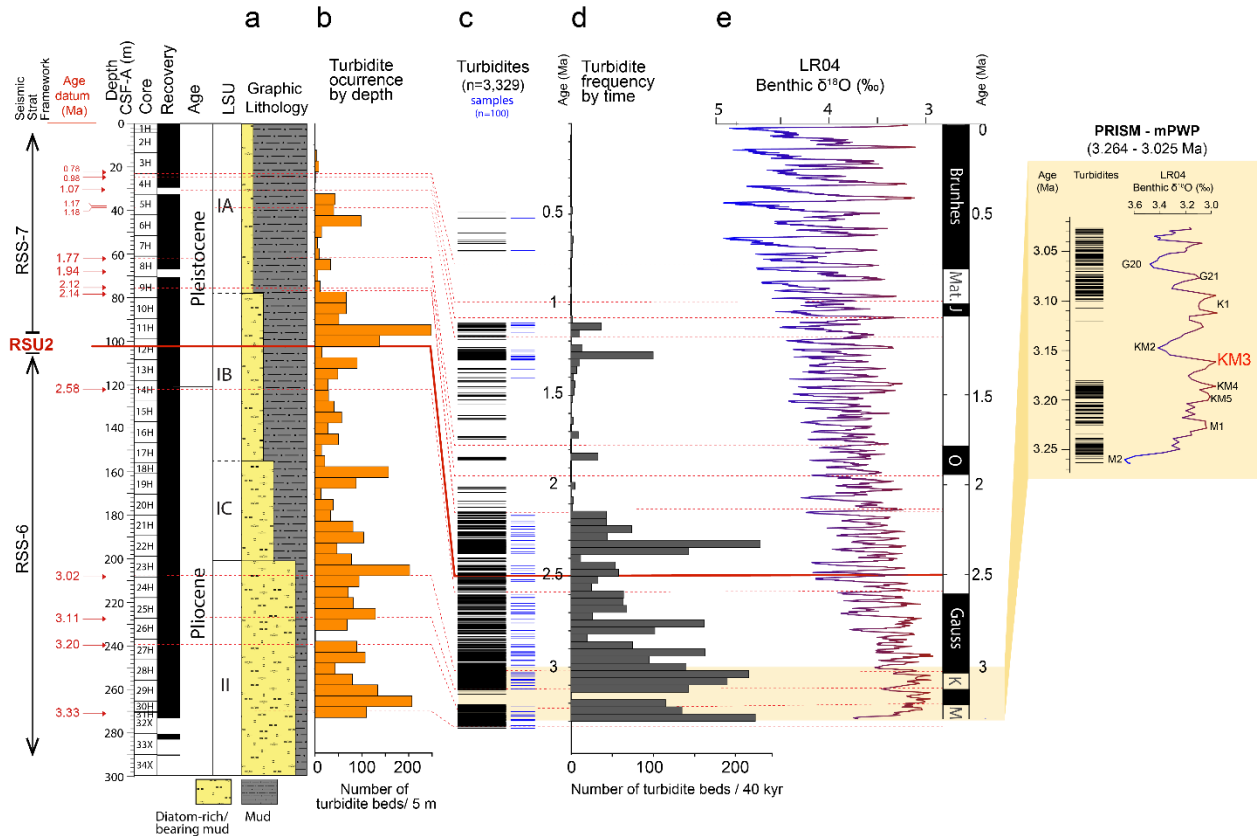


**Figure 4.** (a) Stratigraphic context for IODP Site U1524 (CSF-A in meters). Age datums (in red numbers) are denoted by the red dotted lines. Modified from McKay et al. (2019). (b) Frequency of the turbidite beds versus depth every 5 m. (c) Frequency of the turbidite beds versus time (black lines) and the location of the samples (blue lines). (d) Turbidite frequency plotted every 40 kyr. (e) Benthic  $\delta^{18}\text{O}$  LR04 stack (Lisiecki & Raymo, 2005) with the magnetostigraphic units for context. The yellow-shaded horizontal band shows the position of the PRISM-mPWP within the turbidite record, and the zoomed in box on the far right shows detail of the LR04 stack for that time.

## 5.2. Grain size

The grain size of the turbidite beds ranges from very fine silt to very fine sand (5->100  $\mu\text{m}$ ) (Fig. 3d). The median particle size (D50) ranges from very fine to medium silt (5-29  $\mu\text{m}$ ), whereas the D90 extends from medium silt to very fine sand (9->115  $\mu\text{m}$ ). There is no systematic trend in the grain size of the turbidite beds as a function of depth, and the median values indicate a coarser grain size when compared to the overlying mud (5-7  $\mu\text{m}$ ). The grain size analysis for overlying mud, expressed in silt (4-63  $\mu\text{m}$ ) percent, is a rather stable throughout the core, ranging from 13% to 44%. This trend, or lack thereof, is consistent with the turbidite beds. Regarding the relationship

between turbidite bed and corresponding overlying mud grain size, a weak correlation is observed (Fig. 3d-e).

### *5.3. Calculated density flow properties*

The 100,000 simulations were run with a relatively wide range of parameters (Table 2). To see what flow parameters are most likely, considering the information from Site U1524, we excluded all the realizations that do not satisfy the following criteria:

- coarse bed thickness at Site U1524 is between 0.1 – 0.3 cm (1 – 3 mm)
- fine bed thickness at Site U1524 is between 1 – 5 cm (10-50 mm)
- coarse grain size at Site U1524 is less than 80  $\mu\text{m}$  (0.08 mm)

After eliminating these realizations, there are 1,759 parameter combinations left (<2% of total number of simulations). A typical simulation result illustrates that bed thickness is the result of the interplay between concentration (C) and entrainment (E), for both grain size classes, although entrainment outside of the Hillary Canyon is zero, therefore does not play a role at Site U1524 (orange line in Fig. 6b-c). Therefore, outside the canyon, the bed thickness is close to constant, both for the coarser and finer grain size classes (Fig. 5). This is consistent with the seismic geometries observed within the overbank deposits of Hillary Canyon (Fig. 1).

This set of parameters provides a probabilistic view of the flow parameters (Fig. 6). The most important insight is that the density flows responsible for the deposits described here were likely low velocity (<0.6 m/s) currents with a very low concentration of the coarser grain fraction (<1%). The fact that coarser grain sizes are more likely to produce results that match the data at Site U1524 (Fig. 5) suggest that, if slightly coarser grains were available, they would be observed at this location. Thus, the lack of coarser grain sizes is likely a reflection of the unavailability of such grains. This also means that the thalweg of Hillary Canyon is unlikely to have thick, coarse-grained turbidite deposits that are characteristic of most submarine canyon-channel systems that are directly linked to a terrestrial source of coarse sediment. The broad, mode-free distributions of thickness, concentration, and grain size observed for the fine sediment class suggest that a broader set of parameters would match the data. This is a reflection of the fact that, due to the ease of suspending such fine grains, a wide range of concentrations and flow durations can result in the sediment characteristics observed at Site U1524.

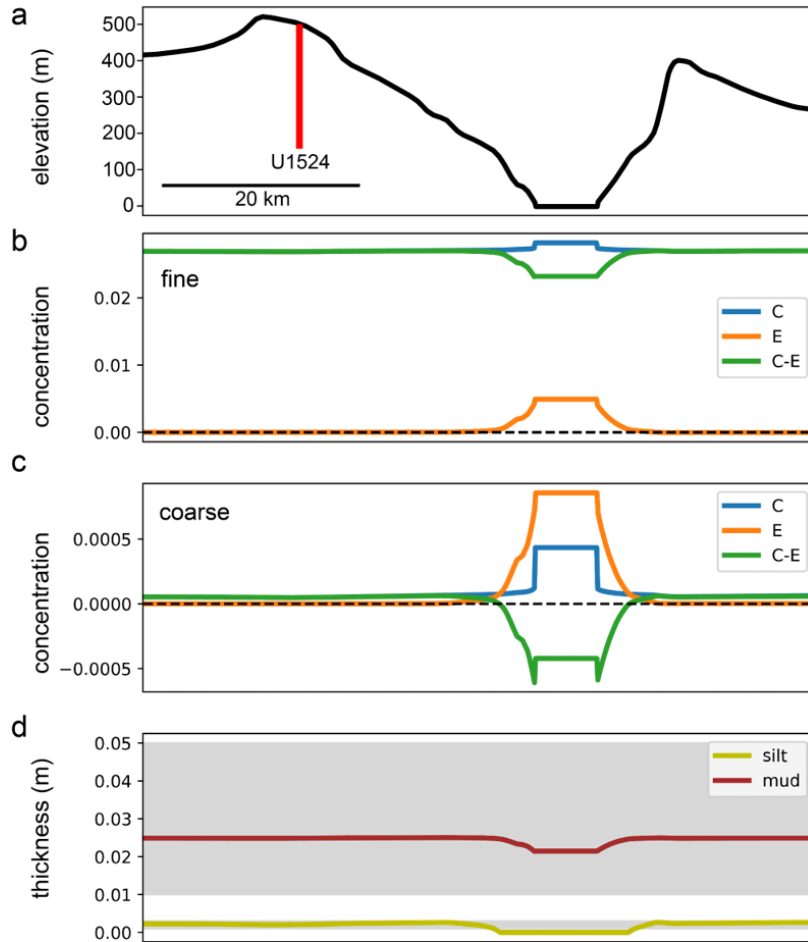


**Figure 5.** A typical simulation result that shows the bathymetric profile (a) used in the simulations, the variation of concentration (C) and entrainment (E) along the profile, for both the fine (b) and coarse (c) sediment classes, and the resulting deposit thicknesses (d). Gray intervals in the thickness plot correspond to the acceptable thickness ranges used when selecting the 1759 matching simulations from the larger set.

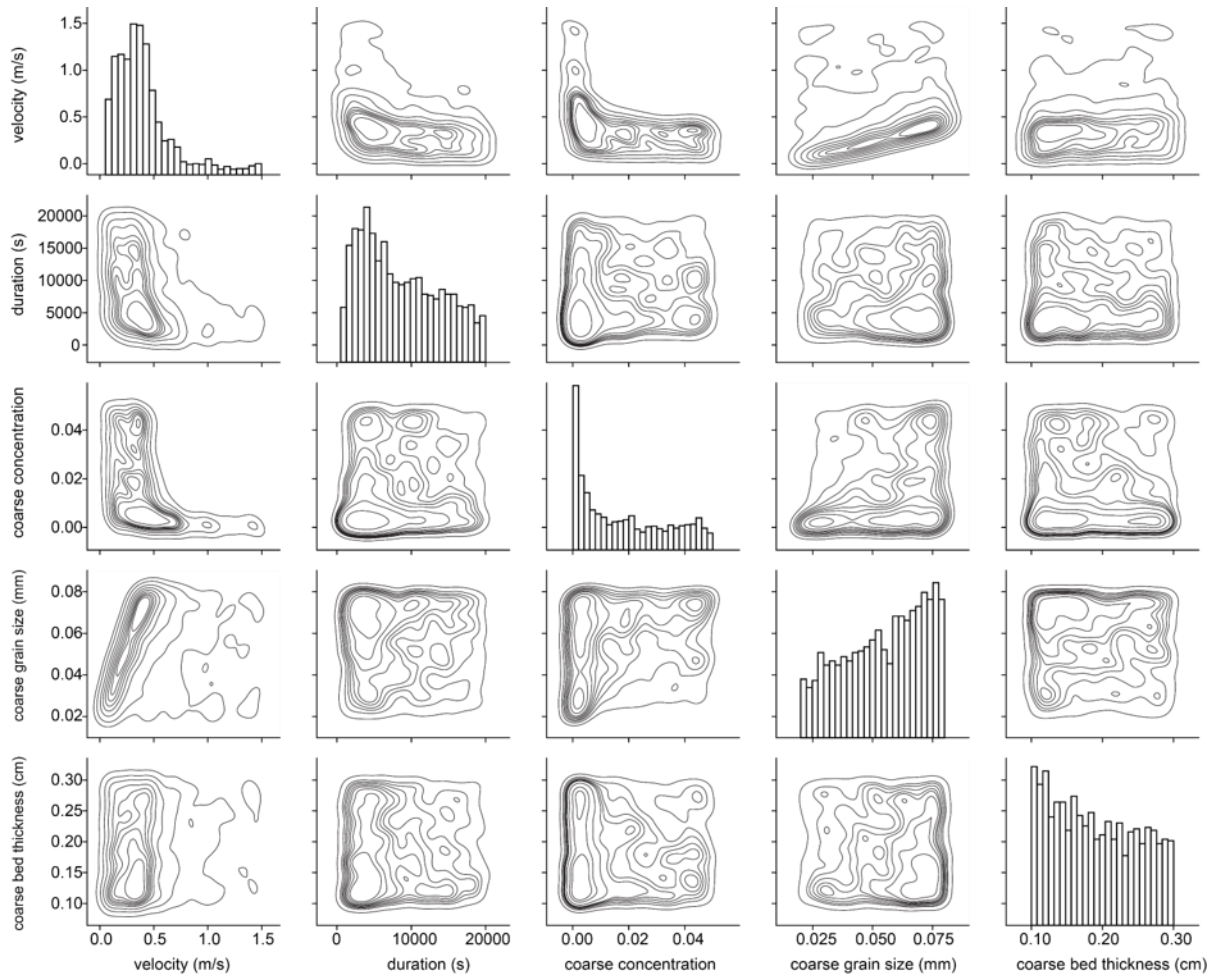


**Figure 6.** Pairwise plots and histograms of the main flow parameters for the 1759 simulations that match the observations at IODP Site U1524.

## 6. Discussion

Our results are consistent with a process that previous workers have proposed (Backhaus et al., 1997; Baines & Condie, 1998; Ivanov et al., 2004) whereby DSW cascading off the shelf edge is funneled into relatively narrow slope conduits (canyon-channel systems), resulting in enhanced AABW production to the deep ocean (e.g. Ohshima et al., 2013; Gales et al., 2021; Conte et al., 2021). We posit that focused density flows of sufficient velocity entrain and resuspend sediment from the outer shelf or upper slope, leading to the development of a low-concentration turbidity current. These sediment-laden density currents, in turn, contribute to the construction of levee deposits adjacent to the channel. Here, we investigate the relationship of our turbidite record from Site U1524 to climatic conditions and change over the past  $\sim 3.3$  Myr with an emphasis on linked

DSW-AABW outflow history. We also discuss the broader context and potential caveats to using submarine channel-levee deposits as a physical proxy of bottom water formation in high-latitude settings.

### *6.1. AABW production from the latest Pliocene (~3.3 Ma) to present*

Linked DSW-AABW formation in the modern Ross Sea is controlled by several factors, including available shelf area (Amblas & Dowdeswell, 2018), seasonal polynya and sea ice formation (Baines & Condie, 1998; Amblas & Dowdeswell, 2018), interaction with warmer water masses (e.g. CDW/LCDW; Amblas & Dowdeswell, 2018; Morrison et al., 2020), interactions with the Antarctic Slope Current (Conte et al., 2021), location of large cross-shelf troughs (Amblas & Dowdeswell, 2018; Gales et al., 2021), among others. We interpret the turbidite record during the Pliocene-Pleistocene as the result of linked DSW-AABW production and investigate the multi-millennial frequency changes in the context of those controlling factors.

The base of Hole U1524A and of our sedimentological record is ~3.3 Ma, thus capturing the late Pliocene (3.3 to 2.6 Ma), a time characterized by generally cooling temperatures (relative to early and mid-Pliocene), but with regular, orbitally-paced advance and retreat of the marine-based WAIS across the Ross Sea continental shelf (Naish et al., 2009; McKay et al., 2012; Austermann et al., 2015). Diatom assemblages, biomarker-based sea surface temperatures (SSTs), and bulk sediment carbon and nitrogen isotopes are interpreted to show that this overall cooling led to enhanced polynya-mixing and increase presence of summer sea ice in the Ross Sea (McKay et al., 2012).

Within the Pliocene (Fig. 7a), during the period between 3.264–3.025 Ma, known as the mid-Piacenzian/mid-Pliocene Warm Period (mPWP), there is a consensus on a reduced WAIS during interglacials, as compared to the modern (Raymo et al., 1996; Naish et al., 2009; H. J. Dowsett et al., 2013; Austermann et al., 2015). A range of AOGCMs models have predicted globally warmer ocean temperatures, an overall weaker thermohaline circulation, and a reduced outflow of AABW into the Pacific, among other effects (Haywood & Valdes, 2004; Dowsett et al., 2009; Haywood et al., 2016); however, these models are not coupled directly to ice sheets, and therefore the impact of active glacier melt on past water mass formation and overturning remains unvalidated.

In Site U1524, however, and except for a brief interval (~3.17-3.12 Ma) where there is no turbidite deposition (see section 6.2), the late Pliocene record has the highest frequency of turbidites (50->200 beds per 40 kyr) of the entire succession (Fig. 4d). We attribute this generally high DSW-AABW production to be the consequence of the enhanced polynya formation combined with an expansion of the WAIS that, although grounded at the mid-shelf (ANDRILL AND-1B), did not extend to the outermost continental shelf. This configuration promoted DSW production in the Ross Sea, even during most of the mPWP. Diminished frequency of the turbidite bed deposition (25-40 beds per 40 kyr) started at ~2.8 Ma (Fig. 4d), coincident with reduced Southern Ocean ventilation, which has been attributed to increased sea ice cover and stratification of surface waters (Hodell & Venz-Curtis, 2006; McKay et al., 2012; Patterson et al., 2018).

Full glacial conditions and the grounding of the WAIS at the continental shelf edge occurred at ~2.5 Ma as recorded by the regional erosional seismic unconformity RSU-2 (Brancolini et al., 1995; Conte et al., 2021). Coincident with this, there is a further increase in sea ice production and polynya formation on the continental shelf, along with reinvigoration of bottom current activity (McKay et al., 2019; Conte et al., 2021). At Site U1524, we interpret the intensification of turbidite frequency in the interval immediately above 102 m (RSU-2) (Fig. 4d) as the result of these conditions, and therefore, an enhancement of DSW-AABW production.

During the remainder of the Pleistocene, the increasingly colder climate maintained the formation of sea ice and polynyas (Hall et al., 2001), coupled with regular orbital-scale advances of the WAIS across the Ross Sea shelf during glacials (McKay et al., 2012). After ~1 Ma, the ice sheet located in the Ross Sea embayment would have cooled enough to be able to allow the Ross Ice Shelf to persist throughout most of the interglacial periods, while glacials saw advances of the WAIS to the shelf break (King et al., 2022). This prevented the proximal shelf area from being exposed to prolonged open marine conditions in all but the peak interglacials, while the inner to mid-shelf was occupied by grounded ice sheets and large ice shelves (McKay et al., 2009, 2012). Such a configuration (Fig. 7b) suggesting an overall reduction in continental shelf area. available for dense water formation. In the record of Site U1524, the frequency of turbidite beds markedly declined following the ~2.5 Ma unconformity (RSU-2) and ultimately diminished to near-absence around ~1 Ma. We interpret this pattern as a consequence of the shrinking continental shelf area, resulting in a reduction in the volume of local production of DSW, and therefore, for the Hillary

Canyon AABW output that forms via this process. We note that the very low frequency of silt turbidites in the <1.0 Ma time period does not necessarily indicate the cessation of AABW formation in the Ross Sea, but that the DSW-AABW outflow events of sufficient magnitude to generate overbank flow from turbidity currents in this conduit diminished significantly. Another potential explanation is that during full glacial periods the dense water is produced in open ocean-polynyas, and there would be no channelization of the flow, reducing the transport energy of the plume and its capacity to carry sediments (Amblas & Dowdeswell, 2018; Bollen et al., 2022).

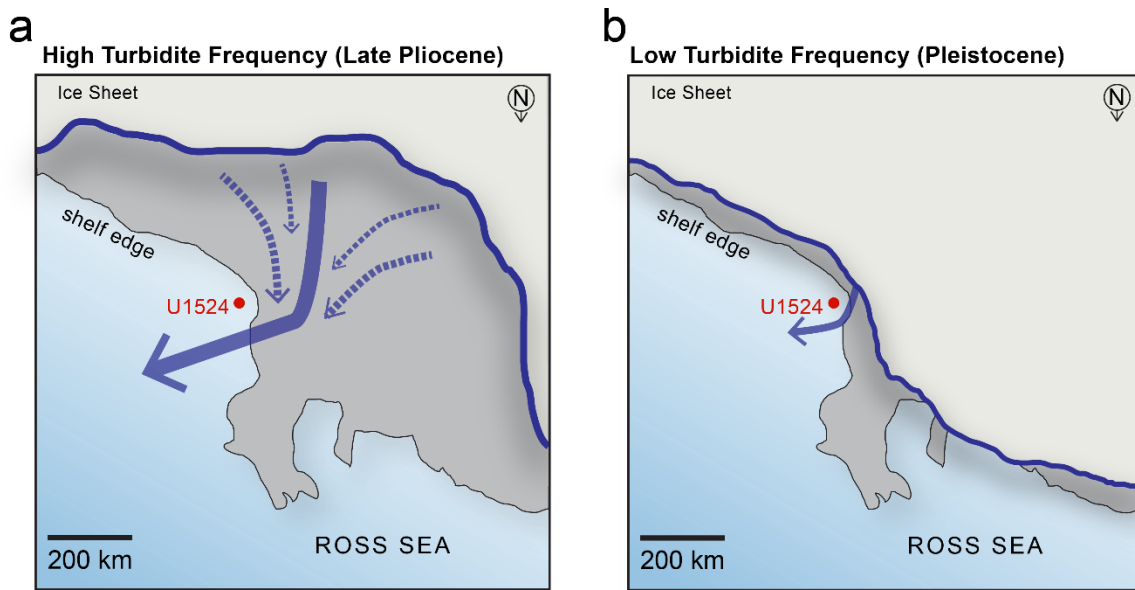


**Figure 7.** Schematic representation of the different scenarios to explain the variations in the frequency of the turbidite record in IODP Site U1524 (red dot); see Fig. 4. (a) High turbidite frequency. During the Late Pliocene, a generally cooling climate led to WAIS expansion and conditions for polynya/sea ice formation. These conditions combined with the relatively large shelf area promoted DSW formation. (b) Low turbidite frequency. The shelfward expansion of the WAIS during the increasingly colder conditions in the Pleistocene led to reduced shelf area and diminished DSW formation, even though the cooling climatic conditions could have sustained the polynya/sea ice formation during that time.

### 6.2. Shutdown of DSW-AABW outflow during anomalous late Pliocene interglacial KM3

In this Ross Sea-focused study, we observe a conspicuous gap in the occurrence of turbidite beds between 239.6-232.5 mbsf (~3.17-3.12 Ma) in Site U1524 (Figs. 4b and 4d; depth and age plots), in an otherwise dense record, which is followed by a return to the previous, higher frequency. We associate this gap to specific deglaciation threshold being reached in Ross Sea within the mPWP, that caused the cessation of DSW-driven AABW export through Hillary

Canyon. Marine Isotope Stage KM3 (3.17-3.15 Ma; Fig 4 - yellow box), as recorded in IODP Site U1361 from Wilkes Land (Patterson et al., 2014), has been interpreted as an anomalously warm interglacial based on diatom assemblages (Taylor-Silva & Riesselman, 2018). This short-lived (~20 kyr) event is associated with the southward migration of the Antarctic Polar Front (Barron, 1996; Taylor-Silva & Riesselman, 2018) and the reduction of sea ice formation (Dowsett et al., 1996; Haywood et al., 2016). The KM3 event was followed by a return to the overall cooling conditions of the late Pliocene, indicating again a greater influence of sea ice (Taylor-Silva & Riesselmann, 2018) and therefore brine rejection and polynya-driven linked DSW-AABW production.). We interpret that either sea ice, and polynya-driven DSW formation ceased, and with reduced presence of marine-based ice sheets during this anomalously warm interglacial resulting in a reduced ocean-ice interactions and water mass coolings. Consequently, although deglaciation provide a wide region for dense water formation, the reduced brine rejection and cooling driven by sea ice formation and marine-based resulted in a greatly reduced density of bottom waters being sourced from the Ross Sea, resulting in reduced intensity of turbidity current activity influencing deposition of silt turbidite laminae at Site U1524. This abrupt reduction of DSW-driven turbidity current activity suggests a highly sensitive, threshold influenced system during the mPWP, whereby partial deglaciation can enhance dense bottom water formation, before more expansive deglaciation of marine-based ice and reduction in sea ice formation can trigger a reduction.

### *6.3. Antarctic submarine channel-levee systems and dense-water formation*

Our novel application of thin-bedded, silty turbidites deposited in the levee of a major submarine conduit of DSW-AABW as a proxy for past dense-water production requires us to consider other factors that may influence the interpretation of similar deposits elsewhere. The following factors are analyzed in depth in this section.

#### *6.3.1. Record of high magnitude events only*

The low sediment concentration values estimated for the basal layer of these turbidity currents (<1% suspended sediment concentration; Figs. 5 and 6) supports an interpretation of cascading DSW as the main driver of the outflow in Hillary Canyon during the Pliocene-Pleistocene. In other words, unlike typical turbidity currents where the excess density necessary to initiate down-slope flow comes from suspended sediment (Talling et al., 2012), we consider the sediment in the Hillary

Canyon flows to be secondary. These results are in accordance with modern observational data in places like the Barrow Canyon in the Canada Basin, where the increase in density due to seasonal brine formation can trigger cascading flows (Shapiro, 2003). However, the construction of the turbidite record in the levees of Hillary Canyon suggests that not all DSW-AABW formation events would have scaled to the 40 km wide by ~500 m deep submarine canyon-channel system over the past ~3.3 Myr. Therefore, the record of AABW production in the Ross Sea, based on the silty, mm-thick turbidites in Site U1524, may be the product of the highest magnitude events; i.e., those with sufficient vigor to entrain and suspend sediment, and therefore, potentially biasing our record to only the major episodes of DSW-AABW outflow. Interestingly, our results show that the sedimentological character of these beds (thickness and grain size) do not appreciably change or show any obvious stratigraphic trend (Fig. 3), which suggests that the physical characteristics of these flows were relatively consistent and perhaps scaling to a maximum-magnitude outflow event.

### *6.3.2. Sediment availability*

Sediment availability is another potentially important factor to consider. There is a notable correspondence of the overall sediment accumulation rates and higher prevalence of diatom-rich sediment with the high turbidite frequency during the late Pliocene in Site U1524 (Fig. 4). This diatom-rich lithology diminishes gradually into and throughout the Pleistocene, as does the turbidite frequency, suggesting that the amount, and potentially type, of sediment available to be resuspended into these flows may influence interpretations of the record. However, the base of the gap in our turbidite record at 239.6-232.5 mbsf (~3.17-3.12 Ma), which coincides with the KM3 warming event discussed above, is interbedded between intervals with the highest frequency of DSW cascading events (Fig. 4) and, thus, likely sufficient sediment availability. With this in mind, we argue that the abrupt cessation of turbidite deposition due to an anomalously warm interglacial (e.g., significantly diminished polynya-driven DSW) is a more plausible explanation than a sudden lack of available sediment.

### *6.3.3. Potential effect of ASC*

Our study is focused on the linkage of DSW formation to AABW production in a single conduit (Hillary Canyon), but there are other important water masses and oceanographic currents in the Ross Sea that may have had an influence on the turbidite record at Site U1524. The relationship

between the Antarctic Slope Current (ASC) and the Antarctic Slope Front (ASF) with DSW outflow and CDW entrainment onto the continental shelf in the modern has been relatively well established (Baines, 2009; Jacobs, 1991; Thompson et al., 2018, 2020). For example, both ASC and ASF play a key role in controlling the heat exchange between the offshore, warmer CDW waters, and the shelf waters in the Ross Sea (e.g. Thomas et al., 2018, Conte et al. 2021, Gales et al. 2021). In Hillary Canyon, the relationship between the ASC and the DSW outflow interpreted by Conte et al. (2021), based on seismic-stratigraphic sequences, oceanographic data, and IODP sites including U1524, proposed a weakened ASC during the Pliocene, as evidenced by the deposition of RSS-6, followed by a strong ASC activity during the Pleistocene, recorded by RSS-7 (Fig. 1c), implying a similar behavior for the DSW-AABW formation. However, in our turbidite record, the highest frequency of outflow events is observed during the Pliocene, and, after an increase right after 2.5 Ma, the frequency noticeably decreases during the Pleistocene, to nearly no events after 1 Ma (Fig. 4). The apparent contradiction in this interpretation could be due to other factors that play a key role in DSW-AABW formation: (1) polynya-style mixing that started at around 3.3 Ma, registered by ANDRILL AND-1B core (McKay et al., 2012), and (2) a reduction in the shelf area due to the corresponding expansion of the WAIS (e.g. Jacobs, 1991, Naish et al. 2009; Amblas & Dowdeswell, 2018). Conte et al. (2021) also mentions that the deposition of RSS-6 (Fig. 4) could be the product of a decrease in bottom-current activity and a weakening of ASC, and therefore a reduction of AABW in the Ross Sea. As discussed above, the stable input of sediment during the Pliocene, based on the frequency, grain size, composition, and thickness of the turbidite record does not reflect that Conte et al. (2021) interpretation, but the complex interplay of oceanographic and physical processes involved in DSW-AABW production in the Ross Sea can account for more or one variable to explain these differences.

Our study focuses on one specific sedimentary deposit type on the continental rise of the Ross Sea that we interpret to record AABW production history. We acknowledge that our results do not capture the full range of processes and interactions that constructed the sedimentary record at IODP Site U1524. However, by isolating the specific process behind the largest DSW outflow events to the deep sea, which is an important process in other parts of Antarctica (Baines & Condie, 1998; Ivanov et al., 2004; Amblas & Dowdeswell, 2018), and potentially in the Arctic as well (e.g.

Midttun, 1985; Schauer, 1995; Ivanov et al., 2004; Årthun et al., 2011), our results establish a valuable physical proxy to better understand ice-ocean-sedimentary systems.

## 7. Conclusions

The formation of dense shelf water (DSW) in the modern Ross Sea is influenced by factors such as shelf area availability, seasonal polynya, sea ice dynamics, interactions with warmer water masses (mCDW) and along-slope currents, and the presence of cross-shelf troughs. The cascading process that brings DSW from the shelf area to the slope, eventually contributing to Antarctic Bottom Water (AABW) formation, triggers turbidity currents whose record of activity sits in the levees of submarine channels. The turbidite record of Site U1524 (IODP Expedition 374), drilled in the levee of the Hillary Canyon, a conduit for linked DSW-AABW formation, provides a physical record of this process during the Plio-Pleistocene in the Ross Sea.

The sedimentological characterization of 3,329 turbidite beds in Site U1524 includes identifying event frequency, thickness, and grain size analysis of 100 pairs of turbidites and their overlying mud. The grain size (D50 between 5-30  $\mu\text{m}$ ) and thickness of the beds (mean of 1.5 mm) reveals a lack of variability throughout the succession, which we interpret as the turbidite beds being deposited by a similar process. In addition, the grain size results and the Hillary Canyon dimensions conduit were used to model flow parameters, indicating that the density flows responsible for the deposits in Hillary Canyon were likely characterized by low velocities ( $<0.6$  m/s) and very low concentrations of the coarser grain fraction ( $<1\%$ ). This supports the interpretation that the main driver of the turbidity currents is water-mass density and therefore connecting this turbidite deposit to the DSW production.

The turbidite bed frequency of Site U1524, therefore, allows an analysis of the history of DSW-AABW over the past 3.3 Myr. The higher frequency of turbidites during the late Pliocene (3.3 to 2.6 Ma) is attributed to a cooling climate, an expanded WAIS, and enhanced polynya formation in the Ross Sea. However, at  $\sim 2.8$  Ma, our record shows decreased turbidite frequency, which we interpret to relate to documented reduced Southern Ocean ventilation due to an increased sea cover and stratification of ocean waters. Full glacial conditions at 2.5 Ma subsequently intensified sea ice production, polynya formation, and turbidite frequency. The colder climate of the Pleistocene supported the sustained formation of sea ice and polynyas. However, following the onset of the

larger West Antarctic Ice Sheet (WAIS) around 1 Ma, there was a reduction in continental shelf area, leading to a decline in the local production of DSW and AABW. This suggests that DSW export could also occur in open-ocean polynya environments, rather than being channeled through Hillary Canyon.

A distinct interruption in the turbidite bed occurrence is observed at 239.6-232.5 mbsf (~3.17-3.12 Ma), which coincides with an anomalous late Pliocene interglacial known as Marine Isotope Stage KM3. This hiatus in turbidite events is attributed to a specific deglaciation threshold being reached in the Ross Sea within the mid-Piacenzian Warm Period (mPWP), leading to the cessation of DSW-driven AABW export through Hillary Canyon. The KM3 event (3.17-3.15 Ma) is associated with the southward migration of the Antarctic Polar Front, reduction of sea ice formation, and overall warming conditions. The interruption in DSW-driven turbidity current activity during this period suggests a highly sensitive system, where partial deglaciation can enhance bottom water formation before more extensive deglaciation and reduced sea ice trigger a reduction in density and, consequently, a decrease in turbidity current activity.

Our study, centered on the turbidite deposits of IODP Site U1524, provides a crucial physical proxy for comprehending DSW-AABW production history in the Ross Sea. While acknowledging its limitations in fully capturing the diverse array of processes and interactions in the shelf-to-slope area, our research contributes new insights into past ice sheet-ocean interactions during climate fluctuations in the Pliocene-Pleistocene, that can aid in the projection and assessment of future climate scenarios.

## **8. References Cited**

- Altinakar, M. S., Graf, W. H., & Hopfinger, E. J. (1996). Flow structure in turbidity currents. *Journal of Hydraulic Research*, 34(5), 713–718. <https://doi.org/10.1080/00221689609498467>
- Amblas, D., & Dowdeswell, J. A. (2018). Physiographic influences on dense shelf-water cascading down the Antarctic continental slope. *Earth-Science Reviews*, 185, 887–900. <https://doi.org/10.1016/j.earscirev.2018.07.014>

- Årthun, M., Ingvaldsen, R. B., Smedsrud, L. H., & Schrum, C. (2011). Dense water formation and circulation in the Barents Sea. *Deep Sea Research Part I: Oceanographic Research Papers*, 58(8), 801–817. <https://doi.org/10.1016/j.dsr.2011.06.001>
- Austermann, J., Pollard, D., Mitrovica, J. X., Moucha, R., Forte, A. M., DeConto, R. M., Rowley, D. B., & Raymo, M. E. (2015). The impact of dynamic topography change on Antarctic ice sheet stability during the mid-Pliocene warm period. *Geology*, 43(10), 927–930. <https://doi.org/10.1130/G36988.1>
- Backhaus, J. O., Fohrmann, H., Kämpf, J., & Rubino, A. (1997). Formation and export of water masses produced in Arctic shelf polynyas—Process studies of oceanic convection. *ICES Journal of Marine Science*, 54(3), 366–382. <https://doi.org/10.1006/jmsc.1997.0230>
- Baines, P. G. (2009). A model for the structure of the Antarctic Slope Front. *Deep Sea Research Part II: Topical Studies in Oceanography*, 56(13–14), 859–873. <https://doi.org/10.1016/j.dsr2.2008.10.030>
- Baines, P. G., & Condie, S. (1998, March 18). *Observations and Modelling of Antarctic Downslope Flows: A Review*. AGU Journals; American Geophysical Union (AGU). <https://onlinelibrary.wiley.com/doi/abs/10.1029/AR075p0029>
- Barrett, P. J. (Ed.). (1989). Antarctic Cenozoic history from the CIROS-1 drillhole, McMurdo Sound. (*No Title*).
- Barron, J. A. (1996). Diatom constraints on the position of the Antarctic Polar Front in the middle part of the Pliocene. *Marine Micropaleontology*, 27(1), 195–213. [https://doi.org/10.1016/0377-8398\(95\)00060-7](https://doi.org/10.1016/0377-8398(95)00060-7)
- Basak, C., Pahnke, K., Frank, M., Lamy, F., & Gersonde, R. (2015). Neodymium isotopic characterization of Ross Sea Bottom Water and its advection through the southern South Pacific. *Earth and Planetary Science Letters*, 419, 211–221. <https://doi.org/10.1016/j.epsl.2015.03.011>

- Bergamasco, A., Defendi, V., Zambianchi, E., & Spezie, G. (2002). Evidence of dense water overflow on the Ross Sea shelf-break. *Antarctic Science*, *14*(3), 271–277. <https://doi.org/10.1017/S0954102002000068>
- Billups, K., Ravelo, A. C., & Zachos, J. C. (1997). Early Pliocene deep-water circulation: Stable isotope evidence for enhanced northern component deep water. *Proc. Ocean Drill. Program, Sci. Results*, *154*, 319–330.
- Blott, S. J., & Pye, K. (2001). GRADISTAT: A grain size distribution and statistics package for the analysis of unconsolidated sediments. *Earth Surface Processes and Landforms*, *26*(11), 1237–1248. <https://doi.org/10.1002/esp.261>
- Bollen, M., Riesselman, C. R., Ohneiser, C., Albot, O., McKay, R., Lee, M. K., Yoo, K.-C., Kim, S., Lee, J. I., & Levy, R. (2022). Pleistocene oceanographic variability in the Ross Sea: A multiproxy approach to age model development and paleoenvironmental analyses. *Global and Planetary Change*, *216*, 103901. <https://doi.org/10.1016/j.gloplacha.2022.103901>
- Brancolini, G., Cooper, A. K., & Coren, F. (1995). Seismic facies and glacial history in the western Ross Sea (Antarctica). *Geology and Seismic Stratigraphy of the Antarctic Margin*, *68*, 209–233.
- Budillon, G., Castagno, P., Aliani, S., Spezie, G., & Padman, L. (2011). Thermohaline variability and Antarctic bottom water formation at the Ross Sea shelf break. *Deep Sea Research Part I: Oceanographic Research Papers*, *58*(10), 1002–1018. <https://doi.org/10.1016/j.dsr.2011.07.002>
- Budillon, G., Gremes Cordero, S., & Salusti, E. (2002). On the dense water spreading off the Ross Sea shelf (Southern Ocean). *Journal of Marine Systems*, *35*(3–4), 207–227. [https://doi.org/10.1016/S0924-7963\(02\)00082-9](https://doi.org/10.1016/S0924-7963(02)00082-9)
- Chorley, H., Levy, R., Naish, T., Lewis, A., Cox, S., Hemming, S., Ohneiser, C., Gorman, A., Harper, M., Homes, A., Hopkins, J., Prebble, J., Verret, M., Dickinson, W., Florindo, F.,

- Golledge, N., Halberstadt, A. R., Kowalewski, D., McKay, R., ... Lurcock, P. (2022). East Antarctic Ice Sheet variability during the middle Miocene Climate Transition captured in drill cores from the Friis Hills, Transantarctic Mountains. *GSA Bulletin*, 135(5–6), 1503–1529. <https://doi.org/10.1130/B36531.1>
- Conte, R., Rebesco, M., De Santis, L., Colleoni, F., Bensi, M., Bergamasco, A., Kovacevic, V., Gales, J., Zgur, F., Accettella, D., De Steur, L., Ursella, L., McKay, R., Kim, S., & Lucchi, R. G. (2021). Bottom current control on sediment deposition between the Iselin Bank and the Hillary Canyon (Antarctica) since the late Miocene: An integrated seismic-oceanographic approach. *Deep Sea Research Part I: Oceanographic Research Papers*, 176, 103606. <https://doi.org/10.1016/j.dsr.2021.103606>
- Cook, C. P., van de Flierdt, T., Williams, T., Hemming, S. R., Iwai, M., Kobayashi, M., Jimenez-Espejo, F. J., Escutia, C., González, J. J., Khim, B.-K., McKay, R. M., Passchier, S., Bohaty, S. M., Riesselman, C. R., Tauxe, L., Sugisaki, S., Galindo, A. L., Patterson, M. O., Sangiorgi, F., ... Yamane, M. (2013). Dynamic behaviour of the East Antarctic ice sheet during Pliocene warmth. *Nature Geoscience*, 6(9), Article 9. <https://doi.org/10.1038/ngeo1889>
- de Leeuw, J., Eggenhuisen, J. T., & Cartigny, M. J. B. (2018). Linking submarine channel–levee facies and architecture to flow structure of turbidity currents: Insights from flume tank experiments. *Sedimentology*, 65(3), 931–951. <https://doi.org/10.1111/sed.12411>
- De Santis, L. (1999). The Eastern Ross Sea continental shelf during the Cenozoic: Implications for the West Antarctic ice sheet development. *Global and Planetary Change*, 23(1–4), 173–196. [https://doi.org/10.1016/S0921-8181\(99\)00056-9](https://doi.org/10.1016/S0921-8181(99)00056-9)
- Dowsett, H., Barron, J., & Poore, R. (1996). Middle Pliocene sea surface temperatures: A global reconstruction. *Marine Micropaleontology*, 27(1), 13–25. [https://doi.org/10.1016/0377-8398\(95\)00050-X](https://doi.org/10.1016/0377-8398(95)00050-X)

- Dowsett, H. J., Robinson, M. M., & Foley, K. M. (2009). Pliocene three-dimensional global ocean temperature reconstruction. *Climate of the Past*, 5(4), 769–783. <https://doi.org/10.5194/cp-5-769-2009>
- Dowsett, H. J., Robinson, M. M., Stoll, D. K., Foley, K. M., Johnson, A. L. A., Williams, M., & Riesselman, C. R. (2013). The PRISM (Pliocene palaeoclimate) reconstruction: Time for a paradigm shift. *Philosophical Transactions of the Royal Society A: Mathematical, Physical and Engineering Sciences*, 371(2001), 20120524. <https://doi.org/10.1098/rsta.2012.0524>
- Draut, A. E., Raymo, M. E., McManus, J. F., & Oppo, D. W. (2003). Climate stability during the Pliocene warm period. *Paleoceanography*, 18(4). <https://doi.org/10.1029/2003PA000889>
- Duncan, B., McKay, R., Levy, R., Naish, T., Prebble, J. G., Sangiorgi, F., Krishnan, S., Hoem, F., Clowes, C., Dunkley Jones, T., Gasson, E., Kraus, C., Kulhanek, D. K., Meyers, S. R., Moossen, H., Warren, C., Willmott, V., Ventura, G. T., & Bendle, J. (2022). Climatic and tectonic drivers of late Oligocene Antarctic ice volume. *Nature Geoscience*, 15(10), Article 10. <https://doi.org/10.1038/s41561-022-01025-x>
- Eggenhuisen, J. T., Tilston, M. C., de Leeuw, J., Pohl, F., & Cartigny, M. J. B. (2020). Turbulent diffusion modelling of sediment in turbidity currents: An experimental validation of the Rouse approach. *The Depositional Record*, 6(1), 203–216. <https://doi.org/10.1002/dep2.86>
- Ferguson, R. I., & Church, M. (2004). A Simple Universal Equation for Grain Settling Velocity. *Journal of Sedimentary Research*, 74(6), 933–937. <https://doi.org/10.1306/051204740933>
- Flower, B. P. (1999). Warming without high CO<sub>2</sub>? *Nature*, 399(6734), Article 6734. <https://doi.org/10.1038/20568>
- Flower, B. P., & Kennett, J. P. (1994). The middle Miocene climatic transition: East Antarctic ice sheet development, deep ocean circulation and global carbon cycling. *Palaeogeography, Palaeoclimatology, Palaeoecology*, 108(3), 537–555. [https://doi.org/10.1016/0031-0182\(94\)90251-8](https://doi.org/10.1016/0031-0182(94)90251-8)

- Flower, B. P., & Kennett, J. P. (1995). Middle Miocene deepwater paleoceanography in the southwest Pacific: Relations with East Antarctic Ice Sheet development. *Paleoceanography*, *10*(6), 1095–1112. <https://doi.org/10.1029/95PA02022>
- Foldvik, A., Gammelsrød, T., Østerhus, S., Fahrbach, E., Rohardt, G., Schröder, M., Nicholls, K. W., Padman, L., & Woodgate, R. A. (2004). Ice shelf water overflow and bottom water formation in the southern Weddell Sea. *Journal of Geophysical Research: Oceans*, *109*(C2). <https://doi.org/10.1029/2003JC002008>
- Gales, J., Rebesco, M., De Santis, L., Bergamasco, A., Colleoni, F., Kim, S., Accettella, D., Kovacevic, V., Liu, Y., Olivo, E., Colizza, E., Florindo-Lopez, C., Zgur, F., & McKay, R. (2021). Role of dense shelf water in the development of Antarctic submarine canyon morphology. *Geomorphology*, *372*, 107453. <https://doi.org/10.1016/j.geomorph.2020.107453>
- Garcia, M. H. (1990). *Depositing and Eroding Sediment-Driven Flows: Turbidity Currents* [Report]. St. Anthony Falls Hydraulic Laboratory. <http://conservancy.umn.edu/handle/11299/108513>
- Garcia, M., & Parker, G. (1991). Entrainment of Bed Sediment into Suspension. *Journal of Hydraulic Engineering*, *117*(4), 414–435. [https://doi.org/10.1061/\(ASCE\)0733-9429\(1991\)117:4\(414\)](https://doi.org/10.1061/(ASCE)0733-9429(1991)117:4(414))
- Gill, A. E. (1973). Circulation and bottom water production in the Weddell Sea. *Deep Sea Research and Oceanographic Abstracts*, *20*(2), 111–140. [https://doi.org/10.1016/0011-7471\(73\)90048-X](https://doi.org/10.1016/0011-7471(73)90048-X)
- Goldner, A., Herold, N., & Huber, M. (2014). Antarctic glaciation caused ocean circulation changes at the Eocene–Oligocene transition. *Nature*, *511*(7511), Article 7511. <https://doi.org/10.1038/nature13597>
- Gordon, A. L. (1991). *The Role of Thermohaline Circulation in Global Climate Change*. <https://doi.org/10.7916/D8M04G8H>

- Gordon, A. L. (2001). Bottom Water Formation. In *Encyclopedia of Ocean Sciences* (pp. 334–340). Elsevier. <https://doi.org/10.1006/rwos.2001.0006>
- Gordon, A. L., Huber, B. A., & Busecke, J. (2015). Bottom water export from the western Ross Sea, 2007 through 2010: ROSS SEA BOTTOM WATER EXPORT. *Geophysical Research Letters*, *42*(13), 5387–5394. <https://doi.org/10.1002/2015GL064457>
- Gordon, A. L., Orsi, A. H., Muench, R., Huber, B. A., Zambianchi, E., & Visbeck, M. (2009). Western Ross Sea continental slope gravity currents. *Deep Sea Research Part II: Topical Studies in Oceanography*, *56*(13–14), 796–817. <https://doi.org/10.1016/j.dsr2.2008.10.037>
- Gordon, A. L., Zambianchi, E., Orsi, A., Visbeck, M., Giulivi, C. F., Whitworth, T., & Spezie, G. (2004). Energetic plumes over the western Ross Sea continental slope: ROSS SEA PLUMES. *Geophysical Research Letters*, *31*(21), n/a-n/a. <https://doi.org/10.1029/2004GL020785>
- Grant, G. R., Naish, T. R., Dunbar, G. B., Stocchi, P., Kominz, M. A., Kamp, P. J. J., Tapia, C. A., McKay, R. M., Levy, R. H., & Patterson, M. O. (2019). The amplitude and origin of sea-level variability during the Pliocene epoch. *Nature*, *574*(7777), Article 7777. <https://doi.org/10.1038/s41586-019-1619-z>
- Hall, I. R., McCave, I. N., Shackleton, N. J., Weedon, G. P., & Harris, S. E. (2001). Intensified deep Pacific inflow and ventilation in Pleistocene glacial times. *Nature*, *412*(6849), Article 6849. <https://doi.org/10.1038/35090552>
- Hall, I. R., McCave, I. N., Zahn, R., Carter, L., Knutz, P. C., & Weedon, G. P. (2003). Paleocurrent reconstruction of the deep Pacific inflow during the middle Miocene: Reflections of East Antarctic Ice Sheet growth. *Paleoceanography*, *18*(2). <https://doi.org/10.1029/2002PA000817>
- Hambrey, M. J., Ehrmann, W., & Larsen, B. (1991). Cenozoic glacial record of the Prydz Bay continental shelf, East Antarctica. In: *Barron, J; Larsen, B, et al.(Eds.), Proc. ODP, Sci. Results, College Station, TX.(Ocean Drilling Program), 119, 77-132, 119, 77–132.*

- Haywood, A. M., Dowsett, H. J., Dolan, A. M., Rowley, D., Abe-Ouchi, A., Otto-Bliesner, B., Chandler, M. A., Hunter, S. J., Lunt, D. J., Pound, M., & Salzmann, U. (2016). The Pliocene Model Intercomparison Project (PlioMIP) Phase 2: Scientific objectives and experimental design. *Climate of the Past*, *12*(3), 663–675. <https://doi.org/10.5194/cp-12-663-2016>
- Haywood, A. M., & Valdes, P. J. (2004). Modelling Pliocene warmth: Contribution of atmosphere, oceans and cryosphere. *Earth and Planetary Science Letters*, *218*(3), 363–377. [https://doi.org/10.1016/S0012-821X\(03\)00685-X](https://doi.org/10.1016/S0012-821X(03)00685-X)
- Hodell, D. A., & Venz-Curtis, K. A. (2006). Late Neogene history of deepwater ventilation in the Southern Ocean. *Geochemistry, Geophysics, Geosystems*, *7*(9). <https://doi.org/10.1029/2005GC001211>
- Holbourn, A., Kuhnt, W., Kochhann, K. G. D., Andersen, N., & Sebastian Meier, K. J. (2015). Global perturbation of the carbon cycle at the onset of the Miocene Climatic Optimum. *Geology*, *43*(2), 123–126. <https://doi.org/10.1130/G36317.1>
- Huang, X., Stürz, M., Gohl, K., Knorr, G., & Lohmann, G. (2017). Impact of Weddell Sea shelf progradation on Antarctic bottom water formation during the Miocene. *Paleoceanography*, *32*(3), 304–317. <https://doi.org/10.1002/2016PA002987>
- Ivanov, V. V., Shapiro, G. I., Huthnance, J. M., Aleynik, D. L., & Golovin, P. N. (2004). Cascades of dense water around the world ocean. *Progress in Oceanography*, *60*(1), 47–98. <https://doi.org/10.1016/j.pocean.2003.12.002>
- Jacobs, S. S. (1991). On the nature and significance of the Antarctic Slope Front. *Marine Chemistry*, *35*(1), 9–24. [https://doi.org/10.1016/S0304-4203\(09\)90005-6](https://doi.org/10.1016/S0304-4203(09)90005-6)
- Jacobs, S. S., Amos, A. F., & Bruchhausen, P. M. (1970). Ross sea oceanography and antarctic bottom water formation. *Deep Sea Research and Oceanographic Abstracts*, *17*(6), 935–962. [https://doi.org/10.1016/0011-7471\(70\)90046-X](https://doi.org/10.1016/0011-7471(70)90046-X)

- King, M. V., Gales, J. A., Laberg, J. S., McKay, R. M., De Santis, L., Kulhanek, D. K., Hosegood, P. J., & Morris, A. (2022). Pleistocene depositional environments and links to cryosphere-ocean interactions on the eastern Ross Sea continental slope, Antarctica (IODP Hole U1525A). *Marine Geology*, *443*, 106674. <https://doi.org/10.1016/j.margeo.2021.106674>
- Kneller, B., & Buckee, C. (2000). The structure and fluid mechanics of turbidity currents: A review of some recent studies and their geological implications. *Sedimentology*, *47*(s1), 62–94. <https://doi.org/10.1046/j.1365-3091.2000.047s1062.x>
- Lear, C. H., Coxall, H. K., Foster, G. L., Lunt, D. J., Mawbey, E. M., Rosenthal, Y., Sosdian, S. M., Thomas, E., & Wilson, P. A. (2015). Neogene ice volume and ocean temperatures: Insights from infaunal foraminiferal Mg/Ca paleothermometry. *Paleoceanography*, *30*(11), 1437–1454. <https://doi.org/10.1002/2015PA002833>
- Lear, C. H., Elderfield, H., & Wilson, P. A. (2000). Cenozoic Deep-Sea Temperatures and Global Ice Volumes from Mg/Ca in Benthic Foraminiferal Calcite. *Science*, *287*(5451), 269–272. <https://doi.org/10.1126/science.287.5451.269>
- Leutert, T. J., Modestou, S., Bernasconi, S. M., & Meckler, A. N. (2021). Southern Ocean bottom-water cooling and ice sheet expansion during the middle Miocene climate transition. *Climate of the Past*, *17*(5), 2255–2271. <https://doi.org/10.5194/cp-17-2255-2021>
- Lewis, A. R., Marchant, D. R., Ashworth, A. C., Hemming, S. R., & Machlus, M. L. (2007). Major middle Miocene global climate change: Evidence from East Antarctica and the Transantarctic Mountains. *GSA Bulletin*, *119*(11–12), 1449–1461. [https://doi.org/10.1130/0016-7606\(2007\)119\[1449:MMMGCC\]2.0.CO;2](https://doi.org/10.1130/0016-7606(2007)119[1449:MMMGCC]2.0.CO;2)
- Li, Q., England, M. H., Hogg, A. M., Rintoul, S. R., & Morrison, A. K. (2023). Abyssal ocean overturning slowdown and warming driven by Antarctic meltwater. *Nature*, *615*(7954), Article 7954. <https://doi.org/10.1038/s41586-023-05762-w>

- Lisiecki, L. E., & Raymo, M. E. (2007). Plio–Pleistocene climate evolution: Trends and transitions in glacial cycle dynamics. *Quaternary Science Reviews*, 26(1), 56–69. <https://doi.org/10.1016/j.quascirev.2006.09.005>
- M. McKay, R., Escutia, C., De Santis, L., Donda, F., Duncan, B., Gohl, K., Gulick, S., Hernández-Molina, J., Hillenbrand, C.-D., Hochmuth, K., Kim, S., Kuhn, G., Larter, R., Leitchenkov, G., H. Levy, R., R. Naish, T., O’Brien, P., F. Pérez, L., E. Shevenell, A., & Williams, T. (2022). Chapter 3—Cenozoic history of Antarctic glaciation and climate from onshore and offshore studies. In F. Florindo, M. Siegert, L. D. Santis, & T. Naish (Eds.), *Antarctic Climate Evolution (Second Edition)* (pp. 41–164). Elsevier. <https://doi.org/10.1016/B978-0-12-819109-5.00008-6>
- Marschalek, J. W., Zurli, L., Talarico, F., van de Flierdt, T., Vermeesch, P., Carter, A., Beny, F., Bout-Roumazelles, V., Sangiorgi, F., Hemming, S. R., Pérez, L. F., Colleoni, F., Prebble, J. G., van Peer, T. E., Perotti, M., Shevenell, A. E., Browne, I., Kulhanek, D. K., Levy, R., ... McKay, R. M. (2021). A large West Antarctic Ice Sheet explains early Neogene sea-level amplitude. *Nature*, 600(7889), Article 7889. <https://doi.org/10.1038/s41586-021-04148-0>
- McCave, I. N., & Hall, I. R. (2006). Size sorting in marine muds: Processes, pitfalls, and prospects for paleoflow-speed proxies. *Geochemistry, Geophysics, Geosystems*, 7(10). <https://doi.org/10.1029/2006GC001284>
- McKay, M., & Beckman, R. (1979). WJ, A comparison of three methods for selecting values of input variables in the analysis of output from a computer CodeTechnometrics. *Am Stat Assoc Am Soc Qual*, 21, 239–245.
- McKay, R., Browne, G., Carter, L., Cowan, E., Dunbar, G., Krissek, L., Naish, T., Powell, R., Reed, J., Talarico, F., & Wilch, T. (2009). The stratigraphic signature of the late Cenozoic Antarctic Ice Sheets in the Ross Embayment. *GSA Bulletin*, 121(11–12), 1537–1561. <https://doi.org/10.1130/B26540.1>

- McKay, R., De Santis, L., Kulhanek, D. K., & Expedition 374 Scientists (Eds.). (2019). *Ross Sea West Antarctic Ice Sheet History* (Vol. 374). International Ocean Discovery Program. <https://doi.org/10.14379/iodp.proc.374.2019>
- McKay, R. M., De Santis, L., Kulhanek, D. K., Ash, J., Beny, F., Browne, I. M., Cortese, G., Dodd, J. P., Esper, O. M., Gales, J. A., Harwood, D. M., Ishino, S., Keisling, B. A., Kim, S., Kim, S., Kulhanek, D. K., Laberg, J. S., Leckie, M., Mueller, J., ... Xiong, Z. (2018). *[No title found]*. International Ocean Discovery Program. <https://doi.org/10.14379/iodp.pr.374.2018>
- McKay, R., Naish, T., Carter, L., Riesselman, C., Dunbar, R., Sjunneskog, C., Winter, D., Sangiorgi, F., Warren, C., Pagani, M., Schouten, S., Willmott, V., Levy, R., DeConto, R., & Powell, R. D. (2012). Antarctic and Southern Ocean influences on Late Pliocene global cooling. *Proceedings of the National Academy of Sciences*, *109*(17), 6423–6428. <https://doi.org/10.1073/pnas.1112248109>
- Midttun, L. (1985). Formation of dense bottom water in the Barents Sea. *Deep Sea Research Part A. Oceanographic Research Papers*, *32*(10), 1233–1241. [https://doi.org/10.1016/0198-0149\(85\)90006-8](https://doi.org/10.1016/0198-0149(85)90006-8)
- Miller, K. G., Wright, J. D., Browning, J. V., Kulpecz, A., Kominz, M., Naish, T. R., Cramer, B. S., Rosenthal, Y., Peltier, W. R., & Sosdian, S. (2012). High tide of the warm Pliocene: Implications of global sea level for Antarctic deglaciation. *Geology*, *40*(5), 407–410. <https://doi.org/10.1130/G32869.1>
- Morrison, A. K., Hogg, A. McC., England, M. H., & Spence, P. (2020). Warm Circumpolar Deep Water transport toward Antarctica driven by local dense water export in canyons. *Science Advances*, *6*(18), eaav2516. <https://doi.org/10.1126/sciadv.aav2516>
- Naish, T., Powell, R., Levy, R., Wilson, G., Scherer, R., Talarico, F., Krissek, L., Niessen, F., Pompilio, M., Wilson, T., Carter, L., DeConto, R., Huybers, P., McKay, R., Pollard, D., Ross, J., Winter, D., Barrett, P., Browne, G., ... Williams, T. (2009). Obliquity-paced Pliocene West

- Antarctic ice sheet oscillations. *Nature*, 458(7236), 322–328.  
<https://doi.org/10.1038/nature07867>
- Ohshima, K. I., Fukamachi, Y., Williams, G. D., Nihashi, S., Roquet, F., Kitade, Y., Tamura, T., Hirano, D., Herraiz-Borreguero, L., Field, I., Hindell, M., Aoki, S., & Wakatsuchi, M. (2013). Antarctic Bottom Water production by intense sea-ice formation in the Cape Darnley polynya. *Nature Geoscience*, 6(3), 235–240. <https://doi.org/10.1038/ngeo1738>
- Orsi, A. H. (2002). On the total input of Antarctic waters to the deep ocean: A preliminary estimate from chlorofluorocarbon measurements. *Journal of Geophysical Research*, 107(C8), 3122. <https://doi.org/10.1029/2001JC000976>
- Orsi, A. H., Johnson, G. C., & Bullister, J. L. (1999). Circulation, mixing, and production of Antarctic Bottom Water. *Progress in Oceanography*, 43(1), 55–109. [https://doi.org/10.1016/S0079-6611\(99\)00004-X](https://doi.org/10.1016/S0079-6611(99)00004-X)
- Orsi, A. H., & Wiederwohl, C. L. (2009). A recount of Ross Sea waters. *Deep Sea Research Part II: Topical Studies in Oceanography*, 56(13–14), 778–795. <https://doi.org/10.1016/j.dsr2.2008.10.033>
- Pagani, M., Liu, Z., LaRiviere, J., & Ravelo, A. C. (2010). High Earth-system climate sensitivity determined from Pliocene carbon dioxide concentrations. *Nature Geoscience*, 3(1), Article 1. <https://doi.org/10.1038/ngeo724>
- Patterson, M. O., McKay, R., Naish, T., Bostock, H. C., Dunbar, R., Ohneiser, C., Woodard, S. C., Wilson, G., & Caballero-Gill, R. (2018). A Southwest Pacific Perspective on Long-Term Global Trends in Pliocene-Pleistocene Stable Isotope Records. *Paleoceanography and Paleoclimatology*, 33(7), 825–839. <https://doi.org/10.1029/2017PA003269>
- Patterson, M. O., McKay, R., Naish, T., Escutia, C., Jimenez-Espejo, F. J., Raymo, M. E., Meyers, S. R., Tauxe, L., & Brinkhuis, H. (2014). Orbital forcing of the East Antarctic ice sheet during

- the Pliocene and Early Pleistocene. *Nature Geoscience*, 7(11), Article 11. <https://doi.org/10.1038/ngeo2273>
- Piper, D. J. W., & Normark, W. R. (1983). Turbidite depositional patterns and flow characteristics, Navy Submarine Fan, California Borderland. *Sedimentology*, 30(5), 681–694. <https://doi.org/10.1111/j.1365-3091.1983.tb00702.x>
- Prescott, C. L., Haywood, A. M., Dolan, A. M., Hunter, S. J., Pope, J. O., & Pickering, S. J. (2014). Assessing orbitally-forced interglacial climate variability during the mid-Pliocene Warm Period. *Earth and Planetary Science Letters*, 400, 261–271. <https://doi.org/10.1016/j.epsl.2014.05.030>
- Raymo, M. E., Grant, B., Horowitz, M., & Rau, G. H. (1996). Mid-Pliocene warmth: Stronger greenhouse and stronger conveyor. *Marine Micropaleontology*, 27(1), 313–326. [https://doi.org/10.1016/0377-8398\(95\)00048-8](https://doi.org/10.1016/0377-8398(95)00048-8)
- Rintoul, S. R. (2018). The global influence of localized dynamics in the Southern Ocean. *Nature*, 558(7709), 209–218. <https://doi.org/10.1038/s41586-018-0182-3>
- Rouse, H. & others. (1938). *Fluid mechanics for hydraulic engineers* (Vol. 1). McGraw-Hill New York.
- Sangiorgi, F., Bijl, P. K., Passchier, S., Salzmann, U., Schouten, S., McKay, R., Cody, R. D., Pross, J., van de Flierdt, T., Bohaty, S. M., Levy, R., Williams, T., Escutia, C., & Brinkhuis, H. (2018). Southern Ocean warming and Wilkes Land ice sheet retreat during the mid-Miocene. *Nature Communications*, 9(1), Article 1. <https://doi.org/10.1038/s41467-017-02609-7>
- Schauer, U. (1995). The release of brine-enriched shelf water from Storfjord into the Norwegian Sea. *Journal of Geophysical Research*, 100(C8), 16015. <https://doi.org/10.1029/95JC01184>
- Sequeiros, O. E., Spinewine, B., Beaubouef, R. T., Sun, T., García, M. H., & Parker, G. (2010). Characteristics of Velocity and Excess Density Profiles of Saline Underflows and Turbidity

Currents Flowing over a Mobile Bed. *Journal of Hydraulic Engineering*, 136(7), 412–433.  
[https://doi.org/10.1061/\(ASCE\)HY.1943-7900.0000200](https://doi.org/10.1061/(ASCE)HY.1943-7900.0000200)

Shadwick, E. H., Tilbrook, B., & Williams, G. D. (2014). Carbonate chemistry in the Mertz Polynya (East Antarctica): Biological and physical modification of dense water outflows and the export of anthropogenic CO<sub>2</sub>. *Journal of Geophysical Research: Oceans*, 119(1), 1–14.  
<https://doi.org/10.1002/2013JC009286>

Shapiro, G. I. (2003). Dense water cascading off the continental shelf. *Journal of Geophysical Research*, 108(C12), 3390. <https://doi.org/10.1029/2002JC001610>

Shevenell, A. E., Kennett, J. P., & Lea, D. W. (2004). Middle Miocene Southern Ocean Cooling and Antarctic Cryosphere Expansion. *Science*, 305(5691), 1766–1770.  
<https://doi.org/10.1126/science.1100061>

Shevenell, A. E., Kennett, J. P., & Lea, D. W. (2008). Middle Miocene ice sheet dynamics, deep-sea temperatures, and carbon cycling: A Southern Ocean perspective. *Geochemistry, Geophysics, Geosystems*, 9(2). <https://doi.org/10.1029/2007GC001736>

Silvano, A., Foppert, A., Rintoul, S. R., Holland, P. R., Tamura, T., Kimura, N., Castagno, P., Falco, P., Budillon, G., Haumann, F. A., Naveira Garabato, A. C., & Macdonald, A. M. (2020). Recent recovery of Antarctic Bottom Water formation in the Ross Sea driven by climate anomalies. *Nature Geoscience*, 13(12), 780–786. <https://doi.org/10.1038/s41561-020-00655-3>

Silvano, A., Rintoul, S. R., Peña-Molino, B., Hobbs, W. R., van Wijk, E., Aoki, S., Tamura, T., & Williams, G. D. (2018). Freshening by glacial meltwater enhances melting of ice shelves and reduces formation of Antarctic Bottom Water. *Science Advances*, 4(4), eaap9467.  
<https://doi.org/10.1126/sciadv.aap9467>

- Straub, K. M., & Mohrig, D. (2008). Quantifying the morphology and growth of levees in aggrading submarine channels. *Journal of Geophysical Research: Earth Surface*, 113(F3). <https://doi.org/10.1029/2007JF000896>
- Sugden, D., & Denton, G. (2004). Cenozoic landscape evolution of the Convoy Range to Mackay Glacier area, Transantarctic Mountains: Onshore to offshore synthesis. *GSA Bulletin*, 116(7–8), 840–857. <https://doi.org/10.1130/B25356.1>
- Talling, P. J., Masson, D. G., Sumner, E. J., & Malgesini, G. (2012). Subaqueous sediment density flows: Depositional processes and deposit types. *Sedimentology*, 59(7), 1937–2003. <https://doi.org/10.1111/j.1365-3091.2012.01353.x>
- Taylor-Silva, B. I., & Riesselman, C. R. (2018). Polar Frontal Migration in the Warm Late Pliocene: Diatom Evidence From the Wilkes Land Margin, East Antarctica. *Paleoceanography and Paleoclimatology*, 33(1), 76–92. <https://doi.org/10.1002/2017PA003225>
- Thompson, A. F., Speer, K. G., & Schulze Chretien, L. M. (2020). Genesis of the Antarctic Slope Current in West Antarctica. *Geophysical Research Letters*, 47(16), e2020GL087802. <https://doi.org/10.1029/2020GL087802>
- Thompson, A. F., Stewart, A. L., Spence, P., & Heywood, K. J. (2018). The Antarctic Slope Current in a Changing Climate. *Reviews of Geophysics*, 56(4), 741–770. <https://doi.org/10.1029/2018RG000624>
- Whitworth III, T., Orsi, A. H., Kim, S.-J., Nowlin Jr., W. D., & Locarnini, R. A. (1998). Water Masses and Mixing Near the Antarctic Slope Front. In *Ocean, Ice, and Atmosphere: Interactions at the Antarctic Continental Margin* (pp. 1–27). American Geophysical Union (AGU). <https://doi.org/10.1029/AR075p0001>
- Williams, G. D., Aoki, S., Jacobs, S. S., Rintoul, S. R., Tamura, T., & Bindoff, N. L. (2010). Antarctic Bottom Water from the Adélie and George V Land coast, East Antarctica (140–

149°E). *Journal of Geophysical Research: Oceans*, 115(C4).  
<https://doi.org/10.1029/2009JC005812>

Woodard, S. C., Rosenthal, Y., Miller, K. G., Wright, J. D., Chiu, B. K., & Lawrence, K. T. (2014). Antarctic role in Northern Hemisphere glaciation. *Science*, 346(6211), 847–851.  
<https://doi.org/10.1126/science.1255586>

Yabuki, T., Suga, T., Hanawa, K., Matsuoka, K., Kiwada, H., & Watanabe, T. (2006). Possible source of the antarctic bottom water in the Prydz Bay Region. *Journal of Oceanography*, 62(5), 649–655. <https://doi.org/10.1007/s10872-006-0083-1>

Zachos, J. C., Breza, J. R., & Wise, S. W. (1992). Early Oligocene ice-sheet expansion on Antarctica: Stable isotope and sedimentological evidence from Kerguelen Plateau, southern Indian Ocean. *Geology*, 20(6), 569–573. [https://doi.org/10.1130/0091-7613\(1992\)020<0569:EOISEO>2.3.CO;2](https://doi.org/10.1130/0091-7613(1992)020<0569:EOISEO>2.3.CO;2)

## **CHAPTER 2: Proximal-distal patterns in density-flow deposits on the Ross Sea continental slope and rise: Sedimentological characterization of Pleistocene deposits from IODP Sites U1524 and U1525**

Natalia Varela<sup>1</sup>, Brian W. Romans<sup>1</sup>

1. Department of Geosciences, Virginia Tech

### **Abstract**

Hillary Canyon, located in the Ross Sea, is an archive for ice sheet-ocean interactions since at least the Late Oligocene. The 40 km wide and 500 m deep submarine canyon-channel system cuts through the continental slope in an SSW-NNE direction, serving as a conduit for glacial sediments that are transported from the shelf to the continental rise. One of the main oceanographic processes happening at this location is the downslope flow of dense shelf water (DSW), that forms during the winter in the continental shelf of the Ross Sea due to an interplay between katabatic winds, polynya, sea ice formation, and the interaction with other water masses. The DSW, denser and colder than the surrounding water, sinks, forming a turbiditic flow that is channeled through the Hillary Canyon. DSW reaches depths over hundreds of meters, and contributes to the formation of Antarctic Bottom Water (AABW), the coldest, deepest, and densest water mass in the ocean, and a key player in the global ocean circulation. In this study, we propose that the physical record of the DSW-AABW formation is archived in the levees of the Hillary Canyon as turbidite deposits. Therefore, by characterizing the sedimentological features of those turbidites, we can identify the influence of other oceanographic processes acting at the time of the deposition, such as bottom currents, that can potentially be influencing DSW-AABW formation in the Ross Sea and/or the physical record of its activity.

IODP Expedition 374, drilled two sites on the levees of the Hillary Canyon, on the continental slope (Site U1525) and the rise (Site U1524), separated by ~87 km. The ~158 m of Pleistocene sediments recovered at the more proximal Site U1525 shows massive to stratified diamict, sand, mud, and layers with variable diatom content, which combined with the presence of ice-rafted debris reveal the influence of glaciomarine processes. The more distal Site U1524 is a ~270 m thick Plio-Pleistocene succession that represents a combination of hemipelagic and turbiditic mud, coarse silt to very fine sand beds, and diatom-bearing mud layers. Our sedimentological analyses

on the turbidite beds for the shared 2.1-0.7 Ma interval showed a similar average thickness (~1.5 mm) at both sites. Bed counting for U1525 (from 55.7 m to 116.5 mbsf) revealed 1,350 turbidite beds and ~260 for the same age interval in Site U1524. Our grain-size analysis targeted a subset of these silty to very fine-grained sand beds and the mud-dominated intervals that overlie them. The D50 (median) of these beds showed a coarser grain size range for Site U1525, the closest to the shelf edge. The frequency of the turbidite bed was generally similar for both sites until ~1 Ma, when the turbidite record stops at both sites, to then resume with a similar turbidite bed frequency after 900 ka, but only for U1525; after that ~1 Myr mark, the turbidite record in U1524 is almost non-existent.

We propose two possible explanations, both associated with the cooling experienced in the Pleistocene and the expansion of the ice sheets. One is the strengthening of the Antarctic Slope current (ASC) during the Pleistocene, which could have redistributed the sediment along the slope area, preventing it from being deposited further down-system on the rise. A second hypothesis is that during glacial times, the full expansion of the ice sheet could have pushed the formation of DSW-AABW further offshore, through open ocean polynyas, and therefore, leaving no record in the levees of the Hillary Canyon.

## **9. Introduction**

Antarctic Bottom Water (AABW) is a crucial component of the global thermohaline circulation, being the coldest ( $< 1^{\circ}\text{C}$ ), densest ( $> 28.27 \text{ km}^3/\text{m}^3$  neutral density), and deepest ( $> 1900 \text{ m}$ ) water mass in the ocean (Jacobs et al., 1970; Gordon, 1991; Orsi et al., 1999; Orsi, 2002; Amblas & Dowdeswell, 2018). The formation of modern Antarctic Bottom Water (AABW) is a result of the contact between the ice sheet and the ocean throughout the winter season (Baines & Condie, 1998; Orsi et al., 1999). These processes occur in a few locations along Antarctica's continental margins: the Weddell and Ross seas and along the Adelie coast (Baines & Condie, 1998; Orsi et al., 1999; Rintoul, 2018), and in the Prydz Bay area (Yabuki et al., 2006).

Previous studies, (i.e., Huan et al., (2017), have examined the history of AABW formation in response to climatic changes in the middle to late Miocene, and other authors have extrapolated the ice sheet retreats and advances. However, our understanding of AABW formation in the Southern Ocean during the Pleistocene is still limited, due to the ice sheet advances and retreats

that have eroded during the late Pliocene and early Pleistocene cooling. Additionally, investigating the outflow of AABW during warm periods of the last 2.1 million years has been crucial for understanding current warming trends and potential future scenarios.

In the present-day Ross Sea, sea ice formation along the coast is influenced by the strong katabatic winds originating from the West Antarctic Ice Sheet (WAIS), leading to the creation of coastal polynyas, defined as ice-free zones contiguous to the coastline (Jacobs et al., 1970; Baines & Condie, 1998). This phenomenon fosters a continuous ice formation, thereby heightening the salinity of the neighboring seawater. As a result, the seawater densifies and experiences an increase in oxygen levels, which can reach up to 8 ml/l, due the temperature reduction (Gordon, 2001).

The increased density levels in the shelf waters cause them to sink, ultimately leading to their export across the continental shelf. Under certain circumstances, they transfer over the continental slope, forming a plume-like shape that is influenced by topographical characteristics such as undersea canyons (Baines & Condie, 1998; Gales et al., 2021). These descending currents can sometimes carry and redistribute sediment from the outer shelf and upper continental slope. The presence of extra sediment increases the density of the descending plume, leading to the formation of a sediment-laden turbidity current (Jacobs et al., 1970; Baines & Condie, 1998).

To establish a correlation between these sedimentary deposits and the processes involving dense water, it is essential to analyze the conditions under which these deposits were formed. The presence of these gravity-driven events contributes to the formation of depositional levees next to a channel through a process known as "flow stripping" (Piper & Normark, 1983). This occurs when the upper portion of a turbidity current spills over the confined area, resulting in the accumulation of sediment on the adjacent overbank region (Straub & Mohrig, 2008). The resultant turbiditic deposits, therefore, serve as a potential archive of the interconnected oceanographic and sedimentary processes at play (Baines & Condie, 1998).

The International Ocean Discovery Program (IODP) Sites U1525 and U1524 (Fig. 1a), are two of the five sites drilled by Expedition 374 in 2018. Site U1525 is located more than 60 km away from the continental shelf edge of the Ross Sea, while U1524 is 87 km northeast of U1525, in the upper continental slope and the continental rise respectively. Their respective locations allows an evaluation of the interplay between oceanic influences and the West Antarctic Ice Sheet (WAIS)

during the Pleistocene, from the shelf edge to the slope. In addition to their proximal-to-distal location to the West Antarctic Ice Sheet (WAIS), these sites sit on the southeastern/eastern levee of the Hillary Canyon, a contemporary conduit for Ross Sea Bottom Water (RSBW), a type of AABW in the Ross Sea (McKay et al., 2019).

In this study, we propose that dense shelf water cascading in Hillary Canyon was the main trigger for the initiation of turbidity currents and that thin (<1 cm) turbidite beds within the mud-dominated succession at IODP Sites U1525 and U1524 record the history of AABW formation in the Ross Sea during the Pleistocene, along with the effect of the ice sheet-ocean feedbacks on the record. Our analysis focuses on the sedimentological characterization including grain size, thickness, and frequency of the interpreted turbidite beds in two sites, proximal to distal to the shelf edge, and therefore to the ice sheet. We interpret our results in the context of the last ~ 2.1 Myr ice sheet activity and the influence of the ocean currents in the Ross Sea during a time of progressive global cooling.

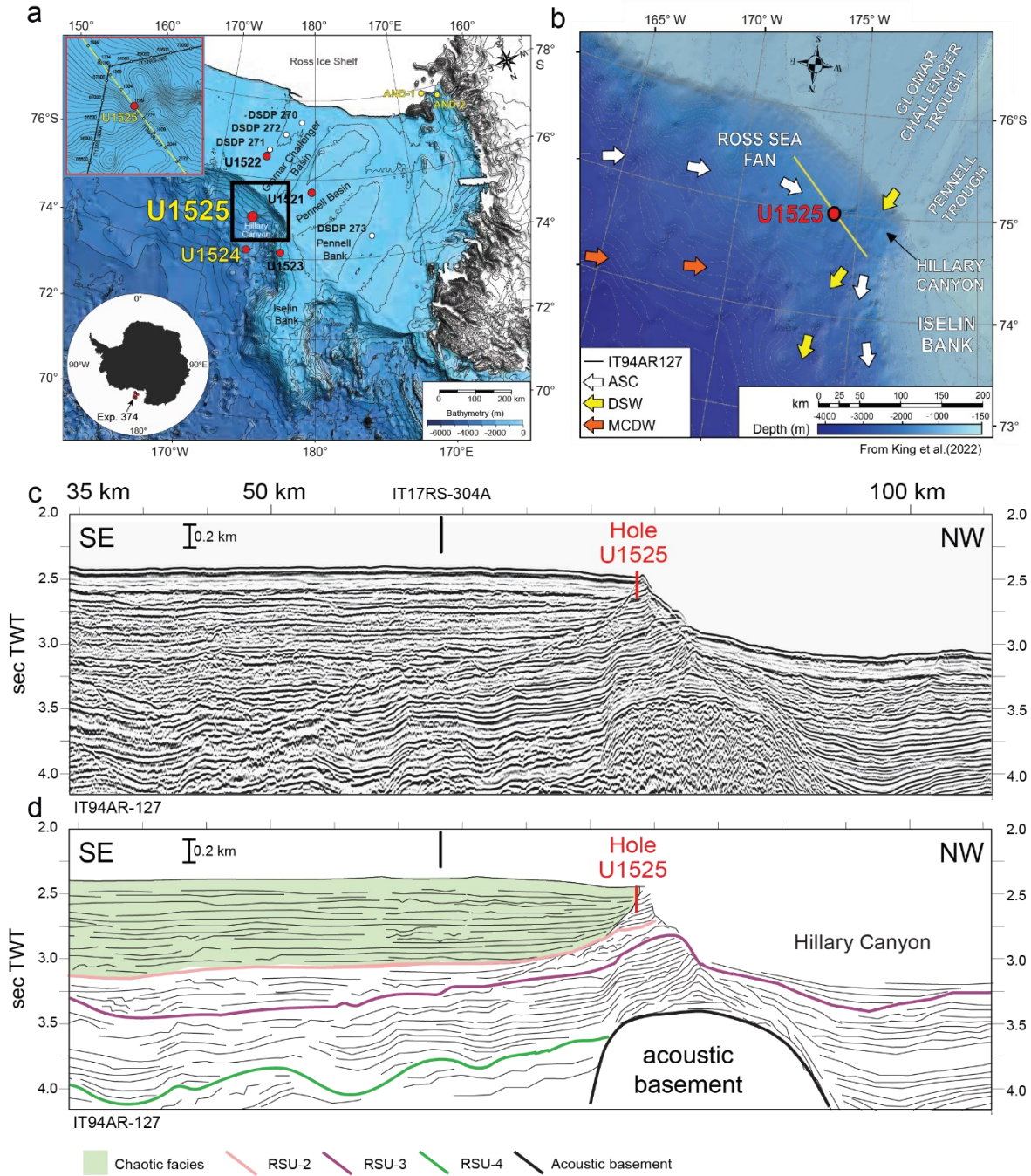


**Figure 1.** (a) Bathymetric map with the location of Sites U1524 and U1525, other IODP Expedition 374 sites (red dots), Deep Sea Drilling Project (DSDP) Leg 28 sites, and Antarctic Geological Drilling Project (AND) drill cores. (b) The red box in the upper left corner shows a zoomed-in location of the seismic line IT94AR127 (yellow line). The black box shows the location of Figure 1.b. Modified from McKay et al. (2019). (b) Direction and location of the main currents (ASC = Antarctic Slope Current) and water masses (DSW = Dense Shelf Water; MCDW = Modified Circumpolar Deep Water) affecting Site U1525. From King et al. (2022) and McKay et al. (2019). (c) Multichannel seismic line IT94AR-127 is shown in C (Finetti et al., unpubl. Data; available from the Antarctic Seismic Data Library System; in King et al., 2022). Highlighted green unit shows TMF facies above Ross Sea Unconformity 2 (RSU2). Modified from McKay et al. (2019) and King et al. (2022).

## 10. Geologic setting and modern oceanography of the Ross Sea

The Ross Sea is one of the major drainage zones for the WAIS (Jacobs et al., 1970; De Santis, 1999; Bergamasco et al., 2002; Budillon et al., 2002; Muench et al., 2009; Gordon et al., 2004; Silvano et al., 2020). The creation of the embayment that is the Ross Sea is linked to crustal thinning and associated rifting that began ~120 Ma with the breakup of Gondwana and the development of the Western Antarctic Rift System (i.e. Jordan et al., 2020). During the Cenozoic, the uplift of the Transantarctic Mountains isolated the Ross Sea from the influence of the East Antarctic Ice Sheet (EAIS) leaving the WAIS as the principal sculptor of its morphology and the main sediment supplier (De Santis, 1999; McKay et al., 2019, Jordan et al., 2020). Therefore, the Ross Sea, and more specifically, its eastern region due to its distance from the Transantarctic Mountains and the EAIS, serves as an archive for the past interactions between the WAIS and the ocean during the last 65 Myr (De Santis et al., 1999).

Three main water masses interact in the modern continental margin region of the Ross Sea: Antarctic Surface Water (AASW; density  $<28$  kg/m<sup>3</sup>), Circumpolar Deep Water (CDW; density between 28-28.27 kg/m<sup>3</sup>), and AABW (density  $>28.27$  kg/m<sup>3</sup>) (Orsi & Wiederwohl, 2009; Morrison et al., 2020; Conte et al., 2021). CDW originates from the relatively warm and salty mid-depth range and is transported from the subtropical regimes of the Southern Ocean (Fig. 1b) (Whitworth III et al., 1998; Orsi & Wiederwohl, 2009). The Antarctic Circumpolar Current (ACC) drives part of CDW to the east, while the remaining volume enters the Ross Gyre, embedded between the colder AASW and AABW below (Whitworth III et al., 1998; Orsi & Wiederwohl, 2009). This overall three-layer structure results in warmer waters flowing into the Ross Sea (Gordon et al., 2009a; Conte et al., 2021). When the warm CDW loses heat as it moves poleward, a modified CDW (mCDW; density between 28.10 to 28.27 kg/m<sup>3</sup>) develops, with similar density but cooler than CDW and separated from it by a 1.5°C isotherm (Orsi & Wiederwohl, 2009; Shadwick et al., 2014; Silvano et al., 2018; Morrison et al., 2020). This mCDW supplies the shelf area with warmer, less-dense waters (Williams et al., 2010; Morrison et al., 2020), that contribute to the formation of Dense Shelf Water (DSW; density  $<28$  kg/m<sup>3</sup>, temperature  $<1.7^{\circ}\text{C}$ , Whitworth III et al., 1998). The transport of CDW/mCDW onto the continental shelf is modulated by a strong gradient of water properties known as the Antarctic Slope Front (ASF) (Gill, 1973; Jacobs, 1991; Thompson et al., 2018; Baines, 2009; Thompson et al., 2020), a hydrographically dense boundary

between the CDW and the shelf waters, that is coupled with the westward flowing Antarctic Slope Current (ASC) (Jacobs, 1991; Thompson et al., 2018, 2020). The ASC and the ASF control the heat transport and other properties, between the continental shelf waters and the warmer mCDW, with the ASC interacting with the main circulation features in the Ross Sea (Jacobs, 1991; Whitworth III et al., 1998; Baines, 2009; Thompson et al., 2018). Thompson et al. (2018) classified the western Ross Sea as a “dense shelf region” for ASC activity. This includes the development of a distinct “V” shape structure that modulates CDW onshore transport and DSW export. Following the V-shape, the CDW flowing towards the shelf first deepens over most of the continental slope. As it approaches the shelf break, it becomes shallow again. The shoaling at the shelf break allows for the DSW, colder and denser, to be transported across the shelf break as a denser layer (Gill, 1973; Baines & Condie, 1998; Thompson et al., 2018).

Dense shelf water is a product of sea ice formation on the Antarctic shelf, which, in turn, causes the loss of heat and the increase of salinity in the remaining water due to brine rejection (Baines & Condie, 1998; Gordon et al., 2004; Morrison et al., 2020). The mixing of the denser, saltier, and colder DSW with the warmer upwelled mCDW downslope allows the production of AABW in the Southern Ocean (Whitworth III et al., 1998; Baines, 2009; Morrison et al., 2020) but this process is limited to a few places in Antarctica.

The Ross and Weddell seas are the main producers of DSW in the modern Southern Ocean (Orsi et al., 1999; Orsi, 2002; Orsi & Wiederwohl, 2009). Their large ice shelves and highly productive polynyas, in addition to the deep and wide continental shelves crossed by large depressions, can accumulate and export large volumes of DSW (Foldvik et al., 2004; Gordon et al., 2004; Ivanov et al., 2004). The continental shelf of the Ross Sea has an average width of ~240 km and a maximum width of ~400 km, and 63% of its ~380,000 km<sup>2</sup> area is deeper than the mean water depth (460 m) of the entire Antarctic continental shelf (Amblas & Dowdeswell, 2018). These physiographic characteristics are ideal for the development of large-scale dense flows that contribute to AABW formation, known in this area as Ross Sea Bottom Water (RSBW) (Orsi et al., 1999; Orsi, 2002; Ivanov et al., 2004; Gordon et al., 2015; Amblas & Dowdeswell, 2018). The RSBW is the coldest (-0.3 to 0°C) and saltiest type (34.7-37.72 PSU) of bottom water formed in the Southern Ocean, with a neutral density > 28.27 kg/m<sup>3</sup> (Jacobs et al., 1970; Orsi & Wiederwohl, 2009; Basak et al., 2015). The neodymium isotopic signature of the RSBW ( $\epsilon_{\text{Nd}} \sim -7$ ) shows that

this water mass can be traced into the Southeast Pacific (Basak et al., 2015), extending its influence outside of the Ross Sea. Therefore, the reconstruction of AABW formation history in the Ross Sea during the Pleistocene, one of its key production sites, provides an opportunity to study the response of the ocean-ice sheet system to past climate change.

## **11. Paleoclimatic evolution during the Pleistocene in the Ross Sea**

The potential paleoclimate value of the continental slope and rise records that are the focus of this study requires a brief review of what is known for this period from other records in the Ross Sea. The Pleistocene was generally characterized by significant advances and retreats of the WAIS across the continental shelf. Consequently, shelf records are fragmentary and commonly include hiatuses and regional unconformities. The success of the ANDRILL project, which drilled beneath the Ross Ice Shelf, provides a robust Pleistocene record. Sediment core AND-1B displays a shift towards more negative  $\delta^{13}\text{C}$  values ( $\sim 27\%$ ) of bulk sedimentary matter after approximately  $\sim 2.6$  Ma. This shift in isotopic composition suggests an increased development of a polynya-style mixing environment, which would have favored the production of Antarctic Bottom Water (AABW) (McKay et al., 2012).

The glaciomarine sequences recovered from AND-1B between  $\sim 2$  and 1 Ma reflect 40-kyr cyclicity, indicative of obliquity forcing (McKay et al., 2012 b). At  $\sim 1$  Ma, the sequences reveal a change from alternating ice shelf/ice sheet sequences to ice shelf/open marine conditions. These open water deposits indicate a reduction, if not a complete collapse, of the WAIS (McKay et al., 2012). The change coincides with Marine Isotopic Stage (MIS) 31 (1.081-1.062 Ma) (Lisiecki & Raymo, 2005), one of the major interglacials of the Pleistocene, with sea surface temperatures in the Ross Sea 3 to 5  $^{\circ}\text{C}$  warmer than the present (Scherer et al., 2008; Naish et al., 2009; Pollard & DeConto, 2009; McKay et al., 2012; Beltran et al., 2020; Warnock et al., 2022; Bollen et al., 2022). After MIS 31, the glaciomarine succession shows a  $\sim 200$  kyr-duration unconformity that coincides with the Mid-Pleistocene Transition (MPT; 1 - 0.8 Ma) (McKay et al., 2012). The MPT was characterized by a shift from glacial-interglacial cycles lasting 40 kyr to 100 kyr, observed in benthic marine  $\delta^{18}\text{O}$  isotope records (Lisiecki & Raymo, 2005) accompanied by an increase in glacial ice volumes (Berger & Jansen, 1994; Lisiecki & Raymo, 2007; Clark et al., 2006). In the

Ross Sea, the MPT is represented by the extension of the marine-based WAIS, characterized by a lithology of diamictites of subglacial proximal to the grounding line.

The record of glaciomarine sequences in AND-1B for the last 800 kyr reveals oscillations of subglacial and ice shelf environments, as a response to changes in ocean temperature and sea level variations while periods of open ocean conditions are more restricted and less evident in the sedimentary record. (McKay et al., 2012 b).

Regarding the ocean response to the ice sheet interactions, Kuijpers (1989) points to a stronger AABW formation in the Southern Ocean from 700 to 400 ka, even with a slower sea ice formation. Bollen et al. (2022) suggest that the DSW export, the precursor of AABW, is higher during interglacials, but with a reduction in channelized export due to the extended ice sheet up to the shelf break. However, there is limited evidence for the AABW formation behavior during the last 2 Myr of advances and retreats of the WAIS in the Ross Sea, and in general, of the ocean response to ice sheet variability in the Southern Ocean during the Pleistocene. The sedimentary record of the DSW-AABW outflow in the Hillary Canyon offers a unique opportunity to characterize the physical evidence of this process, in a proximal-to-distal to the ice sheet environment.

## **12. Study Approach**

### *12.1. Hillary Canyon channel-levee system*

Hillary Canyon is a 180 km long submarine conduit on the eastern Ross Sea continental margin, that shows erosional canyon morphology at the shelf edge and continental slope (Gales et al., 2021) transitioning to depositional channel-levee morphology on the continental rise (Conte et al., 2021). The head of the canyon sits on the shelf edge, at the juncture of the Pennell Trough and Glomar Challenger Basin (Gales et al., 2021), making Hillary Canyon a pathway for the glacial sediments exported from the continental shelf interior through ice streams (De Santis, 1999; Gales et al., 2021). Sediments are delivered downslope through gravity flows (Baines & Condie, 1998; Shapiro, 2003; Ivanov et al., 2004; Gordon et al., 2009b; Gales et al., 2021), with a mixture of sediments and highly saline waters (DSW and mCDW), that are interpreted to contribute to the formation of the levees of Hillary Canyon further down-system due to the overspill of the suspended load downstream through “flow stripping” (Piper & Normark, 1983).

Regional seismic-stratigraphic mapping and reconstruction of the Ross Sea sedimentation history provide important context for our core-based study. Conte et al. (2021) identified eight seismic sequences (Ross Sea Sequences; RSSs) using new seismic-reflection, morpho-bathymetric, and oceanographic data acquired in a 2017 campaign onboard the R/V OGS Explora, in combination with sediment cores, downhole log data, and the age model from IODP Sites U1523 and U1524 (Expedition 374) (Fig. 1c). In the eastern Ross Sea, these RSSs are limited by the regional unconformities (Ross Sea Unconformities; RSUs) defined by seismic reflectors interpreted as the record of advances and retreats of the WAIS (Brancolini et al., 1995b; De Santis, 1999). The sequences reveal the evolution of Hillary Canyon from the Late Oligocene to the Pleistocene and the overall effect of bottom currents, cascading dense shelf water, and sediment supply in the system, all of which can be linked to climatic variations. The onset of active gravity flow deposits in the early Miocene (17-14.5 Ma; deposition of RSS-4) allowed the building up of the levees of the Hillary Canyon. The thickening of RSS-4 hints at stronger bottom currents acting in the Iselin Bank and the continental rise connected to the higher input of sediment through the action of turbidity currents. During the Middle to Late Miocene, (14.5-8 Ma; deposition of RSS-5), there is an enhancement of the biogenic sediment supply from the shelf that would have been funneled by the Hillary Canyon, reflected on the growth of the sedimentary mounds (De Santis et al., 1999; Conte et al., 2021). A hiatus followed during the Late Miocene (8-5 Ma; RSU-3), due to the action of highly erosive bottom currents and lack of deposition in the shelf and the rise. This bottom current activity and DSW production diminished towards the Pliocene, presumably due to the mPWP (~3.3-3 Ma), weakening the Antarctic Slope Front (Conte et al. 2021). By the Pleistocene, the cooling period that came after the warming in the Pliocene would have invigorated the bottom current activity and the formation of polynyas and sea ice, the driving mechanisms for the AABW formation in the Ross Sea (McKay et al., 2012; Conte et. al., 2021).

## 12.2. IODP Site U1524

IODP Site U1524 (74°13.05'S, 173°37.98'W), is 120 km north of the continental shelf edge at 2934 m water depth, on the southeastern levee crest of Hillary Canyon (McKay et al., 2019). In this area, the vertical relief from the thalweg to the levee crest is ~500 m, the width of the channel thalweg is 5 km, and the width of the entire channel system, from levee crest to crest, reaches up to nearly ~45 km (Fig. 1a). The Upper Miocene to Pleistocene sediments recovered from the three

holes at this site are characterized by three lithostratigraphic units (LSUs I-III), from dominantly diatom-rich mud at the base of the core to relatively more terrigenous-rich sediment towards the top (McKay et al., 2019). Hole A, studied here, was drilled up to 282.35 m core depth below the seafloor (CSF-A), with the upper 270.3 m using piston coring and the remaining section with an extended core barrel system. The high recovery of this hole (94%), is the main subject of this study, and more specifically, the last 2.1 Myr that will be compared with the Pleistocene record from Site U1525.

The dominant lithologies at Site U1524 (Fig. 3-Chapter 1) are diatom-bearing/rich mud/sandy mud, muddy diatom ooze, and muddy diamictite. All the contacts between units and subunits are mostly gradational, with a downhole increase in diatom content (McKay et al., 2019). Unit I consists of ~200 m of upper Pliocene to Pleistocene sediments, and is subdivided into subunits IA, IB, and IC, based on their relative biogenic content (McKay et al., 2019). The overall lithology is unconsolidated interbedded massive to laminated diatom-bearing/rich mud, sandy mud, and muddy diatom ooze. A sharp contact between diatom-rich mud and muddy diatom ooze divides Unit I from Unit II, respectively. Unit II consists of interbedded diatom-rich mud and diatom ooze. For Site U1524, we are focusing on Subunit IA (Pleistocene), since it covers the age range (2.1 – 0.7 Ma) where the two Sites (U1524 and U1525) overlap.

The turbidites observed in the two IODP sites studied here (U1524: Fig 2- Chapter 1; U1525: Fig. 2) have a distinctive light yellow-gray color, highly contrasting with the overall gray-to-brown background, and a sharp bottom contact. The top of the beds has an irregular shape, sometimes resembling flame-like structures.

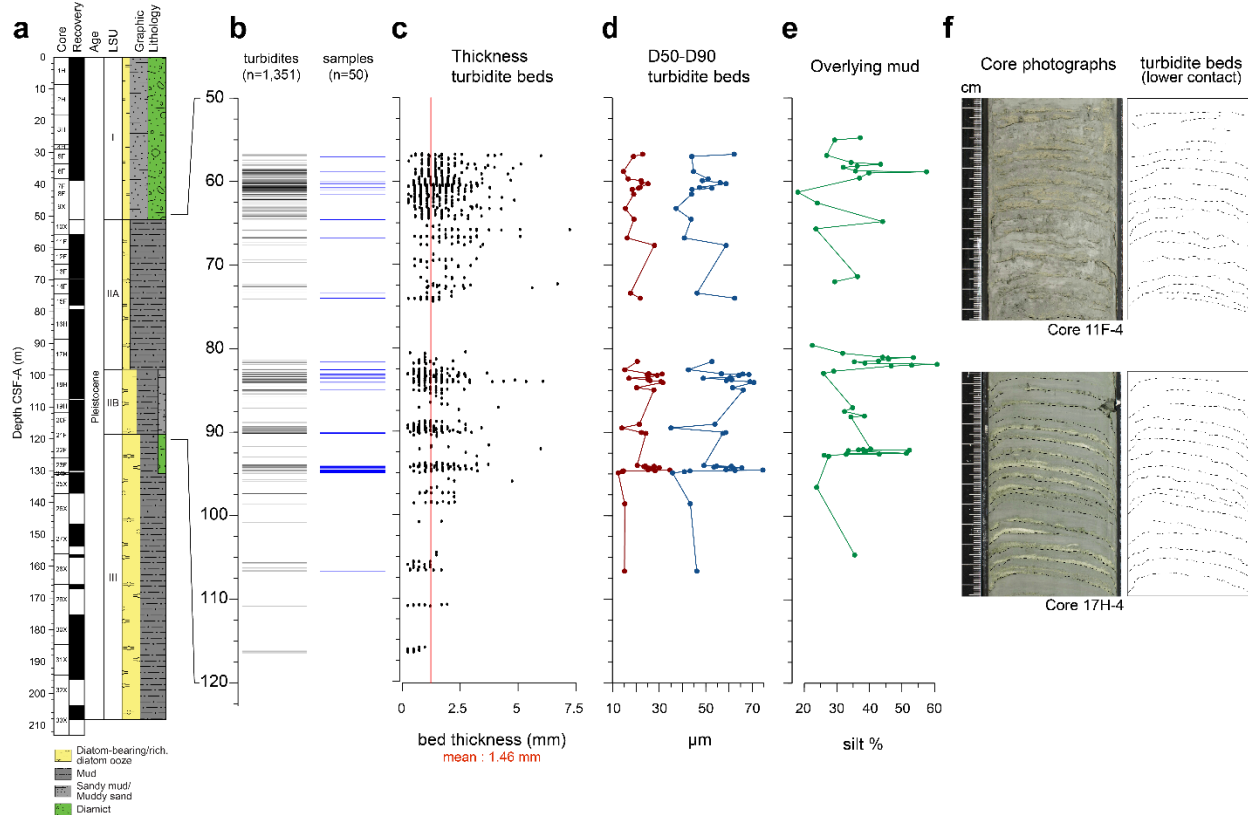


**Figure 2.** (a) Stratigraphic context for IODP Site U1525 (CSF-A in meters). Age datums (in red numbers) are denoted by the red dotted lines. Modified from McKay et al. (2019). (b) Stratigraphic position of all (n=1,351) turbidites with sampled beds (n=50) shown in blue. (c) Thickness of each turbidite bed. The red line represents the mean thickness (1.46 mm). Grain size analysis of fifty-paired samples of turbidites and the overlying mud. Turbidites (d) are characterized by D50 (red) and D90 (blue) (in  $\mu\text{m}$ ). The overlying mud (e) is expressed as silt percentage (%). (f) Core photograph showing the most common sedimentological aspect for Unit IIB (1; core 17H-4) and Unit IIA (2; core 11F-4).

### 12.3. IODP Site U1525

IODP Site U1525, located on the continental slope ( $75^{\circ}0.0603'S$ ,  $173^{\circ}55.2028'W$ ), sits in the southeastern levee of the Hillary Canyon at 1776 m water depth, within the same depositional system as site U1524, located  $\sim 87$  km to the northeast (McKay et al., 2019). Site U1525 is closer to the continental shelf edge (60 km to the southwest) and the mouth of the Pennell and Glomar Challenger basins. The geometry of the Hillary Canyon levees is highly asymmetric in this area: it consists of a 500-meter-relief erosional flank that faces the canyon to the northwest and a 30-meter-relief, less steep flank that faces the canyon to the southeast (McKay et al., 2019). This site lies beneath the westward-flowing Antarctic Slope Current (ASC) (Fig. 1b) and is considered to be stronger and more influential regarding sediment transport compared to the more distal Site

U1524 (Whitworth III et al., 1998; Orsi & Wiederwohl, 2009; McKay et al., 2019). Site U1525 was drilled up to 213 m deep, with a recovery of 158.7 m (73.6%). Site U1525 is divided into three Pleistocene lithostratigraphic units (youngest to oldest: I-III) following IODP Expedition 374 proceedings (McKay et al., 2019).

Unit I (0-51.11 mbsf) is characterized by of unconsolidated massive bioturbated gray diatom-bearing/rich sandy mud with dispersed clasts interbedded on the meter scale with gray to light yellowish-brown clast-poor/rich muddy diamict (McKay et al., 2019; King et al., 2022).

Unit II (51.1-118.58 mbsf), the interval of interest for this study, is composed of mostly greenish-grey, massive to laminated diatom-bearing/rich muds. It also contains a higher and more variable amount of clay than Unit I, and is rich in post-depositional soft sediment deformation features such as cm-scale micro-faulting, as well as cm-scale diamicts and matrix-supported gravel layers (King et al., 2022). This unit was further subdivided into two subunits (IIA and IIB) based on the laminations, coarse fraction content, number of diamict beds  $\geq 1$  cm, and diatom abundance (McKay et al., 2019).

Subunit IIA (51.11- 98.20 mbsf) contains massive to laminated greenish gray to dark greenish gray diatom-bearing mud interbedded at the decimeter to meter scale with diatom-bearing mud/sandy mud with dispersed clasts. The fine sand to silt mm-thick laminae, with sharp lower contacts and yellowish, more abundant in this subunit, are interpreted in this study as turbidite beds, consistent with the “Type A” laminations defined in King et al. (2022)

Subunit IIB (98.2-118.58 mbsf) consists of laminated greenish-gray diatom-rich mud interbedded at the decimeter to meter scale with massive bioturbated olive-gray to greenish-gray diatom-rich sandy mud with dispersed clasts and diamict beds (McKay et al., 2019). The “Type A” lamination here is weaker than in the overlying subunit IIA, and the greyer silty laminae, with sharp upper and lower contacts and no grading, defined in King et al. (2022) as the “Type B” layers, is more common here. These laminae, interbedded with larger, gravel-sized clasts, are not part of this study, since have been interpreted to be the product of bottom current activity (King et al., 2022). For this study, Subunits IIA and IIB are the main objectives due to the presence of turbidite layers, or “Type A” laminations of King et al. (2022).

Unit III (118.58- 208.7 mbsf) is composed of laminated greenish-gray diatom-rich mud to muddy diatom ooze interbedded at the decimeter scale with massive bioturbated light greenish gray diatom-rich sandy mud to muddy diatom ooze with dispersed clasts and diamict (McKay et al., 2019). There are no identifiable turbidite beds in this unit.

#### *12.4. Chronology of the turbidite and age models for Sites U1524 and U1525*

To define the ages of the turbidite layers, we employed the most recent age models available for each site as outlined in Expedition 374 Proceedings (McKay et al., 2019), supplemented by any subsequent post-expedition refinements. These age models were constructed utilizing magnetic polarity reversals, with additional support from diatom and radiolarian biostratigraphy (McKay et al., 2019). The magnetic polarity zones were subsequently correlated with the geomagnetic polarity timescale proposed by Gradstein et al. (2012).

In the context of this investigation, we utilized the latest post-expedition age datums for Site U1524 (Fig. 4), while for Site U1525, we relied on the existing shipboard datums. To determine the age of each layer of interest, we calculated the linear accumulation rate between each age tie point. The accumulation rate for each interval was then applied to compute the age of each layer based on their mid-depth point. The mid-depth was calculated as the average depth between the top and bottom of each layer. These chronological constraints show that there is a 1.4 Myr-long interval (2.1-0.7 Ma) that is present in both sites, thus allowing for an investigation of the broader slope to rise depositional system during that time.

#### *12.5. Methods for Core Characterization*

The sedimentological characterization of the turbidite beds in Sites U1524 and U1525 focuses on three parameters: the stratigraphic position and total number of turbidite beds, the thickness of the turbidite beds, and the grain size of a representative sampling of the turbidite beds and the mud directly overlying these beds through the succession.

##### *12.5.1. Occurrence and thickness of the turbidite beds*

We visually identified the beds in high-resolution core photographs and, using a custom MATLAB script recorded the position of the base and top of each bed, which allowed for determination of their thickness. During this process, we also evaluated the lateral continuity and

other descriptive characteristics of these turbidite beds (e.g., the nature of bed contacts). The depth midpoint of each bed was converted to age through linear interpolation using the shipboard age model as mentioned above.

#### *12.5.2. Grain-size analysis of the turbidite beds and overlying mud*

For the shared age interval between Sites U1525 and U1524 (2.1 to 0.7 Ma), we identified and selected twenty and fifty samples from Site U1524 and U1525, respectively, of the turbidite beds and their corresponding overlying mud intervals, to represent the distribution along the core and sedimentological variations, including thickness and lateral continuity of the beds (Fig. 4). We sampled those turbidite beds from the core using a 10 cm<sup>3</sup> wedge plastic tool, and a 20 cm<sup>3</sup> half-round plastic scoop for the overlying mud.

To characterize the grain size distributions of the turbidite beds, we used a laser particle analyzer (Malvern MasterSizer 3000). The average amount of sediment obtained from each bed was up to 2 g. Since the sediment was non-cohesive and homogeneous silty material, no chemical treatment was necessary, and we measured it directly on the laser particle analyzer. We manually poured the sediment into the wet dispersion unit until it reached a stable obscuration range of 8-10%. Each sample was measured three times using the instrument's sequence. If the sample showed irregular distribution during the measurements (i.e., large variations between each of the three measurements), additional measurements were taken up to 6 times, if necessary, to ensure data quality. The output data was processed using Gradistat version 9.1 (Blott & Pye, 2001), and the results are displayed in volume percentage. We summarized the grain-size data by calculating the median (50th percentile; D50) and the 90th percentile (D90) from the distributions.

To assess the nature of the finer-grained deposits directly overlying the turbidite beds, we generated grain size data using the Micromeritics SediGraph 5100. The SediGraph is a preferred method for clay-rich sediments (1-63  $\mu\text{m}$  fraction) because it measures particle size based on particle settling velocity following Stokes' law, reducing inaccuracies due to the particle shape effect (McCave & Hall, 2006). Before analysis, we wet-sieved the sample at 63  $\mu\text{m}$ , dried the coarser (>63  $\mu\text{m}$ ) fraction in an oven at 50°C for 48 hours, and then weighed it to calculate the mass percentage of the sand fraction. The finer (<63  $\mu\text{m}$ ) fraction was also dried and weighed, and 1 g was analyzed in the SediGraph. We dispersed the sample in 5 ml of 10% NaOH solution before

pouring it into the SediGraph chamber to aid deflocculation. We processed the SediGraph output files with a custom R script to calculate the proportion of silt (4-63  $\mu\text{m}$ ) by mass in these clay-rich sediments.

## 13. Results

### 13.1. *Turbidite bed occurrence, frequency, and thickness*

In the time interval of interest (2.1 to 0.7 Ma), there are 254 turbidite beds in U1524, out of a total of 3,329 observed throughout the entire core, which spans from 3.33 Ma (see Chapter 1). This significant decrease in the upper section of Site U1524 ( $\sim 7.6\%$  of the total occurrence) contrasts with the overall higher occurrence of turbidite beds in U1525 for the same interval, which totals 1,351 (Fig. 4).

In Site U1525, there is a sparser occurrence of turbidite beds from the base of the record until  $\sim 1.25$  Ma, which shifts to a higher number up to 1.072 Ma, followed by a gap (Fig 2b). The turbidite beds reappear with a high frequency at  $\sim 0.92$  Ma, until  $\sim 0.7$  Ma, which coincides with the end of the recovered core section for lithostratigraphic Unit IIA. When plotted in 20 kyr increments, these two identifiable “clusters” of high turbidite frequency in U1525 (Fig. 3) have some differences: the bottom cluster ( $\sim 1.41$  Ma to  $\sim 1.072$  Ma), has a lower frequency (486 turbidite beds in 340 kyr) compared with the top cluster ( $\sim 0.92$  Ma to 0.7 Ma), which has a higher frequency of turbidite beds (786 turbidite beds in 200 kyr). Within each cluster, there is an overall trend to gradually increase from the bottom to the top, and the bottom cluster reaches a higher frequency in the upper portion ( $>150$  turbidite beds/20 kyr). The bed thicknesses do not show a pronounced variability between the clusters, with an average of 1.40 mm for the bottom cluster and 1.50 mm for the top cluster (Fig 2c). The core image analysis, which captures morphological differences between each cluster, did not show any major difference between the two (Fig 2f). Up to 1.2 Ma, however, the occurrence of turbidite beds between U1524 and U1525 follows a similar pattern, and it is possible to recognize similar increases in frequency density (Fig. 4). The average thickness of the turbidite beds for the 2.1 Ma to 0.7 Ma interval in U1524 has a slightly larger value:  $\sim 2.1$  mm vs the 1.4-1.5 mm for U1525 (Fig 5a).



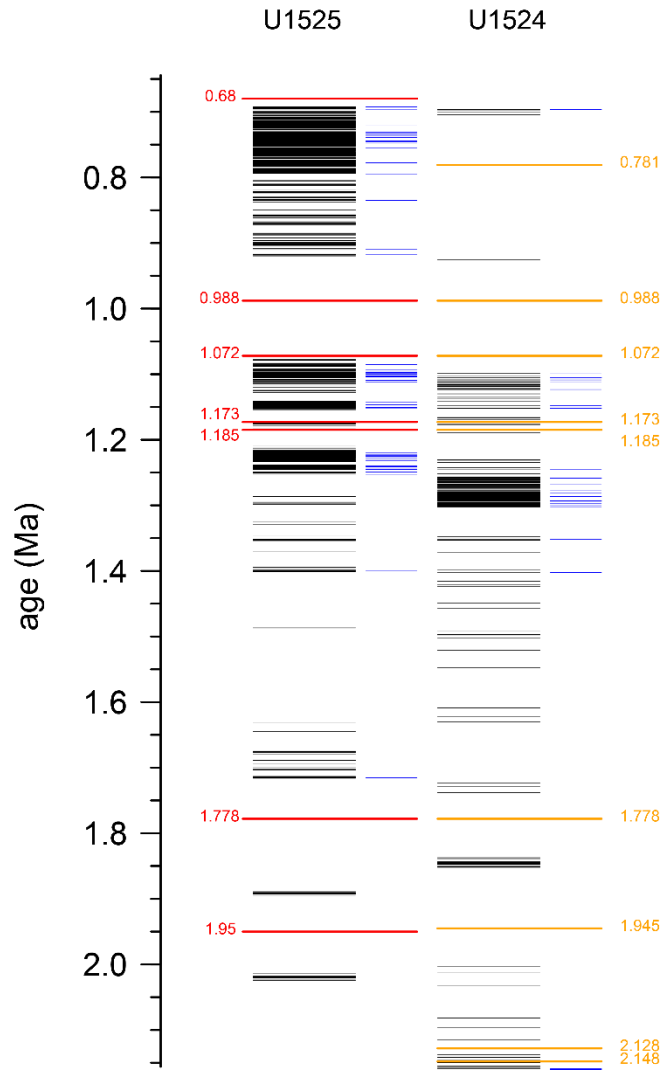


**Figure 4.** Comparative plots of the turbidite frequency for Sites U1525 and U1524 for the U1525 time span (2.1-0.7 Ma). The red and orange lines are the correspondent age datums for each Site. The blue lines show the samples taken for grain size data.

### 13.2. Grain size

The grain size median (D50) for the turbidite beds of U1525 in the 2.1-0.7 Ma, falls in the 13-35  $\mu\text{m}$  range (fine to medium silt in the Wentworth scale), slightly coarser than the range for the samples in Site U1524 for the same interval (5 -24  $\mu\text{m}$ ; very fine silt to medium silt) (Fig. 5b). The D90 of the grain size distribution shows a similar pattern, where Site U1525 has a larger grain size range, from 35-75  $\mu\text{m}$  (coarse silt to very fine sand) against 20-60  $\mu\text{m}$  (medium to coarse silt), except for an outlier at around ~45 m (~1.2 Ma).

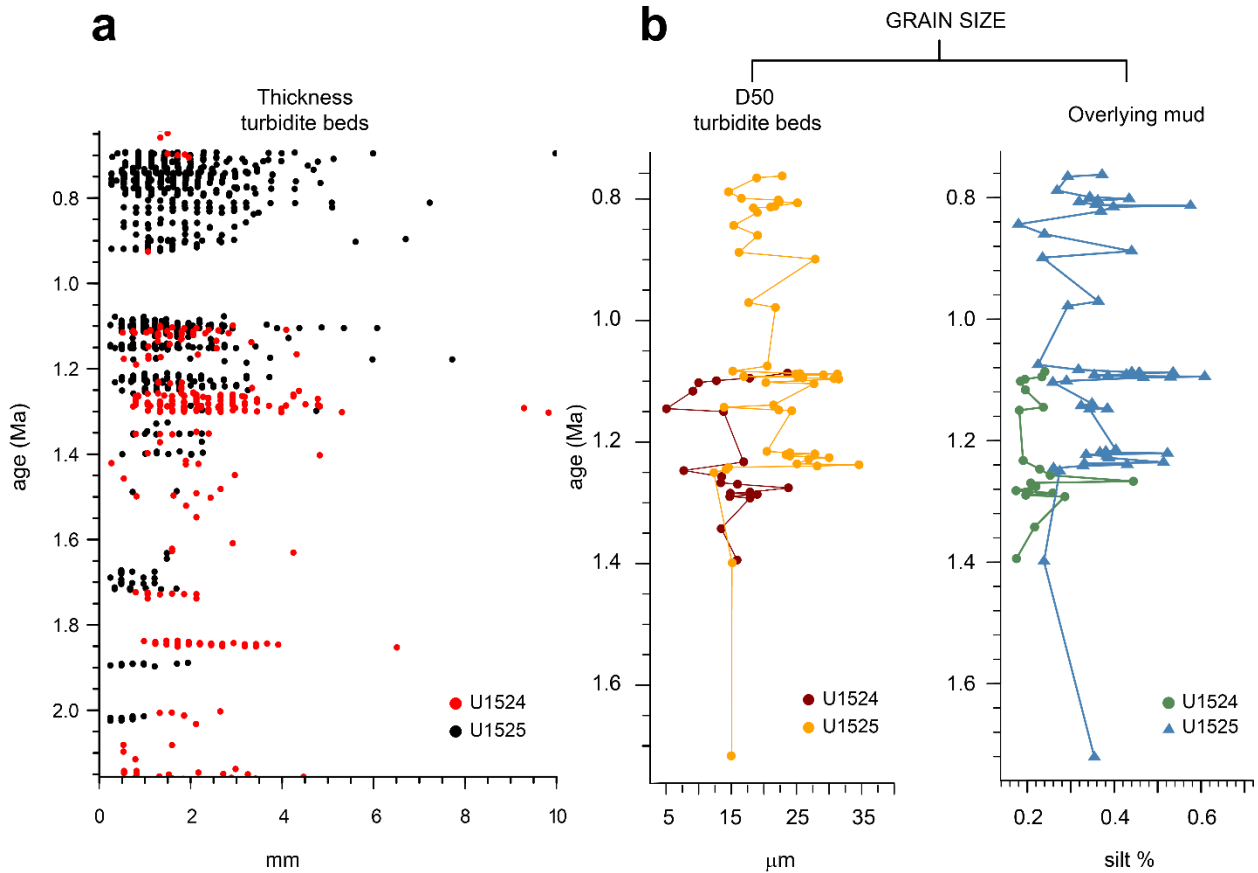


**Figure 5.** Comparative plots of thickness and grain size of the turbidite beds for Sites U1525 and U1524 (a) Thickness of the turbidite beds between 2.1 Ma to 0.7 Ma for each site. The thicknesses for this time interval do not show a clear difference between the sites (b) The average grain size of the turbidite beds (left) and its overlying mud (right) between 8 Ma to 16.5 Ma. U1524 shows an overall less coarse sediment if compared with the same interval for U1525.

## 14. Discussion

### 14.1. *Proximal to distal depositional patterns of the dense shelf water plume from 2.1 to 1 Ma*

The analysis of key sedimentological parameters, including bed frequency, thickness, and grain size, within the turbidite record at IODP Sites U1524 and U1525, has allowed the comparison of the sedimentary records related to the formation processes of DSW-AABW between 2.1-07 Ma. The grain size differences, around  $\sim 10 \mu\text{m}$  larger in the continental slope (Site U1525) than in the rise (Site U1524), point to the proximity to the sediment source, in this case, the continental shelf and uppermost slope. The DSW plume, originated in the Ross Sea shelf, would have progressively decreased its transport energy downslope Hillary Canyon, leaving the coarser sediment fraction in the section closer to the shelf. This is reflected in the grain size difference for the turbidite deposits of the IODP Sites drilled in the levee of this submarine-canyon system.

The comparison of the bed thicknesses shows that Site U1524 has a thicker bed average (2.1 mm) than U1525 (1.5 mm) for the same interval. However, the significant difference in the frequency of turbidite beds for that interval (254 beds in U1524 vs 1,351 in U1525), can skew the averages towards lower values in U1525. Therefore, the thickness variability needs to be further investigated for a more accurate interpretation in this context.

One of the more significant findings in this study is the similarity of the turbidite frequency in both sites, following a very similar pattern until around 1.072 Ma (Fig. 4). This change happens within Marine Isotopic Stage 31 (1.081-1.062 Ma) when warming is interpreted to have increased the sea surface temperature between 3-5°C in the Ross Sea (see section 3). The warming would have caused a strong reduction or even the collapse of the WAIS, according to several proxies indicating open marine conditions at the time (e.g., Scherer et al., (2008), Pollard & DeConto, (2009), McKay et al., (2012)). This would have impacted the DSW-AABW production, due to the higher temperatures preventing the sea ice formation, along with the melting of the WAIS causing the freshening and the stratification of the water masses in the Southern Ocean (Golledge et al., 2014; Beltran et al., 2020), some of the key factors influencing the DSW-AABW formation. Therefore, the gap in turbidite deposition after  $\sim 1$  Ma, present in both sites, can be interpreted as a cessation of DSW-AABW export during the MIS 31 interglacial.

MIS 31 is followed by the Mid-Pleistocene transition (1-0.8 Ma) when glacial-interglacial cycles shifted from a periodicity of 41 kyr to 100 kyr (Lisiecki & Raymo, 2005). During this time, ice volume increased by the sea-level equivalent of ~50 m (Clark et al., 2006). These progressively colder conditions would have promoted the re-initiation of the DSW-AABW formation, which we interpreted to happen at around 900 ka with Site U1525 turbidite frequency record. Within the MPT, Clark et al. (2006) identified the “900 ka” cooling event in the LR04  $\delta^{18}O$  benthic stack (Lisiecki & Raymo, 2005), which marks the lowest sea surface temperature (SST) in the North Atlantic, with a net cooling of ~9°C (Clark et al., 2006; Kemp et al., 2010). In the Southern Ocean, the northward migration of the Antarctic Polar Front (APF) coincided with a notable reduction in the mean flow speed of the Deep Western Boundary Current. This observation, derived from the analysis of sortable silt data from the Chatham Rise (Hall et al., 2001), is indicative of a diminished rate of deep Pacific Ocean ventilation by dense Antarctic waters. Consequently, this is associated with a decline in the production and export of AABW during the MPT (Kemp et al., 2010). For Site U1525, however, the frequency of turbidites increased after 900 ka, but with a lower frequency than before the ~1 Ma gap (Fig. 3d), which could reflect the local reduction in AABW production.

#### *14.2. Depositional variations between ice sheet proximal Site U1525 and distal Site U1524 after 1 Ma*

For Site U1524, however, the turbidite record is almost absent after 1.072 Ma, except for a short period around 0.7 Ma, coinciding with the end of MPT. We consider two main hypotheses to explain why Site U1525 records turbidity current deposition and Site U1524 does not at this time: one, that considers the effect of the bottom current activity in the slope of the Ross Sea (i.e., the Antarctic Slope Current, ASC), and a second, that considers the gradual WAIS growth over the Pleistocene, up to the shelf break, that pushed the DSW production towards the open ocean.

The ASC activity is thought to have strengthened and intensified during the Pleistocene in the Ross Sea (Conte et al., 2021). This is indicated by the presence of sediment drifts (contourite deposits) recording the action of bottom currents in the Ross Sea seismic sequences (RSS-7) west of Hillary Canyon. The growth of contouritic mounds within RSS-7 against the flank of the Iselin Bank therefore indicates the resumption of intense bottom water circulation along the continental rise during the Pleistocene cooling. During full glacial periods, however, the continental shelf of the

Ross Sea would have been covered by the ice sheet, forcing the ASC to circulate in a narrow area of the slope, reducing the energy exchanges with the other water masses across the shelf, and therefore intensifying the transport energy of the current (Conte et al., 2021). We propose that the heightened ASC strength led to the redistribution of sediments carried in the dense shelf water plume cascading down the Hillary Canyon. An invigorated ASC positioned down-system from Site U1525, along the base of the slope, would have effectively dispersed the sediment plume, making it incapable of leaving a physical record of its activity down to the continental rise, where Site U1524 is situated (Fig. 6b)

Regarding the ice sheet expansion during glacial periods and its effect on dense shelf water outflow, Amblas and Dowdeswell (2018) propose that DSW formation during glacial periods occurred in open-ocean polynya settings sustained by the upwelling of the CDW. Consequently, such export is anticipated to be less focused in specific bathymetric conduits on the slope and therefore less likely to generate energetic plumes capable of resuspending and depositing sediments, such as the turbidite beds in the levees of the Hillary Canyon. This interpretation aligns with previous research, which indicated that, during partial ice sheet advances across the continental shelf, DSW might have been generated in coastal and ice front polynyas, mirroring contemporary conditions (Fig. 6c) (Hillenbrand et al., 2017; Amblas & Dowdeswell, 2018; Bollen et al., 2022).

Since the turbidite record for the ~1 Ma to 0.7 Ma does exist in Site U1525, we propose that the absence of turbidite beds in Site U1524 for that same period is predominantly an effect of the strengthened ASC circulation in the Ross Sea, redistributing the sediment to areas outside of the channel-levee system before it reaches the lower slope-rise area. However, the probability of a DSW-AABW production in open ocean polynyas ocean during full glacial conditions cannot be disregarded, but further evidence of that process is needed. The shift to diamict-dominated lithofacies from ~0.7 Ma to present at Site U1525 (lithostratigraphic unit I; Fig. 1a) records the onset of trough-mouth fan deposition (King et al., 2022) and the cessation of fine-grained turbiditic accumulation at this position of the Hillary Canyon system. To what extent this significant shift in slope sedimentation influenced the DSW-AABW outflow system more broadly is unknown but could have also played a role in the relative lack of turbidites observed at Site U1524 for this period.

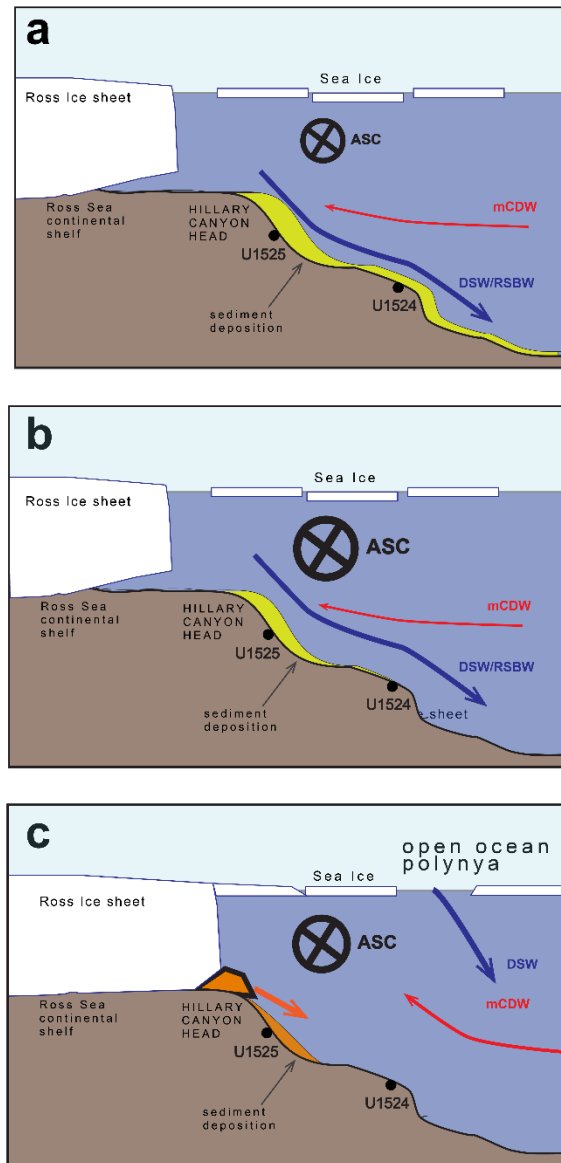


**Figure 6.** Proposed scenarios to explain the sedimentation patterns of turbidite beds in the Hillary Canyon over the past ~2.1 million years. (a) 2.1-1 million years ago: The ice sheet's position facilitated the formation of dense shelf water (DSW) on the continental shelf, and cooling conditions promoted the development of polynyas and sea ice. While the Antarctic Slope Current (ASC) was active, it allowed downslope sediments (in green) to settle along the Hillary Canyon. (b) Post 9000 ka: The ASC's transport energy intensified, causing the stronger current to redistribute sediments carried by the DSW plume, hindering downslope deposition at Site U1524. (c) An alternative explanation for the scarcity of turbidites in Site U1524, compared to the higher frequency in U1525 after 900 ka: The ice sheet likely reached the shelf break during glacial times, impeding DSW formation on the continental shelf. However, the DSW formation would have still happened in open ocean polynyas. Thus, Hillary Canyon is no longer the conduit for dense shelf water cascading, and therefore, the process is not recorded in its levees. In addition, the full glacial state brings sediments to the shelf edge than can collapse, causing slope failures and gravity flows. In this case, these processes are recorded by the glaciomarine sediment of Unit I in Site U1525.

## 15. Conclusions

The sedimentary analysis of turbidite beds in IODP Sites U1524 and U1525 between 2.1 Ma to 0.7 Ma reveals distinct patterns in bed frequency, thickness, and grain size. While the more proximal Site U1525 exhibits an overall higher occurrence of turbidite beds during this interval, both sites share a similar turbidite frequency pattern until around 1.072 Ma. After that, there is a significant gap in turbidite deposition, which we interpreted as a cessation of DSW-AABW export during the MIS 31 interglacial. This warming was followed by the Mid-Pleistocene transition (1-0.8 Ma), which corresponds to an increase in ice volume and marks the re-initiation of DSW-AABW formation, as we observed in the turbidite record at Site U1525. Grain size analysis of the turbidite beds and its overlying mud confirms that the origin of the dense shelf water plume occurs in the Ross Sea shelf since the coarser sediment is deposited at Site U1525, closer to the shelf edge, while at Site U1524 for the same period, the grain size is slightly less coarse.

Further examination of depositional variations after 1 Ma distinguishes the two sites. The more distal Site U1524 shows an almost absent turbidite record after 1.072 Ma, except around 0.7 Ma, in contrast to Site U1525, which maintains a high-frequency of turbidite beds for the same period. Hypotheses explaining this difference involve the influence of bottom current activity, specifically the Antarctic Slope Current (ASC), and gradual West Antarctic Ice Sheet (WAIS) growth. The strengthened ASC circulation is proposed as a factor redistributing sediments that would have otherwise been recorded at the more distal Site U1524.

The overall similarity in turbidite frequency patterns in both sites until around 1.072 Ma underscores the impact of environmental changes, particularly associated with MIS 31 interglacial warming event and the subsequent Mid-Pleistocene transition. This study also highlights the potential role of open-ocean polynyas in DSW-AABW production during full glacial conditions. However, further evidence is needed to understand this process and where it is preserved in the sedimentary record. In conclusion, the sedimentological parameters studied provide valuable insights into the complex interplay of environmental factors influencing the depositional history of turbidites in the Ross Sea region over the past 2.1 million years.

## 16. References Cited

- Amblas, D., & Dowdeswell, J. A. (2018). Physiographic influences on dense shelf-water cascading down the Antarctic continental slope. *Earth-Science Reviews*, 185, 887–900. <https://doi.org/10.1016/j.earscirev.2018.07.014>
- Baines, P. G. (2009). A model for the structure of the Antarctic Slope Front. *Deep Sea Research Part II: Topical Studies in Oceanography*, 56(13–14), 859–873. <https://doi.org/10.1016/j.dsr2.2008.10.030>
- Baines, P. G., & Condie, S. (1998, March 18). Observations and Modelling of Antarctic Downslope Flows: A Review. *AGU Journals; American Geophysical Union (AGU)*. <https://onlinelibrary.wiley.com/doi/abs/10.1029/AR075p0029>
- Basak, C., Pahnke, K., Frank, M., Lamy, F., & Gersonde, R. (2015). Neodymium isotopic characterization of Ross Sea Bottom Water and its advection through the southern South Pacific. *Earth and Planetary Science Letters*, 419, 211–221. <https://doi.org/10.1016/j.epsl.2015.03.011>
- Beltran, C., Golledge, N. R., Ohneiser, C., Kowalewski, D. E., Sicre, M.-A., Hageman, K. J., Smith, R., Wilson, G. S., & Mainié, F. (2020). Southern Ocean temperature records and ice-sheet models demonstrate rapid Antarctic ice sheet retreat under low atmospheric CO<sub>2</sub> during Marine Isotope Stage 31. *Quaternary Science Reviews*, 228, 106069. <https://doi.org/10.1016/j.quascirev.2019.106069>
- Bergamasco, A., Defendi, V., Zambianchi, E., & Spezie, G. (2002). Evidence of dense water overflow on the Ross Sea shelf-break. *Antarctic Science*, 14(3), 271–277. <https://doi.org/10.1017/S0954102002000068>
- Berger, W. H., & Jansen, E. (1994). Mid-Pleistocene Climate Shift—The Nansen Connection. In *The Polar Oceans and Their Role in Shaping the Global Environment* (pp. 295–311). American Geophysical Union (AGU). <https://doi.org/10.1029/GM085p0295>

- Blott, S. J., & Pye, K. (2001). GRADISTAT: A grain size distribution and statistics package for the analysis of unconsolidated sediments. *Earth Surface Processes and Landforms*, 26(11), 1237–1248. <https://doi.org/10.1002/esp.261>
- Bollen, M., Riesselman, C. R., Ohneiser, C., Albot, O., McKay, R., Lee, M. K., Yoo, K.-C., Kim, S., Lee, J. I., & Levy, R. (2022). Pleistocene oceanographic variability in the Ross Sea: A multiproxy approach to age model development and paleoenvironmental analyses. *Global and Planetary Change*, 216, 103901. <https://doi.org/10.1016/j.gloplacha.2022.103901>
- Budillon, G., Gremes Cordero, S., & Salusti, E. (2002). On the dense water spreading off the Ross Sea shelf (Southern Ocean). *Journal of Marine Systems*, 35(3–4), 207–227. [https://doi.org/10.1016/S0924-7963\(02\)00082-9](https://doi.org/10.1016/S0924-7963(02)00082-9)
- Clark, P. U., Archer, D., Pollard, D., Blum, J. D., Rial, J. A., Brovkin, V., Mix, A. C., Pisias, N. G., & Roy, M. (2006). The middle Pleistocene transition: Characteristics, mechanisms, and implications for long-term changes in atmospheric pCO<sub>2</sub>. *Quaternary Science Reviews*, 25(23), 3150–3184. <https://doi.org/10.1016/j.quascirev.2006.07.008>
- Conte, R., Rebesco, M., De Santis, L., Colleoni, F., Bensi, M., Bergamasco, A., Kovacevic, V., Gales, J., Zgur, F., Accettella, D., De Steur, L., Ursella, L., McKay, R., Kim, S., & Lucchi, R. G. (2021). Bottom current control on sediment deposition between the Iselin Bank and the Hillary Canyon (Antarctica) since the late Miocene: An integrated seismic-oceanographic approach. *Deep Sea Research Part I: Oceanographic Research Papers*, 176, 103606. <https://doi.org/10.1016/j.dsr.2021.103606>
- De Santis, L. (1999). The Eastern Ross Sea continental shelf during the Cenozoic: Implications for the West Antarctic ice sheet development. *Global and Planetary Change*, 23(1–4), 173–196. [https://doi.org/10.1016/S0921-8181\(99\)00056-9](https://doi.org/10.1016/S0921-8181(99)00056-9)
- Foldvik, A., Gammelsrød, T., Østerhus, S., Fahrbach, E., Rohardt, G., Schröder, M., Nicholls, K. W., Padman, L., & Woodgate, R. (2004). Ice shelf water overflow and bottom water formation in the southern Weddell Sea. *Journal of Geophysical Research: Oceans*, 109(C2).

- Gales, J., Rebesco, M., De Santis, L., Bergamasco, A., Colleoni, F., Kim, S., Accettella, D., Kovacevic, V., Liu, Y., Olivo, E., Colizza, E., Florindo-Lopez, C., Zgur, F., & McKay, R. (2021). Role of dense shelf water in the development of Antarctic submarine canyon morphology. *Geomorphology*, 372, 107453. <https://doi.org/10.1016/j.geomorph.2020.107453>
- Gill, A. E. (1973). Circulation and bottom water production in the Weddell Sea. *Deep Sea Research and Oceanographic Abstracts*, 20(2), 111–140. [https://doi.org/10.1016/0011-7471\(73\)90048-X](https://doi.org/10.1016/0011-7471(73)90048-X)
- Golledge, N. R., Menviel, L., Carter, L., Fogwill, C. J., England, M. H., Cortese, G., & Levy, R. H. (2014). Antarctic contribution to meltwater pulse 1A from reduced Southern Ocean overturning. *Nature Communications*, 5(1), Article 1. <https://doi.org/10.1038/ncomms6107>
- Gordon, A. L. (1991). The Role of Thermohaline Circulation in Global Climate Change. <https://doi.org/10.7916/D8M04G8H>
- Gordon, A. L. (2001). Bottom Water Formation. In *Encyclopedia of Ocean Sciences* (pp. 334–340). Elsevier. <https://doi.org/10.1006/rwos.2001.0006>
- Gordon, A. L., Orsi, A. H., Muench, R., Huber, B. A., Zambianchi, E., & Visbeck, M. (2009a). Western Ross Sea continental slope gravity currents. *Deep Sea Research Part II: Topical Studies in Oceanography*, 56(13), 796–817. <https://doi.org/10.1016/j.dsr2.2008.10.037>
- Gordon, A. L., Orsi, A. H., Muench, R., Huber, B. A., Zambianchi, E., & Visbeck, M. (2009b). Western Ross Sea continental slope gravity currents. *Deep Sea Research Part II: Topical Studies in Oceanography*, 56(13–14), 796–817. <https://doi.org/10.1016/j.dsr2.2008.10.037>
- Gordon, A. L., Zambianchi, E., Orsi, A., Visbeck, M., Giulivi, C. F., Whitworth, T., & Spezie, G. (2004). Energetic plumes over the western Ross Sea continental slope: ROSS SEA PLUMES. *Geophysical Research Letters*, 31(21), n/a-n/a. <https://doi.org/10.1029/2004GL020785>

- Gradstein, F. M., & Ogg, J. G. (2012). Chapter 2—The Chronostratigraphic Scale. In F. M. Gradstein, J. G. Ogg, M. D. Schmitz, & G. M. Ogg (Eds.), *The Geologic Time Scale* (pp. 31–42). Elsevier. <https://doi.org/10.1016/B978-0-444-59425-9.00002-0>
- Hall, I. R., McCave, I. N., Shackleton, N. J., Weedon, G. P., & Harris, S. E. (2001). Intensified deep Pacific inflow and ventilation in Pleistocene glacial times. *Nature*, 412(6849), Article 6849. <https://doi.org/10.1038/35090552>
- Hillenbrand, C.-D., Smith, J. A., Hodell, D. A., Greaves, M., Poole, C. R., Kender, S., Williams, M., Andersen, T. J., Jernas, P. E., Elderfield, H., Klages, J. P., Roberts, S. J., Gohl, K., Larter, R. D., & Kuhn, G. (2017). West Antarctic Ice Sheet retreat driven by Holocene warm water incursions. *Nature*, 547(7661), Article 7661. <https://doi.org/10.1038/nature22995>
- Huang, X., Stürz, M., Gohl, K., Knorr, G., & Lohmann, G. (2017). Impact of Weddell Sea shelf progradation on Antarctic bottom water formation during the Miocene. *Paleoceanography*, 32(3), 304–317. <https://doi.org/10.1002/2016PA002987>
- Ivanov, V. V., Shapiro, G. I., Huthnance, J. M., Aleynik, D. L., & Golovin, P. N. (2004). Cascades of dense water around the world ocean. *Progress in Oceanography*, 60(1), 47–98. <https://doi.org/10.1016/j.pocean.2003.12.002>
- Jacobs, S. S. (1991). On the nature and significance of the Antarctic Slope Front. *Marine Chemistry*, 35(1), 9–24. [https://doi.org/10.1016/S0304-4203\(09\)90005-6](https://doi.org/10.1016/S0304-4203(09)90005-6)
- Jacobs, S. S., Amos, A. F., & Bruchhausen, P. M. (1970). Ross sea oceanography and antarctic bottom water formation. *Deep Sea Research and Oceanographic Abstracts*, 17(6), 935–962. [https://doi.org/10.1016/0011-7471\(70\)90046-X](https://doi.org/10.1016/0011-7471(70)90046-X)
- Jordan, T. A., Riley, T. R., & Siddoway, C. S. (2020). The geological history and evolution of West Antarctica. *Nature Reviews Earth & Environment*, 1(2), Article 2. <https://doi.org/10.1038/s43017-019-0013-6>

- Kemp, A. E. S., Grigorov, I., Pearce, R. B., & Naveira Garabato, A. C. (2010). Migration of the Antarctic Polar Front through the mid-Pleistocene transition: Evidence and climatic implications. *Quaternary Science Reviews*, 29(17), 1993–2009. <https://doi.org/10.1016/j.quascirev.2010.04.027>
- King, M. V., Gales, J. A., Laberg, J. S., McKay, R. M., De Santis, L., Kulhanek, D. K., Hosegood, P. J., & Morris, A. (2022). Pleistocene depositional environments and links to cryosphere-ocean interactions on the eastern Ross Sea continental slope, Antarctica (IODP Hole U1525A). *Marine Geology*, 443, 106674. <https://doi.org/10.1016/j.margeo.2021.106674>
- Kuijpers, A. (1989). Southern Ocean circulation and global climate in the Middle Pleistocene (early Brunhes). *Palaeogeography, Palaeoclimatology, Palaeoecology*, 76(1), 67–83. [https://doi.org/10.1016/0031-0182\(89\)90104-1](https://doi.org/10.1016/0031-0182(89)90104-1)
- Lisiecki, L. E., & Raymo, M. E. (2005). A Pliocene-Pleistocene stack of 57 globally distributed benthic  $\delta^{18}\text{O}$  records. *Paleoceanography*, 20(1). <https://doi.org/10.1029/2004PA001071>
- Lisiecki, L. E., & Raymo, M. E. (2007). Plio–Pleistocene climate evolution: Trends and transitions in glacial cycle dynamics. *Quaternary Science Reviews*, 26(1), 56–69. <https://doi.org/10.1016/j.quascirev.2006.09.005>
- McCave, I. N., & Hall, I. R. (2006). Size sorting in marine muds: Processes, pitfalls, and prospects for paleoflow-speed proxies. *Geochemistry, Geophysics, Geosystems*, 7(10). <https://doi.org/10.1029/2006GC001284>
- McKay, R., De Santis, L., Kulhanek, D. K., & Expedition 374 Scientists (Eds.). (2019). Ross Sea West Antarctic Ice Sheet History (Vol. 374). International Ocean Discovery Program. <https://doi.org/10.14379/iodp.proc.374.2019>
- McKay, R. M., De Santis, L., Kulhanek, D. K., Ash, J., Beny, F., Browne, I. M., Cortese, G., Dodd, J. P., Esper, O. M., Gales, J. A., Harwood, D. M., Ishino, S., Keisling, B. A., Kim, S., Kim, S.,

- Kulhanek, D. K., Laberg, J. S., Leckie, M., Mueller, J., ... Xiong, Z. (2018). [No title found]. International Ocean Discovery Program. <https://doi.org/10.14379/iodp.pr.374.2018>
- McKay, R., Naish, T., Powell, R., Barrett, P., Scherer, R., Talarico, F., Kyle, P., Monien, D., Kuhn, G., Jackolski, C., & Williams, T. (2012). Pleistocene variability of Antarctic Ice Sheet extent in the Ross Embayment. *Quaternary Science Reviews*, 34, 93–112. <https://doi.org/10.1016/j.quascirev.2011.12.012>
- Morrison, A. K., Hogg, A. McC., England, M. H., & Spence, P. (2020). Warm Circumpolar Deep Water transport toward Antarctica driven by local dense water export in canyons. *Science Advances*, 6(18), eaav2516. <https://doi.org/10.1126/sciadv.aav2516>
- Muench, R., Padman, L., Gordon, A., & Orsi, A. (2009). A dense water outflow from the Ross Sea, Antarctica: Mixing and the contribution of tides. *Journal of Marine Systems*, 77(4), 369–387. <https://doi.org/10.1016/j.jmarsys.2008.11.003>
- Naish, T., Powell, R., Levy, R., Wilson, G., Scherer, R., Talarico, F., Krissek, L., Niessen, F., Pompilio, M., Wilson, T., Carter, L., DeConto, R., Huybers, P., McKay, R., Pollard, D., Ross, J., Winter, D., Barrett, P., Browne, G., ... Williams, T. (2009). Obliquity-paced Pliocene West Antarctic ice sheet oscillations. *Nature*, 458(7236), 322–328. <https://doi.org/10.1038/nature07867>
- Orsi, A. H. (2002). On the total input of Antarctic waters to the deep ocean: A preliminary estimate from chlorofluorocarbon measurements. *Journal of Geophysical Research*, 107(C8), 3122. <https://doi.org/10.1029/2001JC000976>
- Orsi, A. H., Johnson, G. C., & Bullister, J. L. (1999). Circulation, mixing, and production of Antarctic Bottom Water. *Progress in Oceanography*, 43(1), 55–109. [https://doi.org/10.1016/S0079-6611\(99\)00004-X](https://doi.org/10.1016/S0079-6611(99)00004-X)

- Orsi, A. H., & Wiederwohl, C. L. (2009). A recount of Ross Sea waters. *Deep Sea Research Part II: Topical Studies in Oceanography*, 56(13–14), 778–795. <https://doi.org/10.1016/j.dsr2.2008.10.033>
- Piper, D. J. W., & Normark, W. R. (1983). Turbidite depositional patterns and flow characteristics, Navy Submarine Fan, California Borderland. *Sedimentology*, 30(5), 681–694. <https://doi.org/10.1111/j.1365-3091.1983.tb00702.x>
- Pollard, D., & DeConto, R. M. (2009). Modelling West Antarctic ice sheet growth and collapse through the past five million years. *Nature*, 458(7236), Article 7236. <https://doi.org/10.1038/nature07809>
- Rintoul, S. R. (2018). The global influence of localized dynamics in the Southern Ocean. *Nature*, 558(7709), 209–218. <https://doi.org/10.1038/s41586-018-0182-3>
- Scherer, R. P., Bohaty, S. M., Dunbar, R. B., Esper, O., Flores, J.-A., Gersonde, R., Harwood, D. M., Roberts, A. P., & Taviani, M. (2008). Antarctic records of precession-paced insolation-driven warming during early Pleistocene Marine Isotope Stage 31. *Geophysical Research Letters*, 35(3). <https://doi.org/10.1029/2007GL032254>
- Shadwick, E. H., Tilbrook, B., & Williams, G. D. (2014). Carbonate chemistry in the Mertz Polynya (East Antarctica): Biological and physical modification of dense water outflows and the export of anthropogenic CO<sub>2</sub>. *Journal of Geophysical Research: Oceans*, 119(1), 1–14. <https://doi.org/10.1002/2013JC009286>
- Shapiro, G. I. (2003). Dense water cascading off the continental shelf. *Journal of Geophysical Research*, 108(C12), 3390. <https://doi.org/10.1029/2002JC001610>
- Silvano, A., Foppert, A., Rintoul, S. R., Holland, P. R., Tamura, T., Kimura, N., Castagno, P., Falco, P., Budillon, G., Haumann, F. A., Naveira Garabato, A. C., & Macdonald, A. M. (2020). Recent recovery of Antarctic Bottom Water formation in the Ross Sea driven by climate anomalies. *Nature Geoscience*, 13(12), 780–786. <https://doi.org/10.1038/s41561-020-00655-3>

- Silvano, A., Rintoul, S. R., Peña-Molino, B., Hobbs, W. R., van Wijk, E., Aoki, S., Tamura, T., & Williams, G. D. (2018). Freshening by glacial meltwater enhances melting of ice shelves and reduces formation of Antarctic Bottom Water. *Science Advances*, 4(4), eaap9467. <https://doi.org/10.1126/sciadv.aap9467>
- Straub, K. M., & Mohrig, D. (2008). Quantifying the morphology and growth of levees in aggrading submarine channels. *Journal of Geophysical Research: Earth Surface*, 113(F3). <https://doi.org/10.1029/2007JF000896>
- Thompson, A. F., Speer, K. G., & Schulze Chretien, L. M. (2020). Genesis of the Antarctic Slope Current in West Antarctica. *Geophysical Research Letters*, 47(16), e2020GL087802. <https://doi.org/10.1029/2020GL087802>
- Thompson, A. F., Stewart, A. L., Spence, P., & Heywood, K. J. (2018). The Antarctic Slope Current in a Changing Climate. *Reviews of Geophysics*, 56(4), 741–770. <https://doi.org/10.1029/2018RG000624>
- Warnock, J. P., Reilly, B. T., Raymo, M. E., Weber, M. E., Peck, V., Williams, T., Armbrecht, L., Bailey, I., Brachfeld, S., Du, Z., Fauth, G., García, M. M., Glüder, A., Guitard, M., Gutjahr, M., Hemming, S., Hernández-Almeida, I., Hoem, F. S., Hwang, J.-H., Scherer, R. P. (2022). Latitudinal Variance in the Drivers and Pacing of Warmth During Mid-Pleistocene MIS 31 in the Antarctic Zone of the Southern Ocean. *Paleoceanography and Paleoclimatology*, 37(8), e2021PA004394. <https://doi.org/10.1029/2021PA004394>
- Whitworth III, T., Orsi, A. H., Kim, S.-J., Nowlin Jr., W. D., & Locarnini, R. A. (1998). Water Masses and Mixing Near the Antarctic Slope Front. In *Ocean, Ice, and Atmosphere: Interactions at the Antarctic Continental Margin* (pp. 1–27). American Geophysical Union (AGU). <https://doi.org/10.1029/AR075p0001>
- Williams, G. D., Aoki, S., Jacobs, S. S., Rintoul, S. R., Tamura, T., & Bindoff, N. L. (2010). Antarctic Bottom Water from the Adélie and George V Land coast, East Antarctica (140–

149°E). Journal of Geophysical Research, 115(C4), C04027.  
<https://doi.org/10.1029/2009JC005812>

Yabuki, T., Suga, T., Hanawa, K., Matsuoka, K., Kiwada, H., & Watanabe, T. (2006). Possible source of the antarctic bottom water in the Prydz Bay Region. Journal of Oceanography, 62(5), 649–655. <https://doi.org/10.1007/s10872-006-0083-1>

### **CHAPTER 3: Grain size and compositional characterization of the sedimentary infill of a hydrothermal vent complex in the Vøring Basin, North Atlantic (IODP Hole U1568A): Implications for constraining sedimentary system response to the Paleocene-Eocene Thermal Maximum (PETM)**

Natalia Varela<sup>1</sup>, Brian Romans<sup>1</sup>

<sup>1</sup>Department of Geosciences, Virginia Tech

#### **Abstract**

Hydrothermal vent complexes (HTVC), formed as the result of the interaction between sedimentary rocks and magmatic intrusions, are believed to be the source of a substantial injection of depleted <sup>13</sup>C carbon (12,000 Gt) into the system around ~56 Ma. This significant carbon injection is traced back to the formation of the North Atlantic Igneous Province (NAIP) and is proposed as one of the main contributors to the Paleocene-Eocene Thermal Maximum (PETM).

The Modgunn Arch, situated within the mid-Norwegian margin, North Atlantic, is one of approximately 700 potential HTVC, and one of the drilling sites of International Ocean Discovery Program (IODP) Expedition 396.

This study aims to characterize the sedimentary infill of the Modgunn HTVC and the system response to the PETM, by analyzing the grain size, sorting, and composition of sediments associated with that interval. To achieve that, we analyzed the grain size of 163 sediment samples from Hole U1568A, one of the five holes drilled by IODP Expedition 396, and the closest to the vent axis. Compositional analysis of the crater infill includes microscopic observations of smear slides of fifteen of those samples, and scanning electron microscopy (SEM) imaging in six of them, to assess grain morphology. The sedimentary succession of the HTVC crater is by an average (D50) grain size that goes from fine silt (~6.5 μm) to medium sand (~340 μm). The overall composition is characterized by a by clay, lithic grains, quartz, feldspar, and volcanic glass. The main compositional change in the sequence happens when the biogenic material shifts from being predominantly marine to nonmarine upsection. This change in composition does not exactly match the main shift in grain size, from sandy mud to muddy sand, that represents the boundary between the lithostratigraphic Unit V and the overlying Unit IV (119 mbsf). The grain size distribution also

shows variability within Unit IV. Therefore, we proposed, based on composition and grain size trends, a subdivision of Unit IV into four subunits (from top to bottom: A, B, C, and D), that can be interpreted as changes in the sediment transport energy during the PETM.

The results of the sedimentological analysis of the closest borehole to the HTVC center suggest a delayed response of the sedimentary system while indicating to a quicker response of the biota. The sedimentological variations observed in the crater infill of Hole U1568A could serve as a valuable physical proxy for assessing the sensitivity of the system to changes in climate, such as the response of the hydrological versus the biological systems.

## **17. Introduction**

The Paleocene-Eocene Thermal Maximum (PETM) is the most prominent hyperthermal event of the Cenozoic (Fig. 1). The rapid (<10 kyr) (Kennett & Stott, 1991; McInerney & Wing, 2011) input of vast amounts (>3,000 Gt) (Zeebe et al., 2009) of carbon into the ocean-atmosphere system at ~56 Ma ago, shifted the carbon isotope signal abruptly from -2‰ to -6‰ (Zachos et al., 2007). This negative carbon isotopic excursion (CIE), globally associated with the PETM (McInerney & Wing, 2011), requires the addition of isotopically light carbon sources, such as the dissociation of methane hydrate deposits (Dickens et al., 1995) or methane that originated from volcanic heating of organic-rich sediments (Svensen et al., 2004). The latter mechanism has been proposed based on the occurrence and timing of flood basalt volcanism in the vicinity of the North Atlantic Igneous Province (NAIP) (Storey et al., 2007; Svensen et al., 2004). This input of greenhouse gases caused global surface temperatures to rise up to ~5°C (Kennett & Stott, 1991; J. Zachos et al., 2001; Dunkley Jones et al., 2013), long-term warming (~150-200 kyr) (Röhl et al., 2007; Murphy et al., 2010) shoaling of the deep-sea calcium carbonate compensation (CCD) depth and associated acidification (Zachos et al., 2005), extinction of some marine fauna, and numerous other impacts on the environment (McInerney & Wing, 2011).

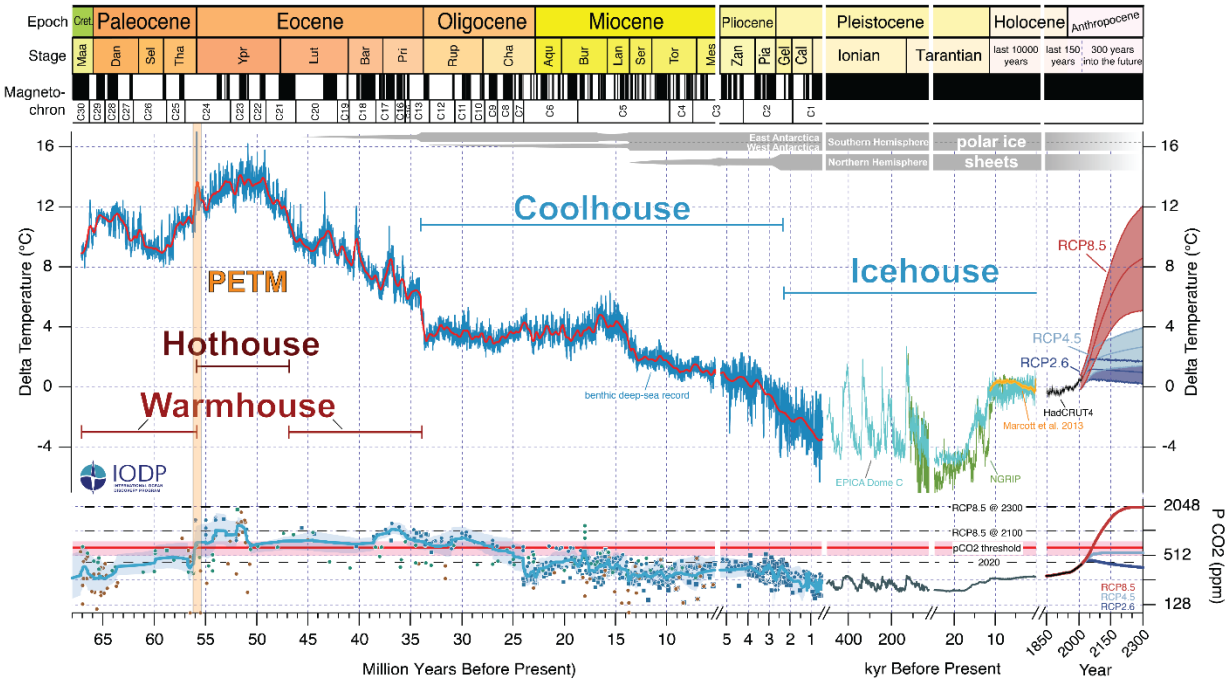


**Figure 1.** Past and future trends in global mean temperature and atmospheric CO<sub>2</sub>. Deep-sea benthic foraminifer oxygen isotope values spanning the last 67 million years are a measure of global temperature and ice volume. The PETM excursion is highlighted here in the orange bar. The future projections for global temperature (Palmer and Harris, 2018) and CO<sub>2</sub> (Meinshausen et al., 2018) for three Representative Concentration Pathways (RCP) scenarios in relation to the benthic deep-sea record. Modified from Westerhold et al. (2020).

One response to the PETM global climate event that has received considerable attention is the hypothesized intensification of the hydrological cycle via an increase of evaporation and precipitation at a global scale (Held & Soden, 2006). At the global scale, the alterations in intensity and seasonality of precipitation enhanced continental silicate weathering rates, one of the main long-term carbon sinks, triggering negative feedback that would have regulated the recovery response of the system after the event (Penman, 2016). At local to regional scales, several studies have investigated the response of source-to-sink sedimentary systems to this global hydroclimatic perturbation (e.g. Schmitz & Pujalte, 2003; Giusberti et al., 2007; John et al., 2008; Pujalte et al., 2015). For example, Foreman et al. (2012) interpreted enhanced transport and deposition of gravel in the Bighorn Basin (Wyoming) fluvial system and Sharman et al. (2023) documented an increase in sediment supply to Gulf of Mexico coastal systems. In addition to interpretations of overall increase in sediment transport in relation to the PETM are questions about system response time. Duller et al. (2019) estimated ~31 kyr lag between PETM onset and observable change in

deposition in northern Spain sedimentary systems. However, there are few studies evaluating the sedimentological characteristics of PETM deposits in settings proximal to the interpreted origin of the carbon release and none that examine the nature of sedimentary deposits within the volcanic system itself.

International Ocean Discovery Program (IODP) Expedition 396, which sailed in August-September 2021, successfully drilled five boreholes in the vicinity of a hydrothermal vent complex (HTVC) in the Modgunn Arch offshore Norway that has been interpreted to be one of the primary sources of PETM carbon release (Planke et al., 2023) (Fig. 2). The objective was to recover sediments deposited during the main phase of NAIP magmatic activity and study its relationship to the PETM. Preliminary bio-magnetostratigraphic and organic carbon isotope data, in addition to seismic stratigraphic information (Berndt et al, 2023), constrain the timing of the latest Paleocene and the PETM interval in the five boreholes. The crater structure of the HTVC indicates rapid formation, followed by undisturbed sedimentation, and limited hydrothermal fluid migration (Berndt et al. 2023). The ~80 m-thick sediment infill of the crater (lithostratigraphic Units V and IV; Fig. 3) was summarized as generally a dark gray to black diatomite with several ash layers indicating active volcanism nearby. Shipboard description of this unique stratigraphic succession (Planke et al. 2023) suggests some variability in the texture and composition of the sediments, but a detailed analysis was not conducted.

This study aims to characterize the sedimentary infill of the Modgunn HTVC and the system response to the PETM, by analyzing the grain size, sorting, and composition of sediments associated within that interval. We focus on the stratigraphic record of the HTVC crater, a potential conduit for the massive organic carbon release responsible for the PETM. Our samples and resultant data come from Hole U1568A (Fig. 3b), which is within the Modgunn HTVC and, thus, most proximal to the suspected site of carbon release. Quantitative grain-size analysis (n=163 samples) is supplemented by visual microscopy (n=15 smear slides) and SEM imaging (n=6 images), all of which is integrated with high-resolution XRF core-scan data. We use these results to examine trends in the Modgunn HTVC crater-infill stratigraphy and discuss implications to understanding sedimentary system response to the PETM climate event.

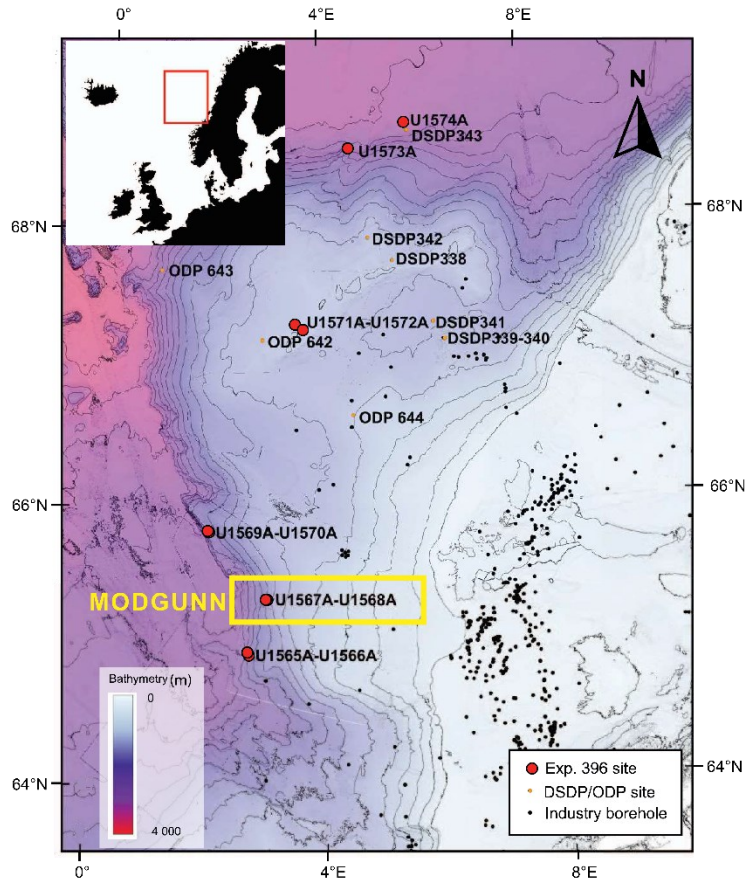
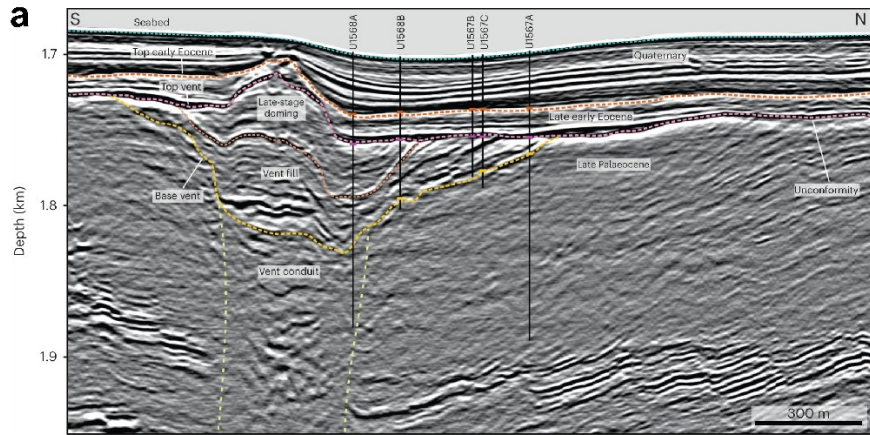


**Figure 2.** Bathymetric map with the location of the Vøring Basin and the IODP Expedition 396 sites (red dots) (after Gernigon et al., 2021 in Planke et al., 2023). The near-vent Modgunn transect (Sites U1567 and U1568) is highlighted with a yellow box. Nearby Deep Sea Drilling Project (DSDP) and Ocean Drilling Project (ODP) are in orange dots, and industry boreholes are shown as black dots. Modified from Planke et al. (2023).



**b** Hole U1568A

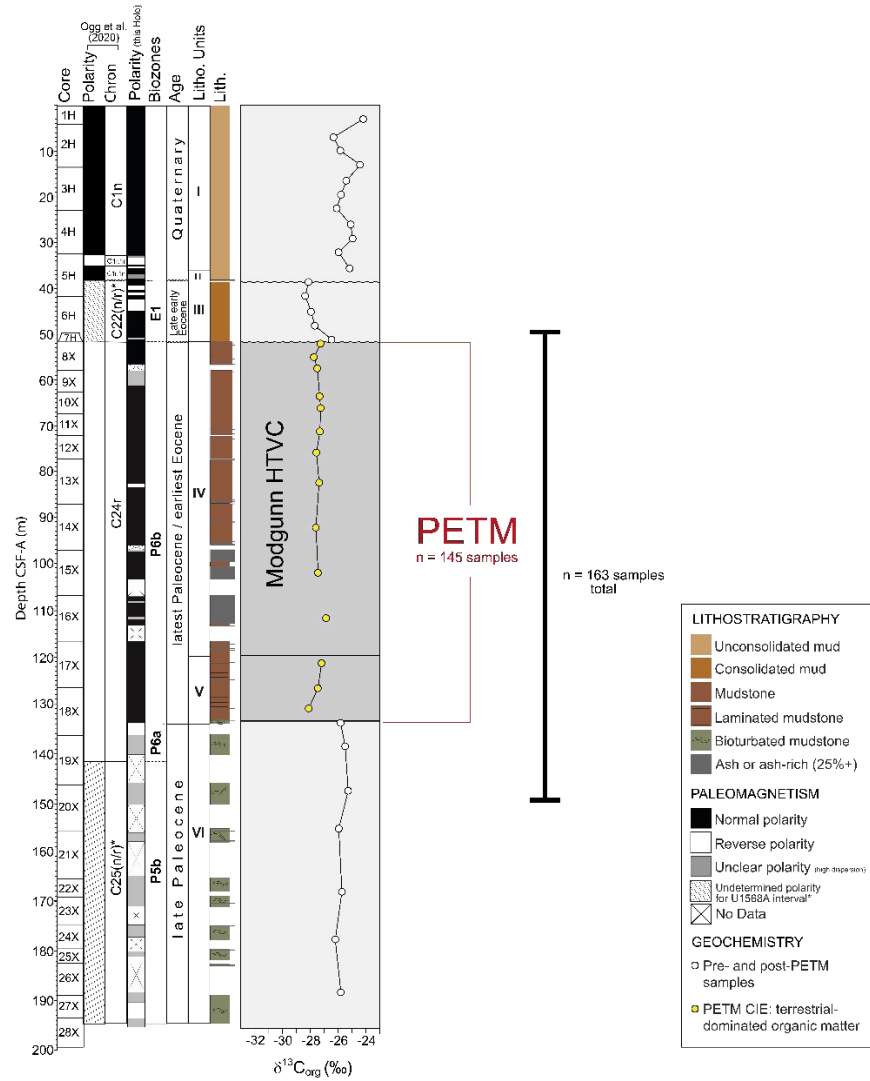


**Figure 3.** (a) Interpreted high-resolution 3D seismic image of the Modgunn Vent showing the location of the five IODP Expedition 396 boreholes (black lines). Colored markers on the boreholes indicate formation tops: orange, top early Eocene; magenta, top vent; dark yellow, top Paleocene; light yellow, approximate vent conduit limit. Seismic data were depth converted, with 1,600 m s<sup>-1</sup> corresponding to the average P-wave velocity measured in the boreholes. Figure and seismic interpretation from Berndt et al. (2023) (b) Lithostratigraphic, magnetic inclination, and  $\delta^{13}\text{C}$  (org) data for Modgunn Hole U1568A with PETM interval in yellow. Note that the shipboard magnetic polarities are in disagreement with the predicted chronostratigraphic and magnetic polarity based on GPTS for the PETM (Ogg, 2020) (the expected reversed polarity for Ch24r is a normal polarity in this transect) therefore, the age model is based on the biozones. Modified from Berndt et al. (2023) and Planke et al. (2023).

---

## 18. Geologic setting

The Modgunn Arch HTVC is located in the Vøring Basin, situated on the Norwegian passive margin in the Norwegian-Greenland Sea (Fig. 2). Following the Caledonian orogeny (390-490 Ma) (e.g. McKerrow et al., 2000), this region underwent intracontinental rifting in the Triassic, followed by the Jurassic oceanic rifting and ultimately the development of the mid-Norwegian passive margin (e.g., Polteau et al., 2020). The Jan Mayen Fracture Zone segments the mid-Norwegian margin, separating it into the Møre and Vøring Margins. These two margins are differentiated by tectonomagmatic characteristics and sediment distribution (Berndt et al., 2001a; Gernigon et al., 2020). Voluminous volcanic activity accompanied the development of the passive margin and rifting (e.g., Wright et al., 2012). Basin opening began ~83 Ma (Campanian) and resulted from extension along three spreading centers: the Kolbeinsey Ridge, the Mohns Ridge, and the Aegir Ridge (Kodaira et al., 1997). Although the first two ridges are still active (Greenhalgh and Kuszniir, 2007), the Aegir Ridge became extinct around 24-21.5 Ma (Uenzelmann-Neben et al., 2017). The ten drill sites chosen for IODP Expedition 396 complement the Ocean Drilling Program (ODP) sites previously drilled in the Vøring Basin in the 1990s (Fig. 2). These new sites, drilled at increasing distance from the Norwegian continental margin, provide access to the Paleogene and PETM sedimentary records as well as the hydrothermal vent complexes (HTVCs) implicated as probable sources of the carbon release. The focus of this study is the Hole from the Modgunn Arch transect most proximal to the HTVC.

The Modgunn Arch transect comprises five boreholes (Holes U1567A, B, and C, and Holes U1568A and B; Fig. 3a) that intersect the upper part of the Modgunn hydrothermal vent complex (HTVC) (Planke et al., 2023). The vent complex is truncated by an erosional unconformity of early Eocene age and overlain by 20 to 50 m of Eocene to recent sediments. The vent includes a feeder system and a crater at the paleoseafloor. The crater was rapidly infilled during the PETM,

presenting an expanded section that consists of diatom-bearing mudstones, ash layers, and deposits containing terrigenous material characterized here in detail.

## **19. Study Approach**

### *19.1. HTVC formation, timing, and morphology*

The Modgunn Arch hydrothermal vent complex (HTVC) is characterized by a vertical feeder system measuring around 400 meters in depth and 200 to 240 meters in width. This system extends from a complex of sills located at the base, reaching up to a seafloor crater with a funnel-like shape at the top (Berndt et al., 2023). According to exploration 3D seismic-reflection data (Fig. 3a), the sill complex comprises multiple interconnected intrusions, with a lateral extent of at least 5 kilometers and likely to be several tens of meters thick, as indicated by their high seismic amplitudes (Berndt et al., 2023).

The Modgunn HTVC is positioned on the upper boundary of the sill. The upper unconformity cuts off the inclined reflections in the top section of the hydrothermal vent complex. Located directly above the pipe structure in the axis of the depression, the reflections curve upwards, creating a mounded morphology. The mound is covered by draping and onlapping reflections that extend towards the seafloor (Fig. 3a).

The sedimentary fill of the vent crater indicates a conformable stratigraphic succession with little to no hydrothermal fluid migration, implying that HTVC was no longer active during deposition of the crater infill (Berndt et al., 2023). The high-resolution C-isotope curve from the Modgunn Hole U1567C places the CIE onset 11–15 m above the vent base, suggesting, due to the high sedimentation rate and thickness of the ash layers, that the vent formed probably only a few millennia before the PETM onset (Berndt et al., 2023) (Fig. 3). Thus, the vent formed before the onset of the PETM, and was refilled during the onset and body of the Carbon Isotope Excursion (CIE). However, this early infill is not present in U1568A, Modgunn's hole closest to the center of the vent, studied here. A potential explanation would be the ongoing hydrothermal at the time, or slumping (Berndt et al., 2023).

According to shipboard data (Planke et al., 2023) and Berndt et al. (2023), the vent infill is composed of two lithostratigraphic Units (IV and V; Fig. 3) consisting mostly of very dark gray to

black diatomite (the units are described in more detail in section 3.2). Throughout the two units, there are widespread ash layers, indicating the frequent presence of nearby explosive volcanism on land or in shallow-water environments during this time period, which has been observed in other deposits with similar age in the NAIP area (Eldholm et al., 1989; Laberg et al., 2005a; Stokke et al., 2020; Berndt et al., 2023).

The recovery phase of the CIE appears to be absent at the Modgunn sites (Fig. 3b), indicating that the vent formation occurred just before the onset of the PETM-CIE and that the crater infill occurred throughout the latest Paleocene and earliest phases of the PETM. The erosional unconformity that forms the top of the vent infill is overlain by lithostratigraphic Unit III, which consists of dark grey to brownish mudstones with occurrences of specific dinocyst taxa (more details in section 3.3), indicating a middle early Eocene age for the sediments onlapping onto the dome structure (Berndt et al., 2023).

### *19.2. IODP Hole U1568A and lithostratigraphic units*

Hole U1568A (65°21.5942'N, 3°3.1091'E) is one of two holes at Site U1568, and the one closest to the HTVC axis along the Modgunn transect (Fig. 3a). It lies at a water depth of 1707.4 meters below sea level (mbsl) and it was drilled up to 200 meters below the seafloor (mbsf), with core recovery of 78.3% (156 meters). The hole comprises a total of 28 cores (9.5 m each), using advanced piston coring (APC) for the upper seven cores, whereas the deeper section was drilled utilizing the extended core barrel system (XCB) (Planke et al. 2023).

The stratigraphic succession recovered at the Modgunn transect was divided into six lithostratigraphic units, all of them recognized in all the holes including U1568A, but with variations of their thicknesses (in Planke et al., 2023). From top to bottom (Fig 3.b):

- Unit I is gray clay with rare isolated outsized clasts.
- Unit II consists of dark brownish-gray sediments (clay- to centimeter-scale nodules) rich in manganese and iron in the uppermost interval and light yellowish-brown sand-rich clay throughout.
- Unit III is pale yellow to very dark greenish-gray clay with silt, including clasts of clay and rare beds of siltstone.

- Unit IV is dark greenish gray to very dark gray claystone to siltstone, with common volcanic ash beds and light bioturbation.
- Unit V is very dark gray to black parallel laminated claystone with common volcanic ash and lacking bioturbation.
- Unit VI is very dark greenish-gray clay- to siltstone with moderate bioturbation

We focus on Units IV and V because these are the units determined to include the PETM interval by Berndt et al. (2023), the chronological constraints for which are summarized in the next section.

### *19.3. Chronology, isotope stratigraphy, and sedimentation rate of Hole U1568*

Based on shipboard bio-magnetostratigraphic data (Planke et al., 2023) and subsequent post-expedition analysis (Planke et al., 2023; Berndt et al., 2023) (Fig. 3b), Units I and II represent the Quaternary and are separated from the underlying strata by a significant unconformity (the base of Unit II is Pleistocene and the top of Unit III is Late Early Eocene; Planke et al. 2023). Iron-manganese nodules are common near this boundary, suggesting a large gap in deposition (Planke et al. 2023). In contrast, the unconformity between Units III and IV is relatively shorter (< 6 million years in duration) and varies among the five boreholes. The deeper Units IV and V are determined to be latest Paleocene to earliest Eocene based on the presence of *Apectodinium augustum*, a dinocyst taxon that serves as an indicator of the PETM, along with the diatom *Hemiaulus proteus*, providing additional evidence (Berndt et al., 2023; Planke et al, 2023).

The organic carbon isotope excursion (CIE) associated with the PETM occurs at 133.26 mbsf as a step change from  $\sim -26\text{‰}$  to more  $^{13}\text{C}$ -depleted values (less than  $-28\text{‰}$ ) (Berndt et al., 2023) (Fig. 3b). The first recorded CIE sample at Hole U1568A consists of marine-dominated organic matter and is much more  $^{13}\text{C}$ -depleted than subsequent values (i.e., less than  $-31\text{‰}$ ). The organic composition shifts abruptly above this sample from marine to terrestrial-dominated, which coincides with increasing CIE values (i.e., from less than  $-31\text{‰}$  up to  $\sim -28\text{‰}$ ). Consequently, the variability within all the depleted CIE samples reflects variability of the organic composition and Units V and IV most likely correspond to the main body CIE (Berndt et al., 2023). The CIE onset corresponds to the Unit VI to Unit V boundary and the PETM is confirmed by the presence of *Apectodinium augustum* (Planke et al., 2023). The last occurrence of common *Apectodinium*

augustum roughly corresponds to the end of the main body (or “core”) of the PETM CIE (Frieling et al., 2016). Therefore, Units V and IV represent main body terrestrial-dominated organic  $\delta^{13}\text{C}$  CIE values which are sustained for nearly 80 m (Fig. 3b). The main body CIE is interpreted to have lasted  $\sim 50$  kyr (Zeebe, 2013), which corresponds to an average sedimentation rate of 1.6 m/kyr for Units V and IV. This value represents a minimum sedimentation rate as the top of Unit IV is marked by an unconformity, suggesting the main body CIE is incomplete (i.e., there is no transition to  $\delta^{13}\text{C}$  recovery values). These very high sedimentation rates reflect the rapid influx of material associated with the infilling of the cratered vent complex following the PETM onset and during the main phase of the PETM events.

#### 19.4. *Methods for characterization*

The characterization of the PETM interval in Units IV and V in Hole U1568A, part of the crater infilling of the HTVC during the latest Paleocene/earliest Eocene, is based on a combination of new data from sediment samples reported here, shipboard and post-expedition data accessible to IODP Exp 396 participating scientists, and recently published data (Berndt et al., 2023). Shipboard core description and biostratigraphic data (Planke et al., 2023) provide generalized lithologic context and chronologic control, respectively. X-ray fluorescence (XRF) core scanning data (publicly available at the IODP Laboratory Information Management System [LIMS] website) provide elemental ratios useful for bulk sediment composition determination. XRF data was collected at the IODP Gulf Coast repository (Texas A&M facilities, College Station, Texas), at a resolution of 3 cm, and at a 30 kV, which provides data for trace elements such as Zr. The  $\delta^{13}\text{C}$  data from Berndt et al. (2023) confirms the presence of the CIE and the PETM interval. The methods for the new data reported here, which includes quantitative grain size analysis and visual microscopy of sediment samples from Hole U1568A, are described in detail below.

##### 19.4.1. *Grain-size analysis of the PETM interval*

The sampling plan was centered on the PETM event recognized in Hole U1568A through shipboard biostratigraphy (Planke et al. 2023) and confirmed by carbon isotope analysis reported in Berndt et al. (2023) summarized above. The sampled section includes, from oldest to youngest: pre-PETM (Late Paleocene; upper section Unit VI), PETM (latest Paleocene/earliest Eocene, Units V and IV) and post-PETM (Late early Eocene; lower section Unit III) strata (Fig. 3). As stated

above, Units IV and V are the focus for this work as they represent the crater infilling of the HTVC during the climatic event (Berndt et al., 2023).

The samples for this study were collected by the Expedition 396 science party at the MARUM Bremen Core repository during the sampling party (April 21-28, 2022). To ensure the coverage of the lithological variations within the targeted interval (from 50.5 to 149.5 mbsf), samples were taken every 50 cm using a 20 cm<sup>3</sup> half-round plastic scoop, yielding a total of 163 samples from Hole U1568A for grain size analysis (Fig. 3b).

We characterized the bulk grain size, instead of isolating a specific fraction (e.g., terrigenous), because of the unique and understudied nature of this HTVC depositional setting. To characterize the bulk grain size distribution, we used a Malvern MasterSizer 3000 laser particle analyzer, which captures 0.01-3500  $\mu\text{m}$  size range. Before the measurement, we physically disaggregated the sediment using a wooden mortar and pestle to avoid over-grinding. Next, we subsampled  $\sim 2.5$  g per sample, which was dispersed in 30 ml of a 0.5% sodium hexametaphosphate solution [(Na-PO<sub>3</sub>)<sub>6</sub>] to aid deflocculation of clay. The solution was left to settle in a centrifuge tube for at least 48 hrs.

Due to the large range of particle sizes in the bulk samples, including a substantial  $>63$   $\mu\text{m}$  fraction, we modified the standard pipetting approach. Although all samples were dispersed in a solution, the larger clasts can settle too fast and the pipette was unable to retrieve them. Instead, we homogenized the samples and then let them settle in its centrifuge tube. To obtain the subsample to be measured in the MasterSizer 3000, we used an elongated spatula to “cut through” the sample all the way down to the bottom of the centrifuge tube, while making sure that the now-settled grains were sampled together. The resultant  $< 0.5$  g subsample was then poured into a smaller beaker with distilled water, and homogenized again.

We manually poured the sediment into the wet dispersion chamber until it reached  $\sim 8$ -10% of obscuration. The dispersed sample was sonicated for 60 seconds and then measured three times using the instrument sequence. The sonication would, in certain cases, increase the obscuration rate, but within acceptable instrumental limits (below 20%).

Out of 163 total samples, 103 (63%) have replicates, consisting of two representative subsamples measured individually with the same instrument sequence. The remaining 60 samples were

duplicated, running the instrument sequence twice on each sample to ensure consistent averages. We processed the output data using Gradistat version 9.1 (Blott & Pye, 2001) and calculated the median (50th percentile; D50), 90th percentile (D90) from the distributions, and sorting categories (Folk & Ward, 1957). The results are displayed in volume percentage.

#### *19.4.2. Visual microscopy and SEM imaging*

To characterize the composition of sediment constituents and their relative abundance in the stratigraphic succession, we subsampled from a representative subset of the bulk grain-size samples for visual (smear slide) microscopy and scanning electron microscope (SEM) imaging.

We selected the smear slides samples ( $n = 15$ ) based on their lithological representativity within the interval of interest, and, as a second criteria, per each core within that same interval. The samples that had a D50 within fine silt to fine sand (8-250  $\mu\text{m}$ ), were directly mounted in a microscope slide. We scrapped off a small amount of sediment from the main sample, spread it in the microscope slides, and dried them in a 50°C oven for ~10-15 minutes. Once dried, we added a drop of the UV-activated adhesive on top, and covered the sample with a 18 mm x 18mm slide cover and pressed it slightly to allow the adhesive to expand. We then put the smear slides under a UV light (48W), for a total of 5 minutes each.

Six out of the 15 selected smear slide samples with a D50 > 250  $\mu\text{m}$  (medium sand and coarser) were wet sieved at 63  $\mu\text{m}$ . The coarse fraction (>63  $\mu\text{m}$ ) was analyzed using scanning electron microscopy (SEM). The <63  $\mu\text{m}$  fraction was analyzed using the smear slide method described above.

Following general procedures of Marsaglia and Milliken (2023), we determined the relative abundance of the different components present in the smear slides by focusing on one specific magnification (10x) and then visually estimating the percentages. Results are reported and displayed visually as “present” (P; 0%-5%), “few” (F, 5%-10%), “common” (C; 10% - 25%), “abundant” (A; 25%-50%), and “very abundant” (VA; >50%). This approach is semi-quantitative and typically used to highlight the presence/absence of constituent grains and overall stratigraphic trends in relative abundance.

## 20. Results

### 20.1. Bulk grain size

The overall grain size distribution of Hole U1568A shows a broad range across the 163 samples and ~100 m of stratigraphy. The median particle size (D50; Fig. 4b) spans from very fine silt (~6.5  $\mu\text{m}$ ) to medium sand (~340  $\mu\text{m}$ ), whereas the coarser end of the distribution (D90, Fig. 4c) ranges from very coarse silt (~32  $\mu\text{m}$ ) up to coarse sand (~980  $\mu\text{m}$ ). The most notable and stratigraphically abrupt change occurs at ~119 mbsf (within Core 17X), where the D50 transitions up core from coarse silt (D50 ~35  $\mu\text{m}$ ) to very fine- to upper fine sand (~90-250  $\mu\text{m}$ ). This abrupt coarsening coincides with the top of lithostratigraphic Unit V, and therefore, after the onset of the PETM interval (Planke et al., 2023, Berndt et al., 2023).

The median grain size (D50) decreases upcore between 90.5 to 77 mbsf narrowing the range to very fine to fine sand. Up section, the grain size variability in Unit IV increases again, fluctuating between very fine up to medium sand. At ~65 mbsf, the grain size (D50 and D90) starts to steadily decrease, to increase again relatively abruptly between 54 to 59.5 mbsf, reaching up to medium sand, followed by a decrease to fine sand in the uppermost few meters of Unit IV. This is followed by a new decrease in the lower section of Unit III (Fig. 4).

Sorting ranges from poorly sorted to very poorly sorted throughout the studied interval with no overall stratigraphic trend (Fig. 4d). The highest sorting values (i.e., most poorly sorted) corresponds with the interval directly overlying the abrupt coarsening transition at ~119 mbsf. Except for a single data point at ~73 mbsf, the lowest sorting values (i.e., most well sorted, relatively) occur in the 54-59.5 mbsf interval near the top of Unit IV.

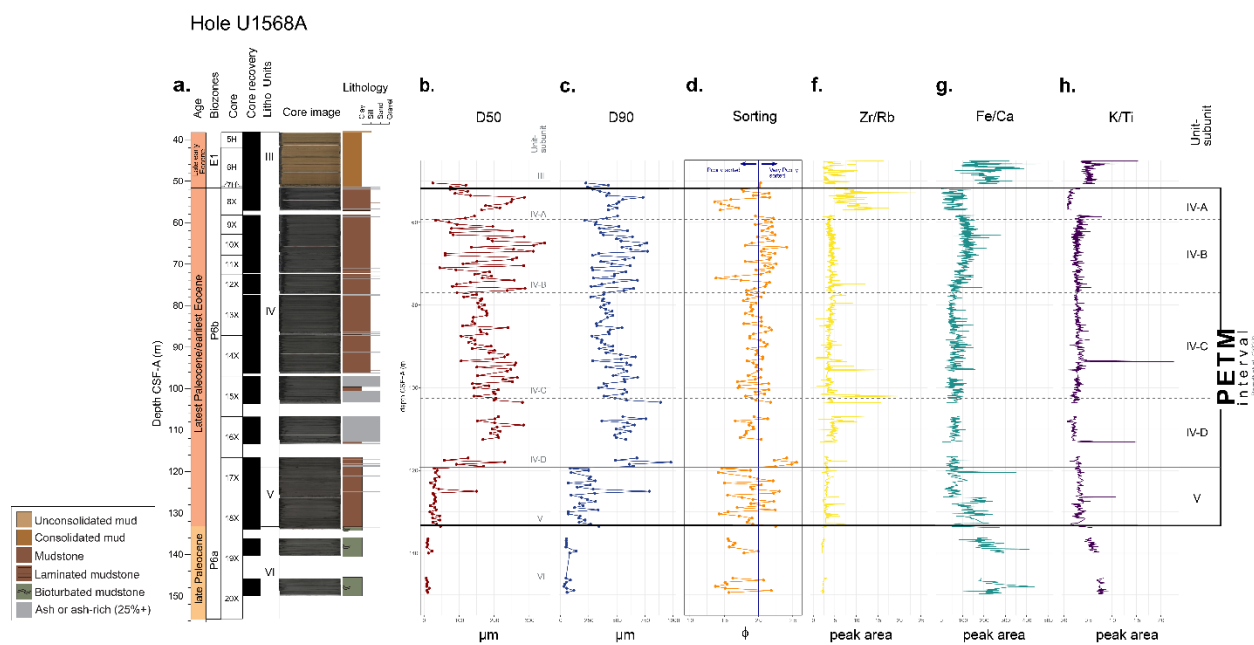


**Figure 4.** Stratigraphic context for IODP Hole U1568A (CSF-A in meters; modified from Planke et al., 2023), plus bulk grain size results (this study; a and b columns) and XRF calculated ratios (c, d and f columns). The PETM interval is indicated by the black lines. Grain size analysis of 163 samples before, during and after the PETM is characterized by the D50 (a) and D90 (b) percentiles (in  $\mu\text{m}$ ).

## 20.2. Grain composition and relative abundance

The smear slide analysis and SEM imaging aids in characterization of the sediment composition and grain morphology of the crater infill succession captured in Hole U1568A. The smear slide results shown in Figures 5 and 6 emphasize the compositional constituents that could be identified consistently throughout the interval and are grouped by general grain type (i.e., siliciclastic, detrital carbonate, and biogenic). In general, the clay fraction is present throughout the  $\sim 100$  m thick interval as a common to very abundant grain type. Intervals with the highest abundance of clay are the two lowermost Units (VI and V) and within Unit IV from  $\sim 70$  to 110 mbsf. Lithic grains are the second-most abundant group, after clay, and present throughout the entire succession. In polarized light they are dark brown or black, but in incident light, the fine-grained material appears to be mudstone/siltstone grains, clay aggregates or, in the case of some of the samples (e.g. sample X396\_U1568A\_10X\_2\_18, Fig. 6c), tephra material. Grains of minerals like quartz and feldspar are present in the silt to sand range, with feldspar slightly more common than quartz in some intervals (Fig. 6b). The abundance of volcanic glass (Figs. 6a, 6d) can be linked to the identified

ash layers, as seen in the samples X396\_U1568A\_15X\_3\_100 and X396\_U1568A\_16 X\_2\_18 taken between 100 to 110 mbsf. On the sample from Core 15X, no biogenic grains were identified.

The most prominent stratigraphic change in the smear slide data is observed from the relatively high abundance of marine biogenic material (Fig. 6f) in the lower Units (V and VI) that decreases slightly in the uppermost parts of Unit V, followed by a significant decrease in overlying Unit IV and the presence of more terrestrial-dominated biogenic material (e.g., pollen, plant debris, etc.; Fig. 6e). This change from marine to more terrestrial biogenic constituents does not match exactly the observed grain-size coarsening (Fig. 5). The content of undifferentiated organic debris increases, overall, upward through the succession. The detrital carbonate content is scarce overall, but notably more common in the uppermost part of Unit IV.

Scanning electron microscopy (SEM) imaging was used to aid in the morphological characterization of the  $>63 \mu\text{m}$  grains within six samples. In addition, we ran an elemental analysis (EA) using the available energy dispersive x-ray spectroscopy (EDS). The resulting elemental maps and XR spectrums did not yield additional compositional information, beyond what was registered in the visual analysis. However, it further confirmed some of the observations (e.g., the red color in some of the grains, hinting at Fe-oxides, was validated by the EA). The overall “poor” to “very poor” sorting given by the grain size analysis for the bulk sample was also evident even in the coarser fraction observed in the SEM images (Figs. 6g, 6h). In these samples, the grains were mostly angular to subrounded, with medium to low sphericity.

Hole U1568A

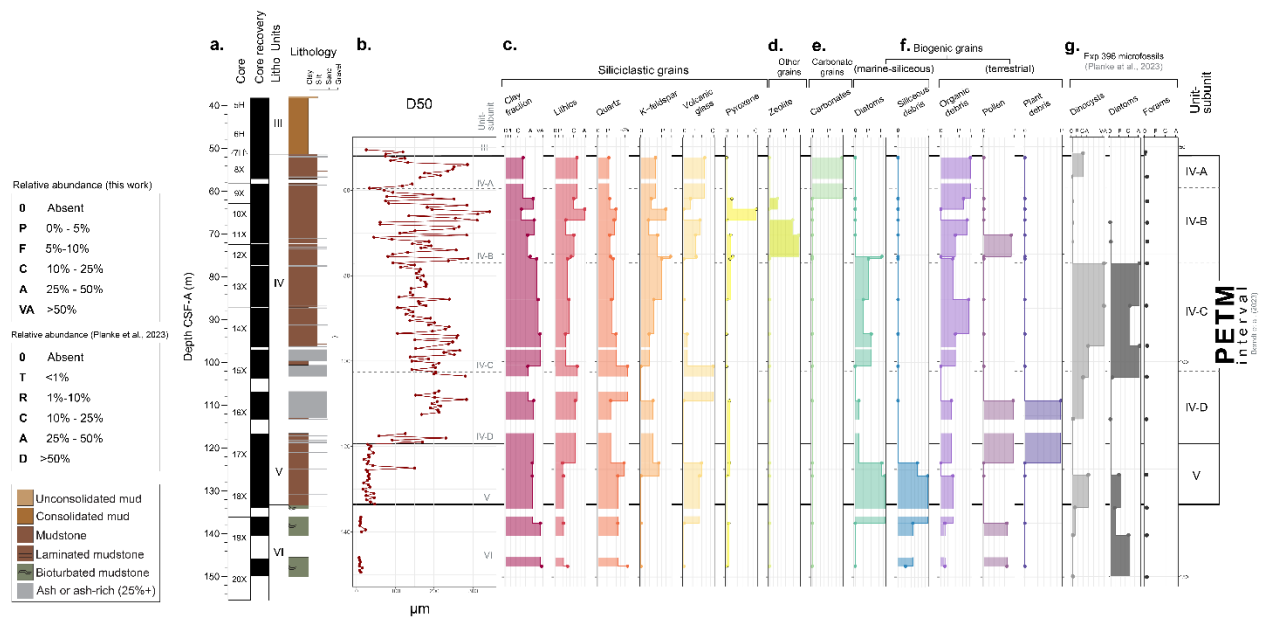


**Figure 5.** (a) Stratigraphic context for IODP Hole U1568A (CSF-A in meters; modified from Planke et al., 2023). (b) Bulk grain size analysis of 163 samples before, during, and after the PETM is characterized by the D50 percentile (in  $\mu\text{m}$ ) (this study). The smear slide compositional analysis of 15 samples is represented here by the relative abundance of the different grain types: (c) siliciclastic, (d) other grains, (e) carbonates, and (f) biogenic. (g) Exp. 396 microfossils column shows the relative abundances of major microfossil groups for Hole U1568A in Planke et al. (2023) (relative abundance scale in the legend). The thickest black lines indicate the PETM interval (Berndt et al., 2023), and the lithostratigraphic unit boundary between units V and IV is a solid black line. The boundaries for the subunits of Unit IV defined in this study are in dashed grey lines.

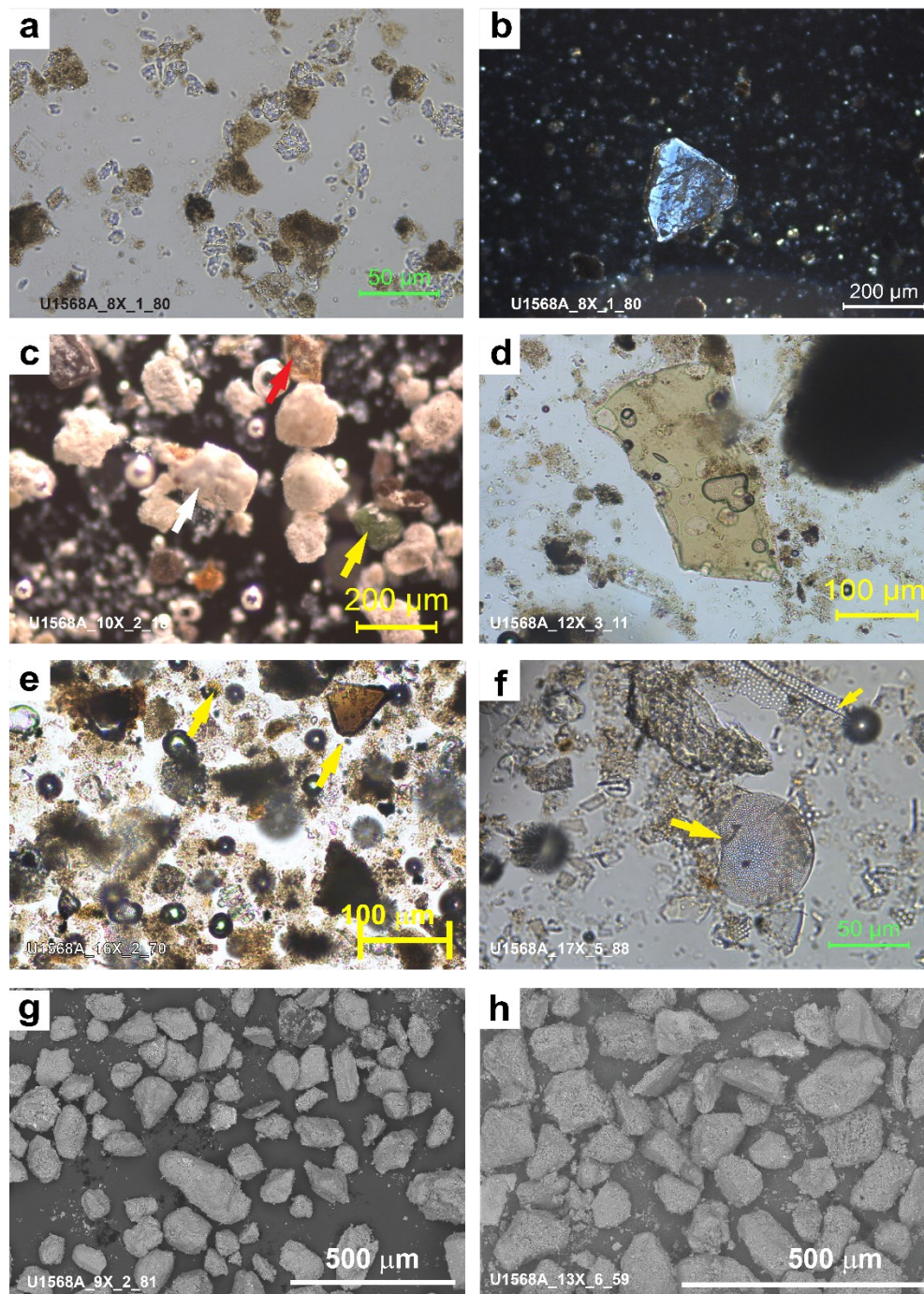


**Figure 6.** Microphotographs of some of the main components identified in the smear slides analysis and SEM images. The sample name is on the lower left corner. (a) Subunit IV-A . Plane polarized light (PPL) image of the bulk sediment sample. Brown grains are organic debris, and the transparent grains are volcanic glass. (b) Subunit IV-A. Feldspar grain in cross-polarized light, with some clay alteration. (c) Subunit IV-B. Lithic volcaniclastic grains (tephra) in incident light. The white arrow shows the most common occurrence, and the red arrow points to Fe-oxide rich clasts. A grain of glauconite is shown with a yellow arrow. (d) Subunit IV-B. Large (~200  $\mu$ m) vesicular volcanic glass with a light brown tint in PPL. (e) Subunit IV-D. PPL image of the bulk sample. This is one of the first ones (core 16X) to show the increase in terrestrial content versus the more marine underlying units. The yellow arrows point a spores (right) and some derived material. (f) Unit V. The PPL of the bulk sample shows the abundance of marine material,

specifically diatoms (yellow arrows). SEM images showing grain morphology of the >63  $\mu\text{m}$  fraction from samples from subunits IV-B (g) and IV-C (h). Overall, the grain morphology ranges from angular to subrounded shapes, with poor to very poor sorting.

---

### 20.3. *Comparison with the XRF ratios*

Utilizing publicly accessible XRF data obtained from core scans of Hole U1568A, we conducted a comparative analysis of three XRF ratios alongside the grain size and smear slide/compositional data (Fig. 4). The primary objective was to discern sedimentation patterns associated with hydrothermal activity and identify evidence of changes in the hydrological cycle during the PETM. The Zr/Rb ratio is commonly used as a proxy for grain size (Dypvik & Harris, 2001; Liu et al., 2002; Rothwell & Croudace, 2015; Wu et al., 2020). Zirconium (Zr) predominantly resides in coarser grain sizes, while Rb is concentrated in clays (Rothwell & Croudace, 2015). The data for Hole U1568A exhibits a relatively consistent trend throughout the studied interval until approximately 59 m, with a few discernible higher peaks (Fig. 4f). Beyond this point and up to around 51.5 m (the upper limit of Unit IV), the increase in Zr/Rb aligns with the pattern of grain size increase, mirroring the trends observed in the other XRF ratios.

The Fe/Ca ratio is a useful indicator for detecting changes in the delivery of terrigenous sediment, used to quantify terrigenous fluxes versus marine carbonate proportions (Rothwell & Croudace, 2015). In U1568A, the upper section of Unit VI exhibits a higher Fe/Ca intensity when compared to the overlying Unit V, gradually declining until approximately 126 m, where it stabilizes. Subsequently, it maintains a consistent intensity trend until  $\sim 77$  m, where an increase in the Fe/Ca ratio aligns with higher variability in grain size (Fig. 4b). This suggests an increase in the proportion of terrigenous material, supported by the rise in organic debris (Fig. 4f). The most prominent correlation occurs in the uppermost 8 meters, where a transition to a lower Fe/Ca ratio corresponds with shifts in the patterns of the other two XRF ratios (Figs. 4f, 4h), including the higher relative abundance of carbonate grains in the smear slides (Fig. 5e).

The K/Ti ratio offers a qualitative assessment of weathering and erosion intensity (Piva et al., 2008; Rothwell & Croudace, 2015). Potassium (K) is associated with K-Feldspar and terrestrial siliciclastics, where a higher content in fine-grained sediment can be correlated with a high illite content (potassium mica) (Rothwell & Croudace, 2015). Titanium (Ti) is typically concentrated in

coarse-grained sediment, characterizing the detrital component. Since it is redox-insensitive, it is less prone to be integrated into other authigenic minerals, unlike Fe (Rothwell & Croudace, 2015). In Unit VI, the higher K/Ti ratio (Fig. 4h) can be attributed to increased clay content, which decreases in the overlying Unit V, without noticeable shifts until around 77 m. The slight increase in variability above 77 m and until around 59 m may indicate a rise in terrigenous material. This is followed by a sharp drop in the upper 8 meters of Unit IV, which aligns with the patterns observed in other XRF ratios, representing a significant increase in grain size and a higher influx of terrigenous sediment.

## **21. Discussion**

### *21.1. Sedimentary infill of a marine hydrothermal vent complex environment*

Studies focused on the characteristics of the sedimentary infill of hydrothermal vent complexes (HTVCs) are relatively rare (Svensen et al., 2006) and especially with an emphasis on the passive infill phase that follows active hydrothermal venting. Moreover, the majority of existing studies are based on seismic-reflection data with sparse borehole information and very few with stratigraphically continuous core (e.g., ODP Eldholm et al. (1989); DSDP; Talwani et al.(1976) sites; Fig 1). The grain size, sorting, and compositional data from the Modgunn Arch -PETM section reported in this study therefore provides fundamental sedimentological information required to better understand the stratigraphic evolution of a unique and rarely studied depositional setting.

Our results allow for a refinement of the existing lithostratigraphic framework for Hole U1568A (Fig. 7). For example, the recent overview by Berndt et al. (2023) refers to the lithologies in Units IV and V as “mudstone”, yet our grain-size data clearly show that Unit IV contains significant amounts of sand-sized material (Fig. 4). Based on our results, the lithology of Unit V is more accurately classified as sandy mud and Unit IV as dominantly muddy sand (with minor amounts of sandy mud and slightly gravelly muddy sand). Additionally, both the sorting (poorly sorted to very poorly sorted, Fig. 4d) and the smear-slide results, which show that terrigenous clay and lithics are present throughout, reveal this depositional succession to be a highly variable mixture of material.

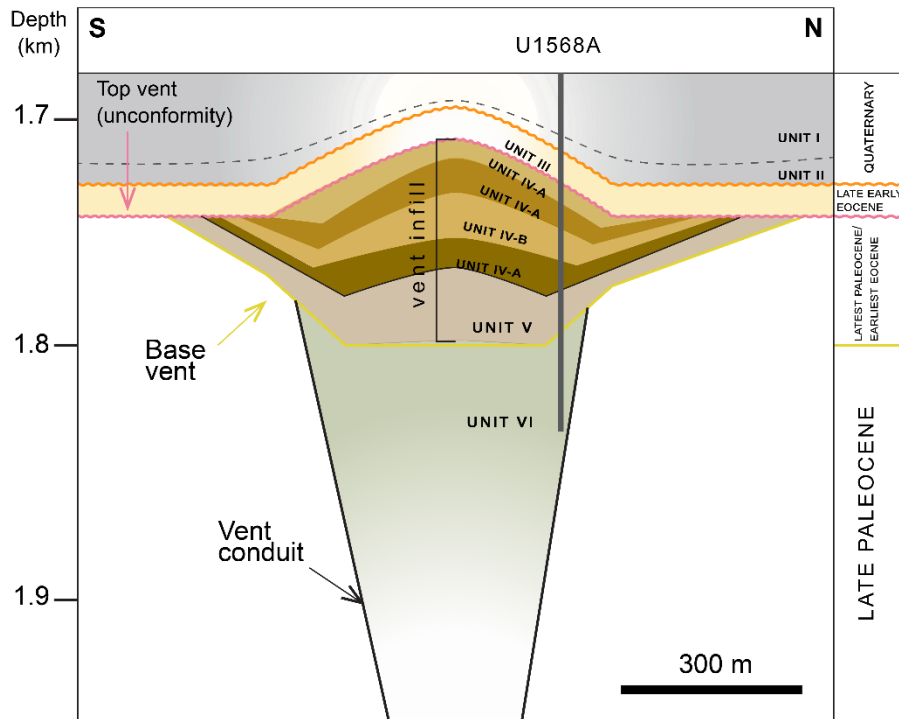


**Figure 7.** Schematic drawing of the Modgunn hydrothermal vent and the distribution of the lithostratigraphic units, including the subunits of Unit IV (this study). The vertical depth scale (km) is approximated, based on the seismic line interpretation of Berndt et al. (2023). The gray line shows the position of Hole U1568A. The age on the left shows the main bounds of the vent (base: yellow line; top vent (and stratigraphic unconformity): pink wavy line) and the main stratigraphic unconformity between Late early Eocene and the Quaternary deposits (orange wavy line).

From the bottom up, Unit VI has a predominantly fine silt grain size, and shows a lack of volcanic-related grains (e.g., volcanic glass, k-feldspar, pyroxene, etc.). The biogenic material, marine and terrestrial, even if present, is quite scarce (<5%). The bioturbation observed in these deposits (Planke et al., 2023) implies a mixing of material, reflected in the poorly sorted mud classification for this Unit. Therefore, the combination of terrestrial and marine-derived grains might not accurately reflect the in-situ deposition, due to the particle reworking.

Unit V has a higher abundance of marine biogenic sediment (i.e., diatoms and other biosiliceous debris) in the lower portion compared to underlying Unit VI, yet it also contains siliciclastic material that is observed throughout the entire succession, indicating that it is not a pure diatomite. The combination of marine biogenic and siliciclastic grains indicates a mixture of in-situ and transported material. The poorly to very poorly sorted sorting, and the angularity of the grains, however, points to a relatively short transport from the source. The land-derived material is more

abundant in the upper third of Unit V, a change in sediment composition that not coeval by the change in grain size (except for the peak at ~125 m).

Unit IV is distinguished from underlying Unit V by the abrupt and significant increase in the abundance and grain size (from the “sandy mud” to the “muddy sand” classification, following Blott and Pye (2001). This significant coarsening, with grains  $>500\ \mu\text{m}$ , suggests an overall marked increase in transport energy. Based on the trends in grain size and the presence/ absence of certain components observed in the smear slides, we propose a further subdivision of Unit IV in four subunits: A, B, C and D (Table 1).

**Table 1:** Sedimentological characterization of Unit IV subunits

SUBUNIT	Top depth (m)	Bottom depth (m)	Total thickness (m)	Grain size range (min-max D50; $\mu\text{m}$ )	Mean D50 ( $\mu\text{m}$ )	Grain size trend (from bottom to top of each subunit)	General lithological description	Sediment transport regime
IV-A	51.45	59.5	8.1	33.5-285.9	163.6	Gradual increase	Carbonate -rich muddy sand Unit with high terrigenous content	Transport energy increase
IV-B	59.5	77	17.5	44.9-343.4	173.1	Gradual increase	Muddy sand with high terrigenous content and ash layers	Transport energy increase
IV-C	77	102.1	25	105.8- 265.9	176.3	Gradual decrease	Muddy sand with some ash layers and marine biogenic grains (diatoms)	Transport energy decrease
IV-D	102.1	119.19	17.1	58.1- 283.5	190.6	No noticeable increase-decrease	Mostly ash layers with land-derived material	Ash fall deposits with transported material

From the bottom up, Unit IV-D (17.1 m thick) has a higher ash content than the rest of the sequence (>25% or more according to shipboard descriptions; Planke et al., 2023). Its composition reveals some terrestrial material that would have been transported along with the deposition of ash fall deposits (volcanic glass in Fig 5.b). The Zr/Rb peaks (Fig. 4c) can be interpreted as evidence of the latter (Westerhold et al., 2009; Rothwell & Croudace, 2015).

Unit IV-C (25 m thick) shows a gradual decrease in grain size up section, along with an increase on mostly fragmented diatom content (“present” in the abundancy classification, between 1% to 5%). The increase in marine material with a decrease in distinctively non marine/terrestrial groups, could be attributed to a weaker energy transport system, including surface ocean currents.

Unit IV- B (17.5 m thick) shows the largest grain size variability (D50 from 44.9-343.4  $\mu\text{m}$ ) and an overall gradual increase towards the top. The lack of marine-derived material (Fig. 5f), with a slight increase in the terrestrial signal, implies an increase in the transport energy of the system, bringing more land-derived material into the HTCVC. The increase in peak intensity of the Fe/Ca ratio supports an interpretation of higher terrigenous input (Rothwell & Croudace, 2015). In addition to the terrestrial biogenic components, there is a rise in volcanic elements (volcanic glass, pyroxenes) matching the described ash layers in the lower third of this subunit (Fig. 5c). The increase in the intensity range for the K/Ti ratio (Fig. 4f) might indicate the formation of authigenic minerals like the zeolite (phillipsite) (Fig. 5c)

Unit IV-A (8.1 m thick) gradually increases its grain size, supported by higher Zr/Rb ratio values (Fig. 4f), along with a higher terrigenous input (lower K/Ti), which is also observed as higher organic debris content (Fig. 5f). The higher carbonate content visible in the smear slides (Fig. 5e), is reflected on the lower Fe/Ca content of this Unit as well (Fig. 4g).

Several of the micropaleontological observations made by Expedition 396 scientists are confirmed by this study as well. The abundant organic debris that shows a more terrestrial signal in the upper half of Unit V, indicated by the phytoclasts and pollen observed in the smear slides, has been interpreted to represent a near-shore depositional environment (Planke et al., 2023). This land-derived signal is a shift from the marine one observed in Unit V and the lower portion of Unit V.

The overall lack of thermal alteration noted by other work is consistent with the compositional assessment done in this study. Planke et al. (2023) mentions that, besides some in-situ specimens at the bottom of the Paleocene in Hole U1568A, most of the samples showed immature organic microfossils, and well-preserved siliceous microfossils. We observed a mostly light-colored spore/pollen assemblage (close to “2” to “2+” in the thermal maturity index scale), coherent with the absence of hydrothermal activity in the Modgunn HTVC during the deposition of the sedimentary infilling (Berndt et al., 2023). The siliceous microfossils were noticeably more fragmented, and practically absent on the upper portion of Unit IV, but they did not show degradation consistent with the influence of hydrothermal fluids. Overall, the good to fair preservation of the microfossils, especially in the lower section analyzed here, made it possible to identify the main groups that were present in the samples.

The presence of volcanic glass in some of the samples (Fig. 5c) is consistent with the ash layers observed throughout the succession. For example, Sample X396\_12\_3\_11 shows mostly pristine vesicular glass shards (Fig. 6d), that can reach >200  $\mu$ m in size. The grain size of the ashes and their preservation state, added to the thickness of the ash layers, from 10-200 mm (Planke et al., 2023, supplementary data), are similar to those layers preserved in the Early Eocene Fur Formation (North of Denmark) interpreted to be ash fall deposits, a product of the hydromagmatic eruptions related to the NAIP (Eldholm et al., 1989; Stokke et al., 2020)

In summary, our grain size and composition data reveal a distinctly heterogeneous sedimentary succession making up the infill of the Modgunn Arch HTVC crater (Fig. 7). The shift from dominantly marine to a higher proportion of terrestrial content, along with the evidence of volcanic activity throughout the succession (Fig 4), indicates a change in environmental conditions, registered in this study and confirmed by shipboard data (Planke et al., 2023). The further subdivision proposed in this work is based on the grain size variations that could indicate energy changes in the hydrological regime, hinting to the influence of physical processes acting in the vicinity of the Modgunn HTVC. Although distances to the paleo-shoreline during this time are highly uncertain, it's likely that sand-sized terrigenous material was delivered to the marine setting via rivers and then subsequently reworked by various oceanic currents in this shallow to deep shelf setting. So far, in the Vøring basin, along slope currents have been inferred only for the late Eocene, by seismic and borehole studies (Laberg, et al., 2005a; Laberg, et al., 2005b). However, the shallow nature of the Modgunn HTVC deposits (<200 m paleo-water depth), as reported by the paleontological assemblage in Planke et al. (2023) and Berndt et al. (2023), and previously, for the Vøring plateau by seismic and borehole data from the Deep Sea Drilling Project (DSDP) and Ocean Drilling Program (ODP) (Eldholm et al., 1989; Laberg, et al., 2005a; Laberg, et al., 2005b), would restrict the influence of this current to the ocean surface. Finally, the crater-scale paleo-bathymetry and variable bioturbation could have led to additional depositional and post-depositional imprints in the observed texture of these deposits, precluding a definitive assessment of physical transport processes.

## 21.2. *Relationship with the PETM timing and sedimentary system response to significant climate change*

Our refined understanding of the lithologies and potential depositional processes provides an opportunity to further examine the signature of the PETM in the Modgunn Arch HTVC crater infill. The unique value of Hole U1568A, and why it was targeted in IODP Exp 396, is that it recovers stratigraphy spanning the pre-PETM, the onset of the PETM, and a significant proportion of the main body or phase of the PETM (Berndt et al., 2023). The pre-PETM lithostratigraphic Unit characterized here (Unit VI), allowed us to assess the environmental conditions before the onset and main of the PETM, identified in Units V and IV (Berndt et al., 2023), while the uppermost few grain size samples were intended to capture the transition into the overlying Unit III.

The carbon isotopic excursion (CIE) indicates the presence of the PETM in a sedimentary sequence, along with other markers, including the global occurrence of the dinocyst *Apectodinium augustum* (Crouch et al., 2001). For the Modgunn Arch HTVC, the onset of the CIE was placed 11-15 m above the vent base (base of Unit V) based on the ~6‰ drop in of the  $\delta^{13}\text{C}$  (organic) record of Hole U1567C, located around 400 m north of U1568A (Berndt et al. 2023). This early onset section, however, is not present in U1568A, and Berndt et al. (2023) attributed this to potentially ongoing hydrothermal activity at the time, that was not detected in the sediments studied here, and/or slumping, in the still-active vent axis. Evidence for soft-sediment deformation in the core was not observed during the shipboard core analysis either, but the reflectors in the 3D seismic image of the Modgunn transect (Fig 3.a) could be pointing to a more complex stratigraphy. However, the grain size coarsening, from the sandy mud in Unit V to muddy sand in Unit IV occurs well above the CIE onset and, therefore, some duration after the environmental change associated with the PETM onset. We hypothesize that the lithological onset of the PETM does not coincide with the carbon isotope onset in Hole U1568A due to a delayed response of the sedimentary system. A simple calculation of the duration of this delayed response, based on the thickness of Unit V and the average sediment accumulation rate (1.6 m/kyr; section 3.3), results in a total lag time of ~22.7 kyr, which is within the same order-of-magnitude as the ~31 kyr estimate from Duller et al. (2019).

The transition from Unit V to Unit IV does not exactly coincide with the shift from a marine to a more terrestrial-derived material. This suggests that the biota had a timelier response to the warming event than the sedimentary system. In our study, we propose dividing Unit IV into four subunits (labeled A, B, C, and D from top to bottom) based on grain size variations and composition, which is used to assess the sedimentary system response to the PETM in greater detail. While all subunits are classified by muddy sand, there is a notable variation in ash content, with subunit D exhibiting a higher abundance. The difference in ash percent could serve as a proxy for volcanic activity in the NAIP, potentially occurring tens to hundreds of kilometers away from the HTVC.

Unit C marks the reappearance of marine grains (diatoms) and a gradual reduction in grain size. The absence of terrestrial biogenic material in conjunction with this suggests an environment with lower sediment transport energy. In other words, there was relatively less terrigenous material being delivered to the crater environment during this time. This is succeeded by an upward coarsening and the disappearance of marine biogenic material in subunit B. The increased presence of lithics and some terrestrial biogenic elements in this subunit can be attributed to heightened sediment transport energy. Additionally, the occurrence of volcanic grains like glass shards, pyroxene, and zeolites concentrated at the subunit's bottom is evidence for volcanic activity in the region during the PETM.

The overlying and uppermost subunit A exhibits a gradual increase in grain size followed by a decrease towards the top. The coarsening is supported by Zr/Rb ratios and accompanied by a decrease in the clay fraction, potentially indicated by lower K/Ti intensities. The increment in organic debris throughout the U1568A succession studied here aligns with shipboard palynological and palynofacies analyses in Planke et al. (2023), indicating a consistent rise in mainly terrestrial material throughout the PETM section.

The sedimentological variations observed throughout the ~100 m Late Paleocene to earliest Eocene succession studied here serve as a valuable proxy for providing a qualitative assessment of the sensitivity of the sedimentary system to changes in climate, possibly reflecting local to regional thresholds in the hydrological regime during the PETM. This sedimentological

characterization provides important context for the paleo-environmental reconstructions based solely on geochemical or faunal proxies to be done on Hole U1568A.

## **22. Conclusions**

This study aimed to characterize sedimentary filling of a hydrothermal vent complex and the sedimentary system response to the Paleocene-Eocene Thermal Maximum (PETM) by analyzing the grain size, sorting, and composition of sediments associated with the PETM interval in the Modgunn Arch vent complex, in the Vøring Basin, Norwegian Sea.

The Modgunn hydrothermal vent complex (HTVC) is believed to be one of the primary sources of carbon release during the PETM, as part of a larger sill-hydrothermal vent system in the North Atlantic Igneous Province (NAIP). International Ocean Discovery Program (IODP) Expedition 396 drilled five holes in the vicinity of a HTVC, from proximal to the vent axis (U1568A) to distal (U1567A). Hole U1568A, drilled up to 200 m deep with a high sediment recovery (78%) allowed a high-resolution sedimentological characterization of the crater infill.

The grain size results (n=163 samples) in Hole U1568A shows variability across different depths and in previously defined lithostratigraphic units (Units IV and V; Planke et al., 2023), with noticeable trend changes within. The grain size ranges from very fine silt to medium sand, and there is no overall stratigraphic trend in sorting (which ranges from poorly sorted to very poorly sorted).

The smear slide analysis (n=15 samples) and SEM imaging (n=6 samples) used to characterize the sediment composition and grain morphology of the crater infill succession in Hole U1568A, revealed the presence of clay, lithic grains, quartz, feldspar, and volcanic glass, with a stratigraphic change from marine to more terrestrial biogenic material before the stratigraphic boundary between Units V to IV, and therefore, before the main shift in grain size. The SEM imaging confirmed the morphological aspects of the sediment, including the poor sorting and angular to subrounded shapes.

This study provides a unique opportunity to characterize the sedimentary infill of a marine hydrothermal vent complex (HTVC), specifically focusing on the passive infill phase. Our results refined the existing lithostratigraphic framework in Planke et al. (2023) and revealed a

heterogeneous succession with changes in grain size, composition, and environmental conditions within the units. The proposed subdivision of the Unit IV suggests variations in energy and the influence of other processes, potentially including variations in ocean current activity.

The sedimentological analysis of the closest hole to the center of Modgunn Arch HTVC crater infill provides insights into the sedimentary system's response to the PETM, with evidence suggesting a delayed response of the system and a timelier response of the biota to the warming event. The sedimentological variations observed throughout the succession studied serve as a valuable proxy for assessing the sensitivity of the sedimentary system to changes in climate.

### **23. References Cited**

- Berndt, C., Planke, S., Alvarez Zarikian, C. A., Frieling, J., Jones, M. T., Millett, J. M., Brinkhuis, H., Bünz, S., Svensen, H. H., Longman, J., Scherer, R. P., Karstens, J., Manton, B., Nelissen, M., Reed, B., Faleide, J. I., Huismans, R. S., Agarwal, A., Andrews, G. D. M., ... Yager, S. L. (2023). Shallow-water hydrothermal venting linked to the Palaeocene–Eocene Thermal Maximum. *Nature Geoscience*. <https://doi.org/10.1038/s41561-023-01246-8>
- Blott, S. J., & Pye, K. (2001). GRADISTAT: A grain size distribution and statistics package for the analysis of unconsolidated sediments. *Earth Surface Processes and Landforms*, 26(11), 1237–1248. <https://doi.org/10.1002/esp.261>
- Crouch, E. M., Heilmann-Clausen, C., Brinkhuis, H., Morgans, H. E. G., Rogers, K. M., Egger, H., & Schmitz, B. (2001). Global dinoflagellate event associated with the late Paleocene thermal maximum. *Geology*, 29(4), 315–318. [https://doi.org/10.1130/0091-7613\(2001\)](https://doi.org/10.1130/0091-7613(2001))
- Dickens, G. R., O’Neil, J. R., Rea, D. K., & Owen, R. M. (1995). Dissociation of oceanic methane hydrate as a cause of the carbon isotope excursion at the end of the Paleocene. *Paleoceanography*, 10(6), 965–971. <https://doi.org/10.1029/95PA02087>
- Duller, R. A., Armitage, J. J., Manners, H. R., Grimes, S., & Jones, T. D. (2019). Delayed sedimentary response to abrupt climate change at the Paleocene-Eocene boundary, northern Spain. *Geology*, 47(2), 159–162. <https://doi.org/10.1130/G45631.1>
- Dunkley Jones, T., Lunt, D. J., Schmidt, D. N., Ridgwell, A., Sluijs, A., Valdes, P. J., & Maslin, M. (2013). Climate model and proxy data constraints on ocean warming across the Paleocene–

- Eocene Thermal Maximum. *Earth-Science Reviews*, 125, 123–145.  
<https://doi.org/10.1016/j.earscirev.2013.07.004>
- Dypvik, H., & Harris, N. B. (2001). Geochemical facies analysis of fine-grained siliciclastics using Th/U, Zr/Rb and (Zr+Rb)/Sr ratios. *Chemical Geology*, 181(1), 131–146.  
[https://doi.org/10.1016/S0009-2541\(01\)00278-9](https://doi.org/10.1016/S0009-2541(01)00278-9)
- Eldholm, O., Thiede, J., and Taylor, E. (1989). The Norwegian continental margin: Tectonic, volcanic, and paleoenvironmental framework. In O. Eldholm Thiede, J., Taylor, E., et al. (Ed.), *Proceedings of the Ocean Drilling Program, Scientific Results (Vol. 104, pp. 5–26)*. Ocean Drilling Program. <https://doi.org/10.2973/odp.proc.sr.104.110.1989>
- Eldholm, O., Thiede, J., & Taylor, E. (1989). Evolution of the Vøring Volcanic Margin. *Proc., Scientific Results, ODP, Leg 104, Norwegian Sea*, 104, 1033–1065.  
<https://doi.org/10.2973/odp.proc.sr.104.191.1989>
- Folk, R. L., & Ward, W. C. (1957). Brazos River bar [Texas]; a study in the significance of grain size parameters. *Journal of Sedimentary Research*, 27(1), 3–26.  
<https://doi.org/10.1306/74D70646-2B21-11D7-8648000102C1865D>
- Foreman, B. Z., Heller, P. L., & Clementz, M. T. (2012). Fluvial response to abrupt global warming at the Palaeocene/Eocene boundary. *Nature*, 491(7422), Article 7422.  
<https://doi.org/10.1038/nature11513>
- Frieling, J., Svensen, H. H., Planke, S., Cramwinckel, M. J., Selnes, H., & Sluijs, A. (2016). Thermogenic methane release as a cause for the long duration of the PETM. *Proceedings of the National Academy of Sciences of the United States of America*, 113(43), 12059–12064.  
<https://doi.org/10.1073/pnas.1603348113>
- Giusberti, L., Rio, D., Agnini, C., Backman, J., Fornaciari, E., Tateo, F., & Oddone, M. (2007). Mode and tempo of the Paleocene-Eocene thermal maximum in an expanded section from the Venetian Pre-Alps. *GSA Bulletin*, 119(3–4), 391–412. <https://doi.org/10.1130/B25994.1>
- Held, I. M., & Soden, B. J. (2006). Robust Responses of the Hydrological Cycle to Global Warming. *Journal of Climate*, 19(21), 5686–5699. <https://doi.org/10.1175/JCLI3990.1>

- John, C. M., Bohaty, S. M., Zachos, J. C., Sluijs, A., Gibbs, S., Brinkhuis, H., & Bralower, T. J. (2008). North American continental margin records of the Paleocene-Eocene thermal maximum: Implications for global carbon and hydrological cycling. *Paleoceanography*, 23(2). <https://doi.org/10.1029/2007PA001465>
- Kennett, J. P., & Stott, L. D. (1991). Abrupt deep-sea warming, palaeoceanographic changes and benthic extinctions at the end of the Palaeocene. *Nature*, 353(6341), Article 6341. <https://doi.org/10.1038/353225a0>
- Laberg, J. S., Dahlgren, K. I. T., & Vorren, T. O. (2005). The Eocene–late Pliocene paleoenvironment in the Vøring Plateau area, Norwegian Sea—Paleoceanographic implications. *Marine Geology*, 214(1), 269–285. <https://doi.org/10.1016/j.margeo.2004.10.031>
- Laberg, J. S., Stoker, M. S., Dahlgren, K. I. T., Haas, H. de, Haflidason, H., Hjelstuen, B. O., Nielsen, T., Shannon, P. M., Vorren, T. O., van Weering, T. C. E., & Ceramicola, S. (2005). Cenozoic alongslope processes and sedimentation on the NW European Atlantic margin. *Marine and Petroleum Geology*, 22(9), 1069–1088. <https://doi.org/10.1016/j.marpetgeo.2005.01.008>
- Liu, L., Chen, J., Chen, Y., Ji, J., & Lu, H. (2002). Variation of Zr/Rb ratios on the Loess Plateau of Central China during the last 130000 years and its implications for winter monsoon. *Chinese Science Bulletin*, 47(15), 1298–1302. <https://doi.org/10.1360/02tb9288>
- Marsaglia, K. M., & Milliken, K. L. (2023). IODP Technical Note. International Ocean Discovery Program. <https://doi.org/10.14379/iodp.tn.5.2023>
- McCarren, H., Kelly, D. C., & Nielsen, T. (2007). The Palaeocene-Eocene carbon isotope excursion: Constraints from individual shell planktonic foraminifer records. *Philosophical Transactions of the Royal Society A: Mathematical, Physical and Engineering Sciences*. <https://doi.org/10.1098/rsta.2007.2045>
- McInerney, F. A., & Wing, S. L. (2011). The Paleocene-Eocene Thermal Maximum: A Perturbation of Carbon Cycle, Climate, and Biosphere with Implications for the Future. *Annual*

Review of Earth and Planetary Sciences, 39(1), 489–516. <https://doi.org/10.1146/annurev-earth-040610-133431>

McKerrow, W., Macniocail, C., & Dewey, J. (2000). The Caledonian Orogeny redefined. *Journal of the Geological Society*, 157. <https://doi.org/10.1144/jgs.157.6.1149>

Murphy, B. H., Farley, K. A., & Zachos, J. C. (2010). An extraterrestrial <sup>3</sup>He-based timescale for the Paleocene–Eocene thermal maximum (PETM) from Walvis Ridge, IODP Site 1266. *Geochimica et Cosmochimica Acta*, 74(17), 5098–5108. <https://doi.org/10.1016/j.gca.2010.03.039>

Penman, D. E. (2016). Silicate weathering and North Atlantic silica burial during the Paleocene–Eocene Thermal Maximum. *Geology*, 44(9), 731–734. <https://doi.org/10.1130/G37704.1>

Piva, A., Asioli, A., Schneider, R. R., Trincardi, F., Andersen, N., Colmenero-Hidalgo, E., Dennielou, B., Flores, J.-A., & Vigliotti, L. (2008). Climatic cycles as expressed in sediments of the PROMESS1 borehole PRAD1-2, central Adriatic, for the last 370 ka: 1. Integrated stratigraphy. *Geochemistry, Geophysics, Geosystems*, 9(1). <https://doi.org/10.1029/2007GC001713>

Planke, S., Berndt, C., Alvarez Zarikian, C. A., and the Expedition 396 Scientists. (2003). Mid-Norwegian Margin Magmatism and Paleoclimate Implications. *Proceedings of the International Ocean Discovery Program, 396*. <https://doi.org/10.14379/iodp.proc.396.2023>

Pujalte, V., Baceta, J. I., & Schmitz, B. (2015). A massive input of coarse-grained siliciclastics in the Pyrenean Basin during the PETM: The missing ingredient in a coeval abrupt change in hydrological regime. *Climate of the Past*, 11(12), 1653–1672. <https://doi.org/10.5194/cp-11-1653-2015>

Röhl, U., Westerhold, T., Bralower, T. J., & Zachos, J. C. (2007). On the duration of the Paleocene–Eocene thermal maximum (PETM). *Geochemistry, Geophysics, Geosystems*, 8(12). <https://doi.org/10.1029/2007GC001784>

Rothwell, R. G., & Croudace, I. w. (2015). Twenty Years of XRF Core Scanning Marine Sediments: What Do Geochemical Proxies Tell Us? In I. W. Croudace & R. G. Rothwell (Eds.), *Micro-XRF Studies of Sediment Cores: Applications of a non-destructive tool for the*

environmental sciences (pp. 25–102). Springer Netherlands. [https://doi.org/10.1007/978-94-017-9849-5\\_2](https://doi.org/10.1007/978-94-017-9849-5_2)

Schmitz, B., & Pujalte, V. (2003). Sea-level, humidity, and land-erosion records across the initial Eocene thermal maximum from a continental-marine transect in northern Spain. *Geology*, 31(8), 689–692. <https://doi.org/10.1130/G19527.1>

Sharman, G. R., Covault, J. A., Flaig, P. P., Dunn, R., Fussee-Durham, P., Larson, T. E., Shanahan, T. M., Dubois, K., Shaw, J. B., Crowley, J. L., & Shaulis, B. (2023). Coastal response to global warming during the Paleocene-Eocene Thermal Maximum. *Palaeogeography, Palaeoclimatology, Palaeoecology*, 111664. <https://doi.org/10.1016/j.palaeo.2023.111664>

Stokke, E. W., Liu, E. J., & Jones, M. T. (2020). Evidence of explosive hydromagmatic eruptions during the emplacement of the North Atlantic Igneous Province. *Volcanica*, 3(2), Article 2. <https://doi.org/10.30909/vol.03.02.227250>

Storey, M., Duncan, R. A., & Swisher, C. C. (2007). Paleocene-Eocene Thermal Maximum and the Opening of the Northeast Atlantic. *Science*, 316(5824), 587–589. <https://doi.org/10.1126/science.1135274>

Svensen, H., Jamtveit, B., Planke, S., & Chevallier, L. (2006). Structure and evolution of hydrothermal vent complexes in the Karoo Basin, South Africa. *Journal of the Geological Society (London, UK)*, 163(4), 671–682. <https://doi.org/10.1144/1144-764905-037>

Svensen, H., Planke, S., Malthes-Sørensen, A., Jamtveit, B., Myklebust, R., Rasmussen Eidem, T., & Rey, S. S. (2004). Release of methane from a volcanic basin as a mechanism for initial Eocene global warming. *Nature*, 429(6991), Article 6991. <https://doi.org/10.1038/nature02566>

Talwani, M., Udintsev, G., et al. (1976). Initial Reports of the Deep-Sea Drilling Project (Vol. 38). US Government Printing Office. <https://doi.org/10.2973/dsdp.proc.38.1976>

Westerhold, T., Röhl, U., McCarren, H. K., & Zachos, J. C. (2009). Latest on the absolute age of the Paleocene–Eocene Thermal Maximum (PETM): New insights from exact stratigraphic position of key ash layers +19 and –17. *Earth and Planetary Science Letters*, 287(3), 412–419. <https://doi.org/10.1016/j.epsl.2009.08.027>

- Wu, L., Wilson, D. J., Wang, R., Yin, X., Chen, Z., Xiao, W., & Huang, M. (2020). Evaluating Zr/Rb Ratio From XRF Scanning as an Indicator of Grain-Size Variations of Glaciomarine Sediments in the Southern Ocean. *Geochemistry, Geophysics, Geosystems*, 21(11), e2020GC009350. <https://doi.org/10.1029/2020GC009350>
- Zachos, J. C., Röhl, U., Schellenberg, S. A., Sluijs, A., Hodell, D. A., Kelly, D. C., Thomas, E., Nicolo, M., Raffi, I., Lourens, L. J., McCarren, H., & Kroon, D. (2005). Rapid Acidification of the Ocean During the Paleocene-Eocene Thermal Maximum. *Science*, 308(5728), 1611–1615. <https://doi.org/10.1126/science.1109004>
- Zachos, J., Pagani, M., Sloan, L., Thomas, E., & Billups, K. (2001). Trends, Rhythms, and Aberrations in Global Climate 65 Ma to Present. *Science*, 292(5517), 686–693. <https://doi.org/10.1126/science.1059412>
- Zeebe, R. E. (2013). What caused the long duration of the Paleocene-Eocene Thermal Maximum? *Paleoceanography*, 28(3), 440–452. <https://doi.org/10.1002/palo.20039>
- Zeebe, R. E., Zachos, J. C., & Dickens, G. R. (2009). Carbon dioxide forcing alone insufficient to explain Palaeocene–Eocene Thermal Maximum warming. *Nature Geoscience*, 2(8), 576–580. <https://doi.org/10.1038/ngeo578>